Real-time Investigation of Catalytic Reaction Mechanisms by Mass Spectrometry and Infrared Spectroscopy

by

Robin Theron
B.Sc., University of Saskatchewan, 2013

A Thesis Submitted in Partial Fulfillment
of the Requirements for the Degree of

MASTER OF SCIENCE

in the Department of Chemistry

© Robin Theron, 2015
University of Victoria

All rights reserved. This thesis may not be reproduced in whole or in part, by photocopy
or other means, without the permission of the author.

Supervisory Committee

Real-time Investigation of Catalytic Reaction Mechanisms by Mass Spectrometry and Infrared Spectroscopy

by

Robin Theron
B.Sc., University of Saskatchewan, 2013

Supervisory Committee

Dr. J. Scott McIndoe, Department of Chemistry
Supervisor

Dr. Dennis Hore, Department of Chemistry
Departmental Member

Abstract

Supervisory Committee
Dr. J. Scott McIndoe, Department of Chemistry
Supervisor
Dr. Dennis K. Hore, Department of Chemistry
Departmental Member

Electrospray ionization mass spectrometry (ESI-MS) has been applied to the realtime study of homogeneous organometallic reactions. ESI-MS as a soft ionization technique is amenable to fragile organometallic complexes, and as a fast and sensitive technique is ideal for detecting low concentration intermediates within reactions. Pressurized sample infusion (PSI) was used for continuous sample infusion into the mass spectrometer, granting the air-free conditions necessary for these reactions to be successful, and resulting in reaction profile data that contains information about the dynamics of speciation of the catalyst. Collision induced dissociation (CID) was used to probe the binding affinities of various bisphosphine ligands as well as in characterizing intermediates in reactions.

PSI ESI-MS was applied to the hydroboration reaction of the alkene tert-butylethene using the amine-borane $H_3B{\cdot}NMe_3$ catalyzed by $[Rh(xantphos)]^+$ fragments to show how the reaction progresses from substrates to products. PSI ESI-MS was also applied to the hydrogenation of a charge-tagged alkyne $[Ph_3P(CH_2)_4C_2H]^+[PF_6]^-$, catalyzed by a cationic rhodium complex $[Rh(P^cPr_3)_2(\eta^6\text{-}FPh)]^+[B\{3,5\text{-}(CF_3)_2C_6H_3\}_4]^-$ (P^cPr_3 = triscyclopropylphosphine, FPh = fluorobenzene). This work demonstrated the use of ESI-MS in conjunction with NMR, kinetic isotope effects and numerical modeling for determining a mechanism of reaction.

The hydroacylation reaction of a β–S substituted aldehyde and an alkyne catalyzed by $[Rh(P^iPr_2NMeP^iPr_2)(\eta^6\text{-}FPh)]^+[B\{3,5\text{-}(CF_3)_2C_6H_3\}_4]^-$ (P^iPr_2 = diisopropylphosphine) was studied by PSI ESI-MS while employing charged tags, allowing for observation of reaction progress and some key intermediates.

A new concept for mechanistic analysis has been developed: coupling of an orthogonal spectroscopic technique with PSI ESI-MS. This new method was applied to the same hydroacylation reaction studied with charged tags. The use of IR in conjunction with ESI-MS led to rate information about the overall reaction along with dynamic information about catalytic speciation. Coupling of these techniques allows for detection over many magnitudes of concentration.

Table of Contents

List of Tables

List of Figures

List of Schemes

List of Abbreviations

Ald	aldehyde
Ar	aryl
$[BAr^F{}_4]^-$	tetrakis[3,5-bis(trifluoromethyl)phenyl]borate
$[BF_4]^-$	tetrafluoroborate
b.p	boiling point
Bu	butyl
cat	catalyst
CI	chemical ionization
CID	collision induced dissociation
COD	cyclooctadiene
Da	Dalton
DC	Direct current
1,2-DCE	1,2-dichloroethane
DCM	dichloromethane
DFT	density functional theory
E_0	mass normalized collision energy
EDESI	energy-dependent electrospray ionization
EI	electron impact
E_{LAB}	collision cell voltage
ESI	electrospray ionization
ESI(-)-MS	negative-ion electrospray ionization mass spectrometry
ESI(+)-MS	positive-ion electrospray ionization mass spectrometry
FPh	fluorobenzene
FT	Fourier transform
FTICR	Fourier transform ion cyclotron resonance
FTIR	Fourier transform infrared
GC	gas chromatography
HPLC	high performance liquid chromatography
^{i}Bu	isobutyl
^{i}Pr	isopropyl
IR	infrared
KE	kinetic energy
KIE	kinetic isotope effect
L	ligand
m_A	mass of collision gas
m_I	mass of target ion
m.p.	melting point
m/z	mass-to-charge ratio
MALDI	matrix-assisted laser desorption

	ionization
MCP	microchannel plate
Me	methyl
MS	mass spectrometry/ mass spectrometer/ mass spectrum
MS/MS	tandem mass spectrometry
NMR	nuclear magnetic resonance
OA	oxidative addition
PEEK	polyetheretherketone
$[PF_6]^-$	hexafluorophosphate
Ph	phenyl
PSI	pressurized sample infusion
Q-TOF	quadrupole-time-of-flight
R	Alkyl
RE	reductive elimination
rf	radio frequency
rt	room temperature
SPS	Solvent Purification System
TBE	tert-butylethene
^{t}Bu	tertiary butyl
THF	tetrahydrofuran
TIC	total ion current
TOF	time-of-flight
UV	ultraviolet
UV/Vis	ultraviolet/visible

List of Structures

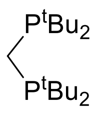

2.1

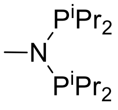

2.2

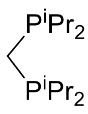

2.3

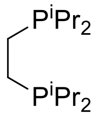

2.4

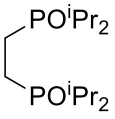

2.5

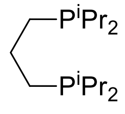

2.6

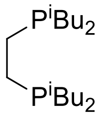

2.7

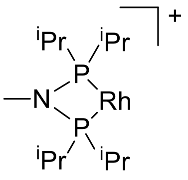

Rh(2.2)

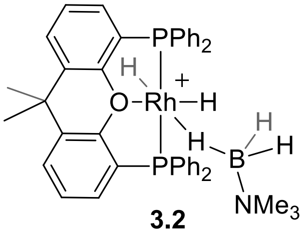

3.2

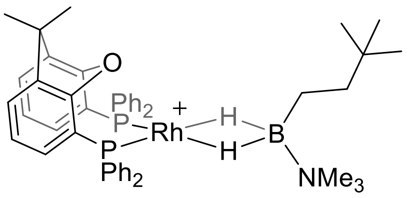

3.3

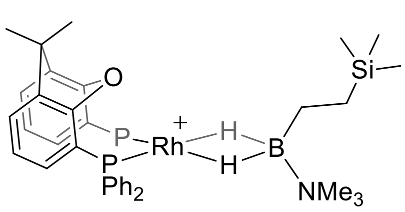

3.4

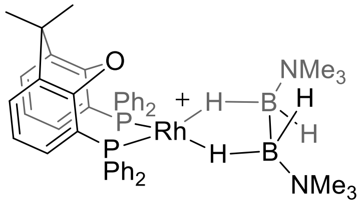

3.5

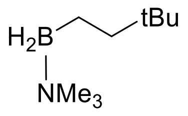

3P

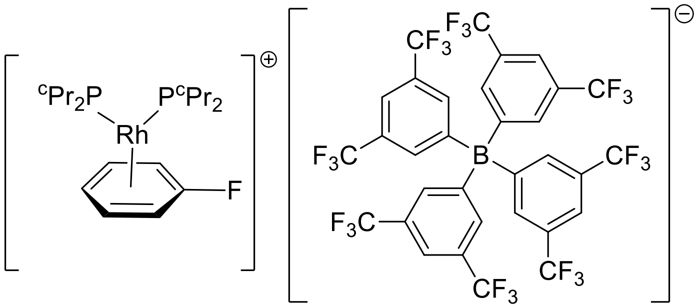

Catalyst 4

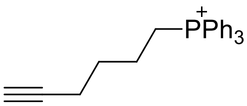

Alkyne 4.1

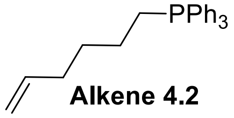

Alkene 4.2

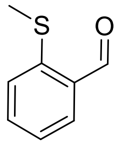

5.1

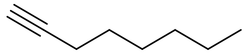

5.2

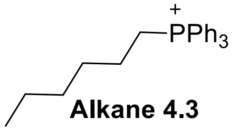

Alkane 4.3

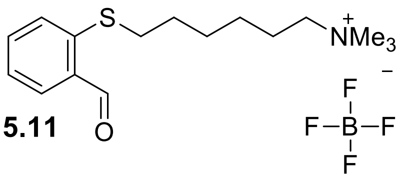

5.11

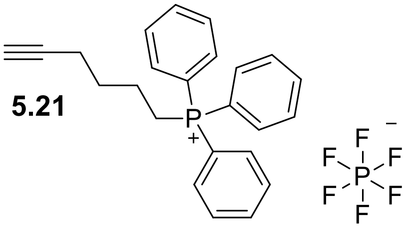

5.21

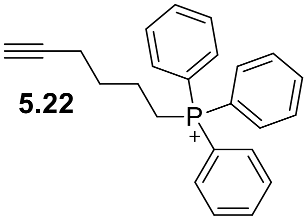

5.22

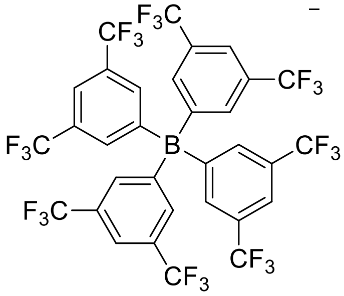

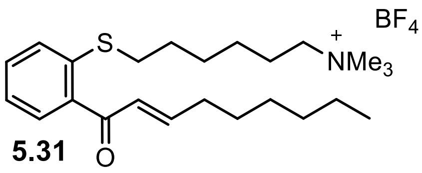

5.31

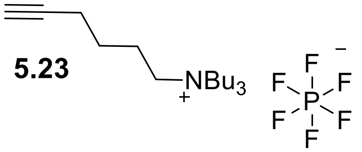

5.23

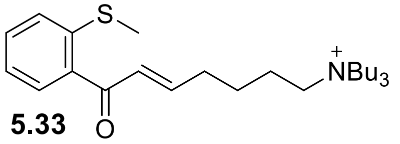

5.33

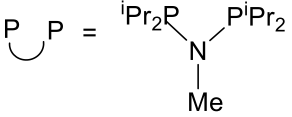

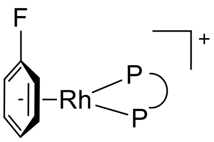

5.A

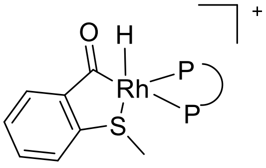

5.B.

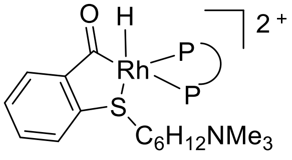

5.B1

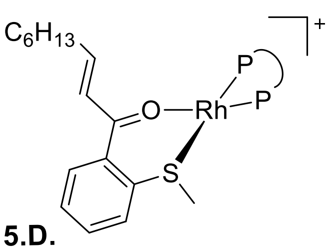

5.D.

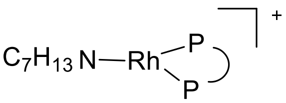

5.E

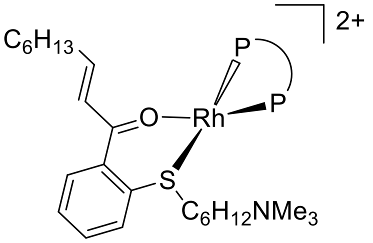

5.D1

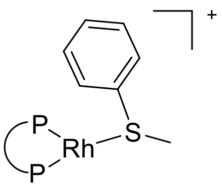

5.F.

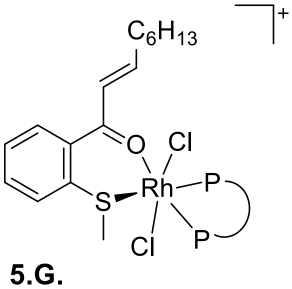

5.G.

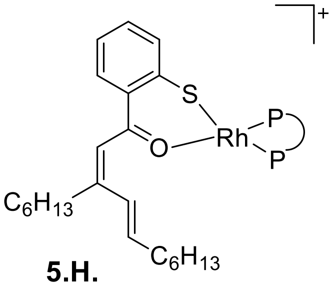

5.H.

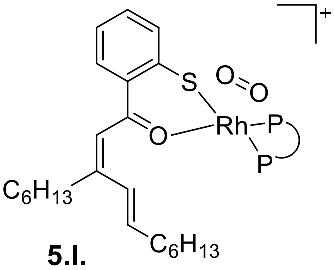

5.I.

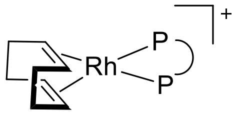

5.K.

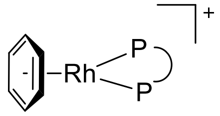

5.L.

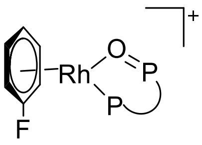

5.O

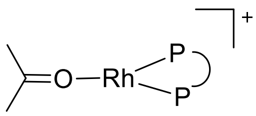

5.Y

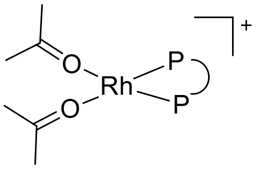

5.Z

Acknowledgments

I would like to thank Dr. J. Scott McIndoe for selecting me as a grad student in his group, and thus opening up the great opportunities I have had over the last two years. His confidence in my abilities enabled me to take on new problems and situations that I did not know I could. He is a superb mentor in research, teaching duties, and in the general trials one goes through as a grad student.

I also thank my group members, Lars and Eric who convinced me to join the group initially, Jingwei who taught me about mass spectrometry experiments, Rhonda, the heart of the group, for teaching me the how-too's of the lab, and for your listening ear whenever I needed to rant about something. Jane, for making being at work more fun. Kingsly, for the help in running so many experiments, and being such a quick learner. Amelia, thanks for your many hours of work trying to get multiple instruments and air-sensitive chemical reactions to work simultaneously and the cheerleading that kept me sane in the weeks of failed experiments.

Ori Granot and Chris Barr, thanks for teaching me about Mass spectrometry and NMR, both incredibly knowledgeable in their fields and a joy to work with.

I would like to thank Dr.A.S. Weller and the Weller group for graciously hosting me while visiting their labs, teaching me new skills, and showing me some of what Oxford had to offer.

Jan, Lorraine, Jan-Jacques, Frances, vir all julle ondersteuning, sonder julle liefde sou ek nooit so vêr gekom het nie.

1 Overview of ESI MS and IR-ESI MS for Reaction Monitoring

1.1 Beginnings of Mass Spectrometry

While studying phenomena in gas discharge tubes in the late 19th century Wilhelm Wein and JJ Thompson found that beams of positive or negative ions created in the gas discharge tubes could be deflected by magnetic fields as well as electric fields. The rays of ions seen to extend from the cathode to the anode were called cathode rays. Moving in the opposite direction to the cathode rays were streams of positive particles which were called anode rays. Wilhelm Wein and J.J. Thompson both studied cathode rays as well as the anode rays leading them to determine the mass to charge ratio of different anode rays as well as the cathode rays. The particles making up the cathode rays were initially called corpuscles which later would be renamed the electron, and J.J. Thompson would win the Nobel Prize in physics for the discovery. [1]

Deflection of anode rays was the start of mass spectrometry. When an anode ray is deflected by magnetic and electric fields, ions of different mass to charge ratios could be separated, leading to the discovery of isotopes. The first element reported with more than one isotope was neon. Thompson and Aston channeled streams of neon ions through magnetic and electric fields and found that there was two paths of deflection, and thus two different masses of neon, ^{20}Ne and ^{22}Ne. This was the first example of mass spectrometry and was performed in an instrument they called the mass spectrograph (Figure 1.1).[2,3] The mass spectrograph underwent improvements by Aston for the goal of being able to do quantitative experiments. A better vacuum system was installed, as well as a series of slits rather than a tube in order to get a stronger beam of ions. This beam was deflected by an electric field from two parallel plates at an angle. This beam passed between two poles of a large magnet, the ions were deflected according to their mass and hit a photographic plate. Tuning the electric field on the parallel plates would focus different mass ions onto the photographic plate.[4] He measured neon and proved that neon did indeed have two isotopes, then tested every element he could find. He discovered that all isotopes of elements are whole number multiples of the mass of the hydrogen atom[5] [6]. In 1922 he won the Nobel Prize in chemistry for his work and discoveries. Mass spectrometry since then has grown into arguably the fastest and most powerful analytical tool used currently.

Figure 1.1. Image of Aston's third mass spectrograph displayed in Cavendish Laboratory museum.[7]

All mass spectrometers are made up of three main components: an ionization source, a mass selector, and a detector. In Aston's mass spectrograph the ion source was the gas chamber with the potential applied across it, the mass selector was electric and magnetic fields, and the detector was a photographic plate. Since then these three aspects of the mass spectrometer has evolved continuously. Many different ionization methods have been developed, such as electron impact ionization (EI), chemical ionization (CI), spray ionization, gas discharge ionization, photoionization, desorption ionization.[8] For mass selectors there are many to choose from, the magnetic sector, quadrupole mass filters, time-of-flight analyzers, ion traps, orbitraps, and Fourier transform ion cyclotron resonance (FTICR), and each has their niche within mass spectrometry.[8] Detectors used are generally electron multipliers and microchannel plate detectors are common while Orbitraps and FTICR instruments require inductive detectors.[8] The instrument used in this work is a Waters Q-Tof *micro*, which is an electrospray ionization-quadrupole-time-of-flight mass spectrometer (ESI-QTOF-MS) with a microchannel plate (MCP) detector.

1.2 Ionization sources:

Ionization sources as the beginning of the mass spectrometry process will be discussed first. The firstly developed ionization sources were electron ionization (EI), developed by Dempster where he reported on the formation of H_3 by using a method other than the cathode ray in order to produce the positive rays that would be detected. He used electrons produced at a Wehnelt cathode that he accelerated in a field, these electrons ionize the gas producing positive particles that have a velocity that takes them through a narrow tube where they are deflected by electric and magnetic fields and get projected along a parabolic path.[9] This method grew into EI, the most widely used MS ionization method.

Modern EI consists of heating a metal filament by running a current through it which causes release of electrons. These electrons are focussed into a beam and directed towards a trap electrode, the neutral sample that is to be analyzed is introduced perpendicularly to the stream of electrons, and as the neutral analytes gets close to the electrons, the neutral analytes experience large fluctuations in the electric fields surrounding them and the neutral molecules lose electrons and become ionized. The method of EI is considered a “hard” ionization technique because during this process the analyte also become fragmented and the molecular ion is rarely seen to any high degree, and thus can produce extremely complicated spectra for even simple molecules. Because fragmentation happens in a reliable way, the fragmentation pattern produced by an analyte can be used to characterize it. Large databases exist for EI fragmentation patterns, and characterization is achieved through finding a match to a library compound’s fragmentation pattern.

Introducing a complex mixture to this method could produce spectra which are unintelligible and difficult to deconvolute due to the amount of peaks present. EI is rarely useful in transition metal organometallic chemistry as the complexes would be decomposed and the molecular ion would likely not be visible. There also does not exist a database of organometallic compound fragmentation patterns to match data with, which is the exact property that makes EI such a useful technique for organic molecules.

1.2.1 Electrospray Ionization

Conversely to EI, electrospray ionization (ESI) is a soft ionization method (Figure 1.2). ESI involves passing the analyte solution through a highly charged capillary that has a potential difference of around 3000 V applied across it. When the solution exits the capillary, it is in the shape of a cone, called a Taylor cone and the solution carries a net charge. Either a positive or negative net charge can be produced. A positive net charge on the solution can result from oxidation processes including corrosion of the metal capillary, oxidation of the solvents and analytes and other reactions that might eliminate anion from the solution. A net negatively charge can be produced by reduction of the solvents, analytes, or elimination of cations from solution. The net charge on the solution causes droplets to be repelled from one another, which results in a very fine spray of droplets. These droplets containing the charged analytes get dried by a desolvation gas at an elevated temperature, which as solvent gets evaporated results in smaller droplets with a higher density of ions. The ions that are least well solvated and/or least strongly ion paired would migrate to the surface of the droplet and when the droplet reaches a certain size the surface field strength is high enough to encourage ion evaporation, resulting in naked gas phase ions.[10–12]

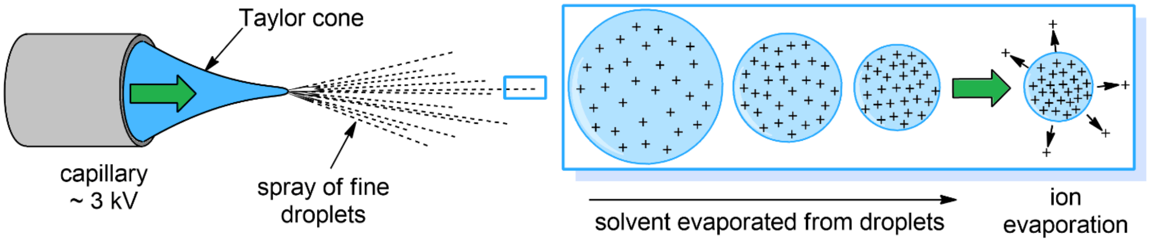

Figure 1.2. The process of electrospray ionization, showing solvent evaporation followed by ion evaporation for the formation of desolated ions in the gas phase.

ESI results in a spectrum with little, if any, fragmentation. It is important to note that ESI does not ionize the analyte, thus an analyte that is inherently charged or that can easily become so is most often used. It is possible to obtain spectra of neutral compounds with this method. For example if the analyte has basic groups, adding in acid can encourage the formation of $[M+H]^+$ ions . Adding sodium or potassium ions can cause formation of $[M+Na]^+$ or $[M+K]^+$ ions. These can be detected in positive ion mode.

Conversely if the analyte is acidic, by adding in a base $[M-H]^-$ ions can be formed and be detected in negative ion mode.[13]

As fragmentation is minimal, a very simple spectrum is produced, generally consisting of only $[M]^+$ or $[M]^-$. The simplicity of these spectra makes it a lot more feasible to study complex mixtures of ions and discern what the mixture is made up of. The softness allows for organometallic compounds to be characterized based on their molecular ion peaks and isotope patterns. Many organometallic compounds contain metals rich in isotopes, so isotope matching can be used to identify the character of complexes. The method of tandem MS/MS can also be used in characterization. As ESI-MS produces minimal fragmentation, tandem MS techniques can be used to induce fragmentation under a controlled environment. Determining where complexes fragment and the masses of the fragmentation losses can give insight into the character of the complex. [13]

1.3 Mass analyzers: Quadrupole – Time of Flight

Once gas phase ions have been created they are drawn into the sample cone to enter the mass selection part of the instrument shown in Figure 1.3. They are drawn in pneumatically as the pressure inside the source is lower than the pressure outside of the sample cone, and also by a voltage difference between outside the sample and inside the sample cone. Excess ions that do not make it into the sample cone end up on the baffle, which gets cleaned between experiments to prevent cross-contamination.

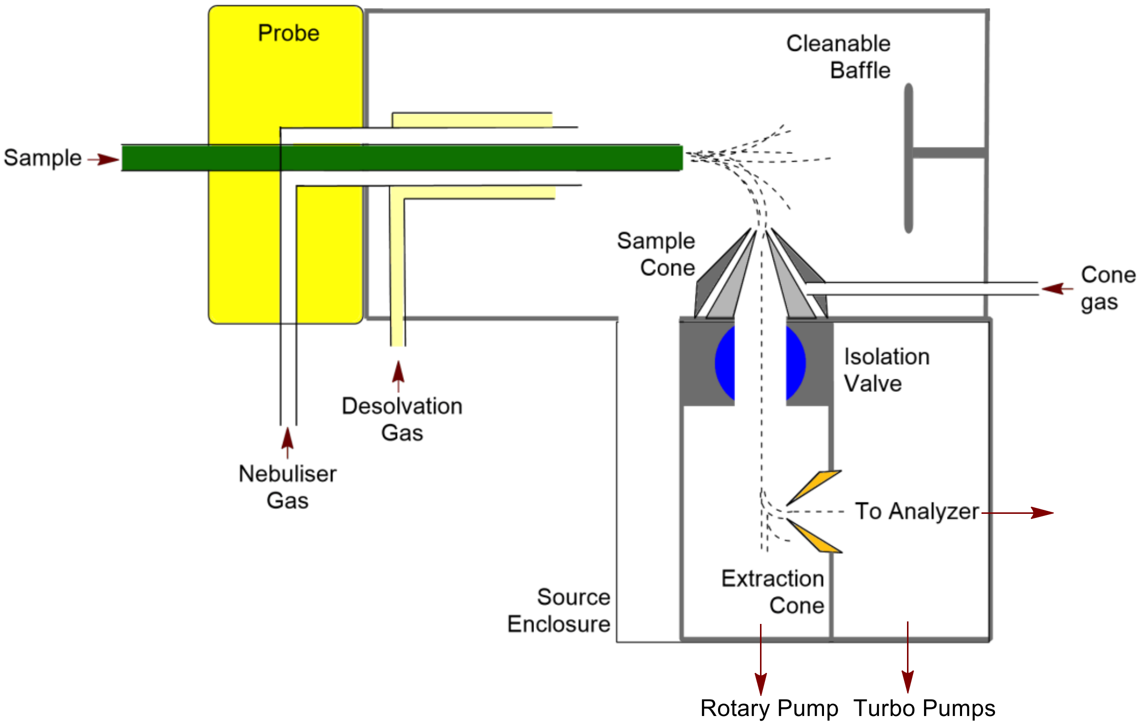

Figure 1.3. Ion path in the electrospray source of a Q-Tof Micro.

Next, the ions travel through the extraction cone into an area of even lower pressure and get guided by a radio frequency only hexapole shown in Figure 1.4.

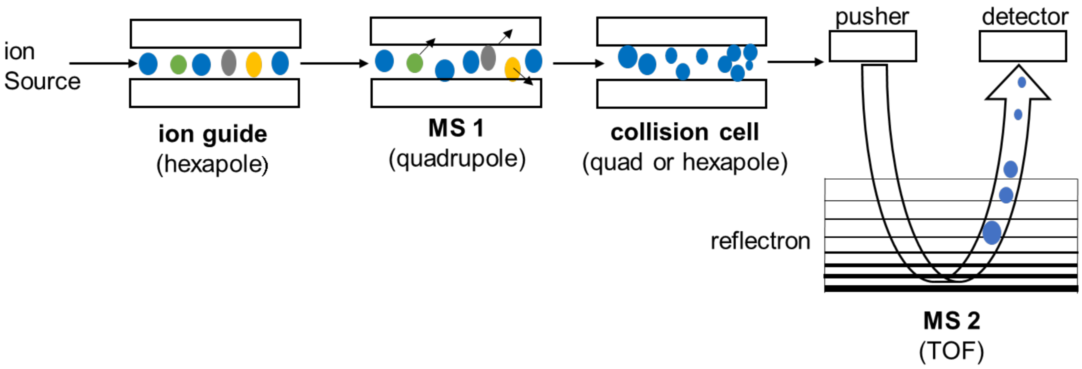

Figure 1.4. Ion path through Q-TOF, from ion source, through RF only hexapole to first mass selector, quadrupole, through collision cell to mass analyzer TOF to detector.

From this point the ions travel to the mass selector(s) through a series of chambers under increasingly high vacuum. The ions reach the quadrupole which can be set at rf-only mode in which case it acts as an ion guide to guide ions through the collision cell towards the pusher to then be analyzed by the time of flight (TOF). This situation describes using the TOF for mass analysis (MS1). The other option that this setup can be used for is to employ the quadrupole as a mass selector (MS1) by applying an rf and DC voltage, thus allowing only a narrow mass range of ions into the collision cell to be analyzed by the TOF (MS2).

A quadrupole is made up of four parallel metal rods, which are paired electrically to the rods opposite one another, and holding a charge of opposite polarity of the other pair. The polarity of these pairs of rods switch rapidly back and forth, and as ions travel through the area between them the ions are attracted to a rod of opposite polarity, but as the rod switches polarity the ion gets repelled by the rod changing the trajectory of the ion. This process can provide mass selection because a specific frequency only allows a certain mass to charge ratio to pass through without colliding into a quadrupole rod.[14]

Next, the ions that made it through the quadrupole reach the collision cell which is at a pressure of 10^{-3} mbar, slightly higher pressure than the quadrupole. At this higher pressure the ions can be focussed and passed through, or excited and collided with gas molecules by applying a voltage across the collision cell.

The next step for the ions is reaching the TOF, the second mass analyzer in this instrument (MS2). The TOF works on the principle of kinetic energy, where all atoms are given the same amount of kinetic energy in the form of an electric pulse at the start of the process and then take varying amounts of time to reach the detector based on their masses. As described by the equation for kinetic energy

$$\mathrm{E}_k = \frac{1}{2}mv^2 \tag{1.1}$$

showing that as the kinetic energy remains the same, the different masses would be associated with different velocities, and thus different amounts of time that the different mass ions would take in order to reach the detector. The amount of kinetic energy that was supplied to the ion at the pusher pulse can be calculated form

$$\mathrm{E}_k = \mathrm{ze}V \tag{1.2}$$

where z is the charge of the ion, *e* is the charge of the ion in coulombs, and *V* is the strength of the electric field in volts. Putting equations (1.1) and (1.2) together and solving for *m/z* determines the mass to charge ratio of an ion:

$$\mathrm{ze}V = \frac{1}{2}mv^2 \tag{1.3}$$

$$\mathrm{ze}V = \frac{1}{2}m\left(\frac{dx}{dt}\right)^2 \tag{1.4}$$

$$m/z = 2\mathrm{e}V\left(\frac{dt}{dx}\right)^2 \tag{1.5}$$

where m is the mass of the ion ion kg, z is the charge of the ion, dt is the flight time in seconds, and dx is the flight path length in meters.

The TOF is under much higher vacuum than the rest of the instrument, at 10^{-7} mbar. This low pressure is extremely important in a TOF as the mean free path of the ions need to be in excess of the length of the flight tube to prevent collisions between ions and ensure that all atoms of the same mass to charge ratio would hit the detector at the same time.

By the kinetic theory of gasses, the mean free path (L) of an ion and a molecule is given by

$$L = \frac{kT}{\sqrt{2}\,\sigma p} \tag{1.6}$$

where k is Boltzmann's constant, T is temperature in Kelvin, p is the pressure in Pa, σ is the collision cross section in m^2 ($\sigma = \pi d^2$), where d is the sum of the radii of the stationary molecule and the colliding ion). So, by decreasing the pressure we can increase the mean free path of the ions, and thus ensure their transit without collision through the instrument.[15]

In order to improve the resolution of a TOF, the flight path within the TOF is outfitted with a reflectron (Figure 1.5). A reflectron is a gradient of electric fields that act like an ion mirror. The figure shows a situation where three different ions of the same *m/z* are pushed with slightly different amounts of kinetic energy towards the reflectron. As these ions move further, the slight difference in kinetic energy results in an increasing separation. As the ions reach the reflectron, the ion with the most kinetic energy penetrates the reflectron field further than the ion with less energy, and thus travels a longer distance than its less energetic counterpart. The result is a focussed packet of ions, where ions of the same *m/z* arrive at the detector at the same time.

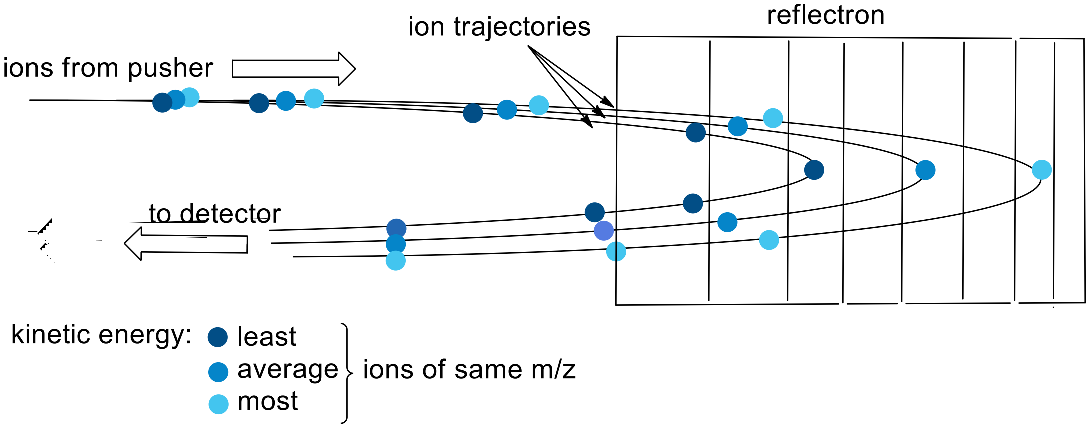

Figure 1.5.Trajectory of three ions of the same *m/z* but different initial kinetic energies in a time-of-flight mass analyzer with reflectron.

1.4 Detector

The detector used is a microchannel plate detector (MCP), which is an array of thousands of electron multiplier tubes. When an ion hits the MCP, a small current is generated which gets multiplied in a cascade process to a larger current which is the electronic signal that gets transferred to Water's software MassLynx where the ion counts and *m/z* are displayed for the user.

1.5 Collision Induced Dissociation

Collision Induced Dissociation (CID) can be achieved by using the instrument in MS/MS mode; focusing the quadrupole mass analyzer on a specific target *m/z* value, allowing only ions of a specific *m/z* through the quadrupole to reach the collision cell, we call this ion the precursor ion. In the collision cell these ions are excited in the presence of a collision gas, argon, the excited ions collide with the gas and undergo dissociation into product ions. This process is depicted in Figure 1.6.

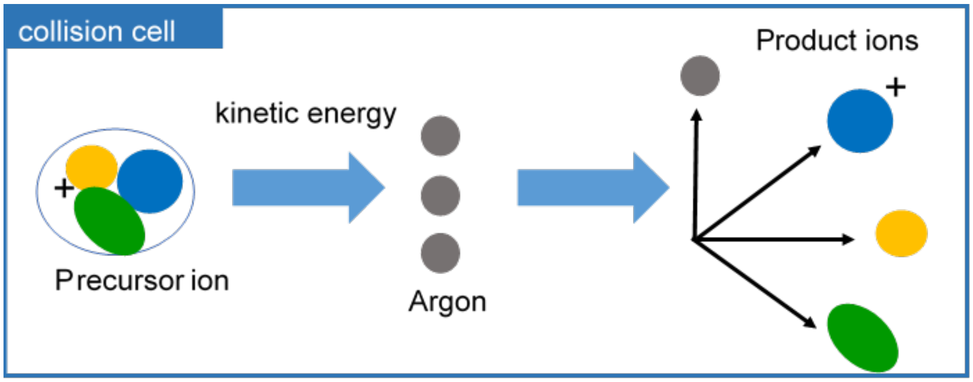

Figure 1.6. Collision induced dissociation process in a collision cell with a cationic precursor ion colliding with argon as collision gas to form fragments.

These fragments can give useful information about the structure of the parent ion. The pressure of the gas in the collision cell can be altered, with a higher pressure resulting in more collisions. The collision voltage can also be altered, and different collision voltages are required to break different bonds, with lower collision voltages resulting in daughter ions where weaker bonds were broken, and higher collision voltages producing daughter ions in which weaker and stronger bonds are broken.[16]

CID for structural analysis of organometallic compounds has special considerations in comparison to organic or bioorganic compounds. For example, the choice of ionization, a soft ionization technique is necessary as organometallic compounds could contain weakly bound, or transient ligands. Electrospray is the best option as a soft ionization source for most organometallic compounds. [16] Matrix assisted laser desorption ionization (MALDI) has also shown some good results.[17] As many organometallic compounds are air sensitive, these methods of ESI-MS and MALDI-MS need to be able to introduce the samples into the mass spectrometer in an air-free way if organometallic complexes are to be detected by those methods. Different ways of introducing air-sensitive samples include linking a glovebox to the ESI source such that a syringe being operated in an inert-atmosphere glovebox injects sample into the mass spectrometer.[18] A method of air-sensitive MALDI-MS is by using a glove bag around the MALDI source of the instrument in order to achieve air-free conditions. [16]

1.6 Solving identities of Peaks in Mass Spectra

Mass and isotope pattern prediction was done using ChemCalc.[19] ChemCalc can generate predicted mass spectra of chemical formulae or can generate chemical formulae when provided with accurate mass information. Both of these functions were used extensively in solving identities of experimentally determined *m/z* ratios.

1.7 Fourier Transform Infrared Spectroscopy (FTIR)

The dispersive technique of absorption spectroscopy works in the intuitive way of shining a monochromatic light at a sample and measuring how much of that light is absorbed by the sample, then repeating for each wavelength in a set range. Fourier Transform Infrared (FTIR) spectroscopy works in a less intuitive way yet yields the same or better results in much less time and is the standard for organic compound identification work.[20] At the heart of an FTIR is an interferometer consisting of a source, beamsplitters, two mirrors, a laser, and a detector. As shown in Figure 1.7, the light from the source travels to the collimating mirror to make the light into parallel rays. This collimated light then goes to the beamsplitter, a device that reflects some light and transmits some light causing a split into two parts of the incident light that hit it, one part goes to the moving mirror, while the other part goes to the fixed mirror. The moving mirror moves back forth at a constant velocity. The two beams get reflected from their respective mirrors and come together again at the beamsplitter. As the two beams travelled different distances their combination will happen as constructive or destructive interference. This recombined light goes from the beamsplitter to the sample, where the sample absorbs some of the light, and the transmitted light is detected by the detector. The detected signal is an interferogram which is signal versus mirror displacement of the moving mirror. This detected information is sent to a computer where a Fourier transform is performed to decompose the interferogram into the various frequencies that make it up to produce a single beam spectrum. This spectrum is compared to a background spectrum to produce a % transmittance spectrum, or further manipulated to convert to absorbances by taking the negative $\log_{10}$.

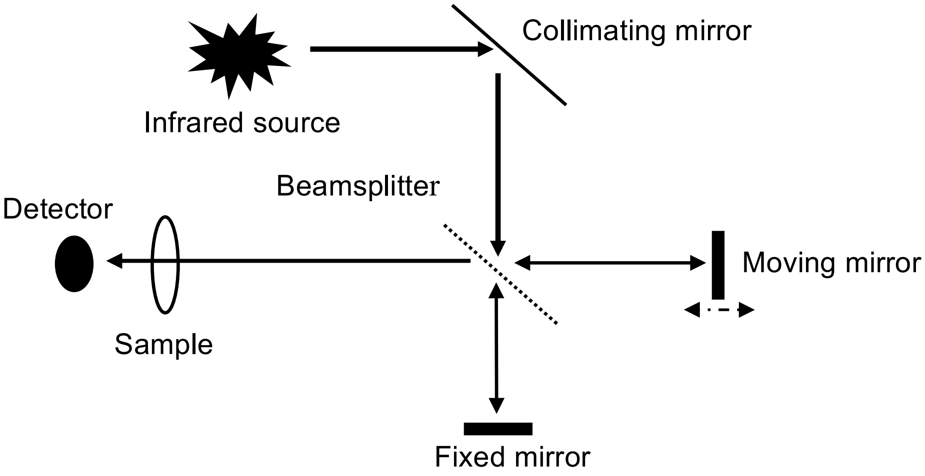

Figure 1.7. Schematic drawing of the optical path of a Michelson interferometer.[21]

1.8 Catalytic Reaction Monitoring

The study of organometallic catalytic reactions mechanisms is complicated by the nature of these homogeneous catalytic reactions. Intermediates are generally only present in solution at very low concentration and are unstable and reactive. Due to being so reactive, intermediates can interact with reagent as would be on-cycle, but could also react with impurities such as water, molecular oxygen, or cross contaminants. This means that strict control of reaction conditions need to be taken while monitoring the reactions.

There is two ways of studying organometallic catalytic reactions, firstly, monitoring what goes into a reaction, and what comes out of the reaction, the behaviour of these reactants and products can then be used to make predictions of the catalytic mechanism. Nuclear magnetic resonance (NMR) spectroscopy, ultraviolet-visible spectroscopy (UV-VIS), infrared (IR) spectroscopy, and labeling experiments are used study the overall kinetics of reaction and make deductions of what must be happening within the catalytic cycle. Secondly is the direct investigation of the catalytic mechanism, where emphasis is placed on detection of intermediates within a reaction. Computational chemistry and ESI-MS has been used in these type of investigations.

A good detection method should be specific and ideally measure both reactant disappearance and product formation. The method should not suffer interference from other reactants in solution, and should be usable within a large concentration range. [22]

NMR is specific, but not sensitive or fast,[23] while UV-VIS spectrometry is sensitive and fast, but not specific as absorption bands could be wide,[24] and intermediates could have chromophoric properties not much different than the reactant or product. IR spectroscopy is also fast, and is quite sensitive for certain absorption bands,[25] and can be extremely useful if the molecules studied contain carbonyls, as they generally have sharp, strong absorptions.[26] MS is a very fast technique, and also very sensitive to low concentrations of ions. These properties allows MS to detect intermediate species that might have short lifetimes in a reaction, and only ever be present in very low concentrations.[27]

NMR spectroscopy yields detailed information about physical and chemical environments of atoms in molecules and is thus very important for structural characterization of molecules. NMR is probably the most widely used characterization technique in chemistry, and has thus also been used extensively for studying catalytic reactions. The downfall of NMR in reaction monitoring is its inherent insensitivity and its slowness as a detection process. How slow it is as a detection method is due to the insensitivity giving rise to a need for multiple scan additions to produce one data point, and also due to inherent properties to the nuclei being studied, their magnetic relaxation times T^1 and T^2 limit the lowest time required for acquisition times. NMR spectroscopy also requires the use of a spin active nucleus, this limits what can be detected by NMR.[23]

NMR was used to study Rh catalyzed intermolecular hydroacylation reactions, where detection and characterizing of a key intermediate was done.[28,29] Due to the reactivity of that intermediate, its fast rate of reaction, and the slowness of the NMR experiment, the NMR tests were carried out under lowered temperature (-60^{o}C). At the lowered temperature the intermediate had a long enough lifetime to be detected by NMR. The mechanism of reaction was also further probed by utilizing a deuterium labeled aldehyde as reagent and finding the kinetic isotope effect (KIE). These studies yielded information about where the hydrogen from the aldehyde gets inserted into the unsaturated bond, and whether hydrogen/deuterium is directly involved in the rate determining step in the reaction.

1.8.1 Continuous Reaction Monitoring

As a reaction progresses, the concentrations of different species changes, and by continuously monitoring the reaction solution the dynamic trends of different species can give insight into what the role of that species is in a reaction. These trends are shown in Figure 1.8.

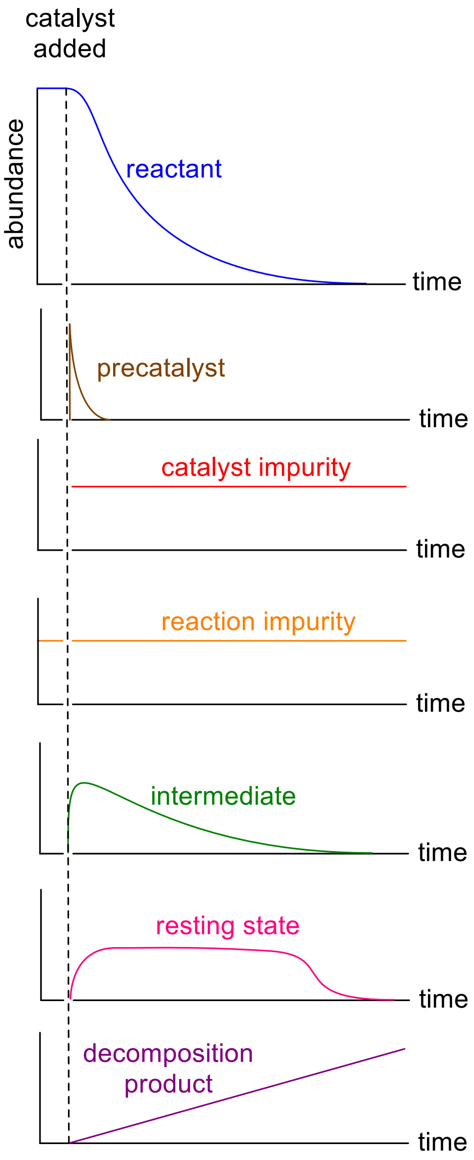

Figure 1.8. Expected dynamic trends of different species in a reaction.

Reactants are expected to decrease over time after the catalyst is added to the reaction and the precatalyst should go away at a rate that is linked to the initiation period. Any catalyst impurities which are not active in the reaction are expected to appear when catalyst is introduced, and stay constant throughout the duration of the reaction. Reaction impurities are expected to be present even before catalyst in added, and should also roughly stay constant throughout the reaction. Intermediates should have abundances related to the rate of the reactions they are involved in. The catalyst resting state is most abundant catalyst containing species during reaction, but it could change after all reactant is consumed. Catalyst decomposition products increase over time, and can be unrelated to the amount of reactant present.

To view an entire reaction, we use continuous direct infusion of reaction solution into the mass spectrometer. This is achieved by pressurized sample infusion (PSI) [30,31], leading to dense data of starting materials, intermediates, byproducts, and products as they form and disappear. There is also an assurance that nothing detectable was missed as can be the case in aliquot sampling of a dynamic process. PSI works by pressurizing the reaction solution flask while a narrow gauge PEEK tubing is inserted in the reaction solution. The overpressure pushes the solution through the PEEK tubing out of the flask and into the source of the ESI-MS, as the PEEK tubing is connected directly to the capillary at the source of the ESI-MS (Figure 1.9). The flow rate of the solution through the PEEK tubing and into the ESI-MS can be controlled by tubing diameter, overpressure applied, and tube length.[31] How these three factors affect the flow rate is described by the Hagen-Poiseuille equation.[32]

$$\Delta P = \frac{128\mu LQ}{\pi d^4} \tag{1.7}$$

Where ΔP is the loss of pressure, μ is the dynamic viscosity, L is the tube length, Q is the volumetric flow rate, d is the inner diameter of the tube.

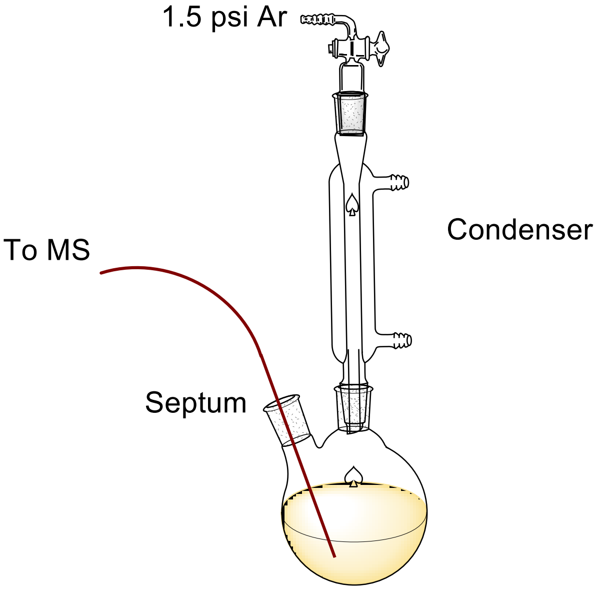

Figure 1.9. PSI-ESI-MS setup.

2 Relative Binding Affinities of Fluorobenzene Ligands in Cationic Rhodium Bisphosphine η^6-Fluorobenzene Complexes probed using Collision Induced Dissociation

Chapter 2 features contributions to a collaborative study with Prof. Andrew Weller (University of Oxford) that has now been published.[33] The focus of the collaboration was using collision induced dissociation (CID) to probe the binding affinities of various bisphosphine ligands previously synthesized by the Weller group. Two methods of CID were employed, ESI-MS variable exit–voltage (cone voltage) CID,[34–36] and collision cell CID.[37–39] Exit voltage CID is a method of achieving dissociation without requiring an instrument with MS/MS capabilities, as the fragmentation occurs inside the ESI source. The fragmentation occurs when high enough potentials are applied at the capillary exit, which acts to accelerate ions to collide with the desolvation gas. This paper emphasizes the utility of in-source CID for acquiring meaningful data on binding affinities of compounds as well as important characterization information.

2.1 Introduction

Mass spectrometry has been previously used to study the binding affinities of fluorobenzene with metal cations. In a study performed by Klippenstein et al., Fourier transform ion cyclotron resonance mass spectrometry (FTICR-MS) was used to study the rates of radiative association of Cr^+ with a set of fluorobenzene derivatives.[40] This study characterized the effects of electron withdrawing substituents on aromatic rings in weakening cation-π interactions. As expected, the study demonstrated that increasing the number of fluorine atoms on the arene resulted in a smaller η^6–(π) binding energy to the cation. Other studies have suggested that electrostatics play a role,[41,42] as the addition of a fluorine substituent reduces the negative charge located across the π region of the arene. The extreme example being hexafluorobenzene, where the π region on the arene would contain a partial positive charge.

Herein CID was used to determine comparative binding affinities of fluorobenzene ligands in a range of $[Rh(L_2)(\eta^6\text{–arene})]^+$ complexes, where the arene is varied and the ligand L_2 is one of the chelating phosphine ligands **2.1-2.7** (Scheme 2.1).

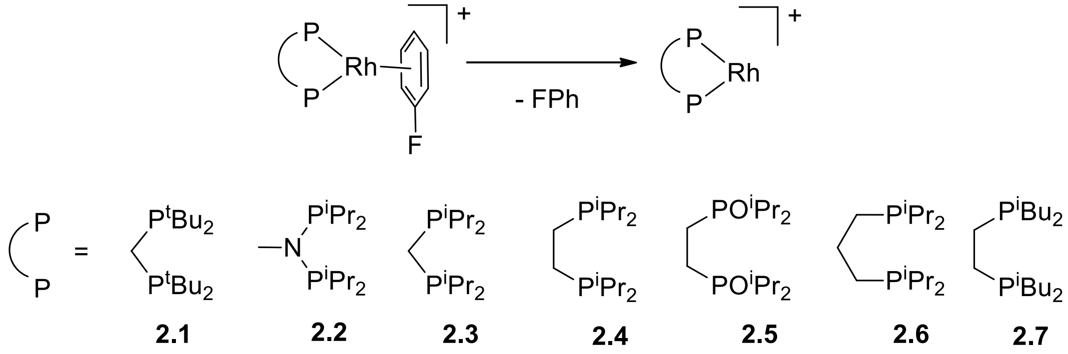

Scheme 2.1. Dissociation scheme for various Rh containing complexes that were tested. The anion is tetrakis[3,5-bis(trifluoromethyl)phenyl]borate ($[BAr^F_4]^-$).

2.2 Results and Discussion

In order to test the reliability of the variable exit–voltage ESI-MS technique, a selection of fluorobenzene bound rhodium bisphosphine complexes were screened using ESI-MS/MS. The fragmentation of a selected species is controlled by altering the voltage across an argon filled collision cell, producing trend lines as is shown in Figure 2.1, where higher collision voltages results in more fragmentation, thus a smaller percentage of arene bound to the complex.

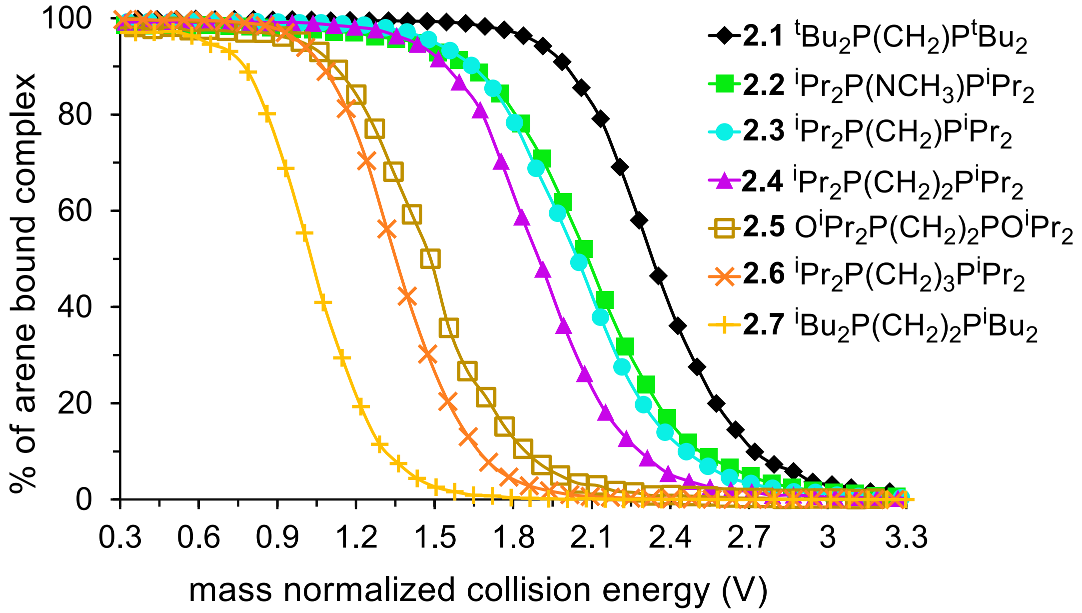

Figure 2.1. CID data from MS/MS of fluorobenzene ligand on rhodium complexes with ligands 1-7. Collision energy has been normalized to center of mass.

Complexes of phosphine ligands with ^{t}Bu groups had the highest binding affinity to fluorobenzene as more collision energy is necessary to dissociate the fluorobenzene while those complexes with ^{i}Bu groups or ^{i}Pr groups had lower binding affinities to fluorobenzene as dissociation occurred at a lower collision energy.

When comparing all the complexes that had ^{i}Pr as the R group on the phosphines (Figure 2.2), the binding affinity was found to increase with the increasing bite angle of the bisphosphine ligand, indicating that large bite angles can negatively influence the binding affinity of the arene ligand.

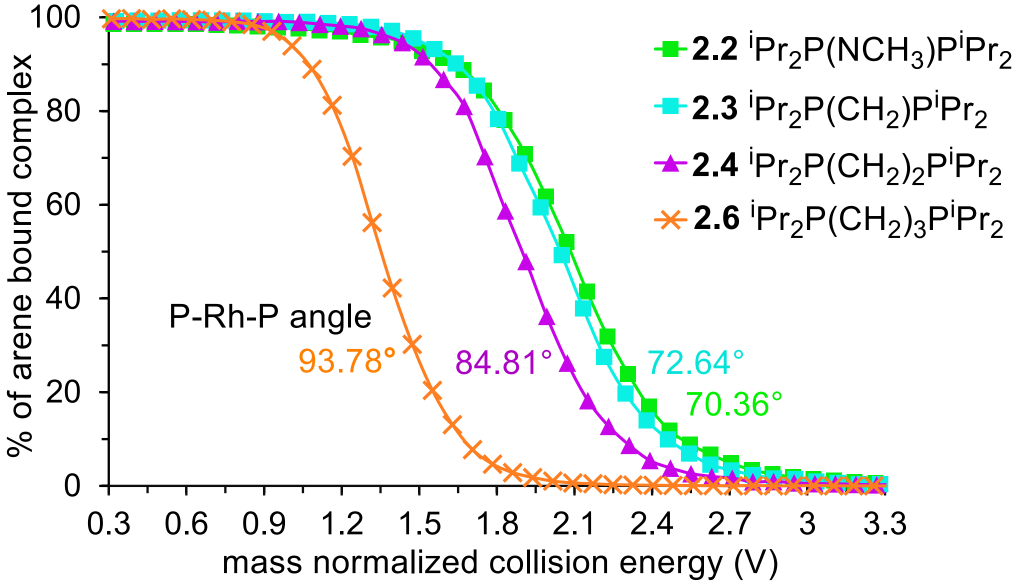

Figure 2.2. CID data from MS/MS of fluorobenzene ligand on rhodium complexes 2, 3, 4 and 6 comparing trends for isopropyl bearing bisphosphine ligands. P-Rh-P binding angles from crystallographic data.[28] Collision energy has been normalized to center of mass.

In order to determine the effect of sterics of the arene on the binding strength of the η^6 arene group, CID data was collected for various arene ligands in the complex [Rh (L_2) – η^6 arene]$^+$ where L_2 is ligand **2.2** (Scheme 2.2). This was accomplished by adding a more strongly binding arene to a fluorobenzene solution of [Rh(**2.2**)(η^6–FPh)]$^+$ to displace the FPh and produce the different arene coordinated analogue.

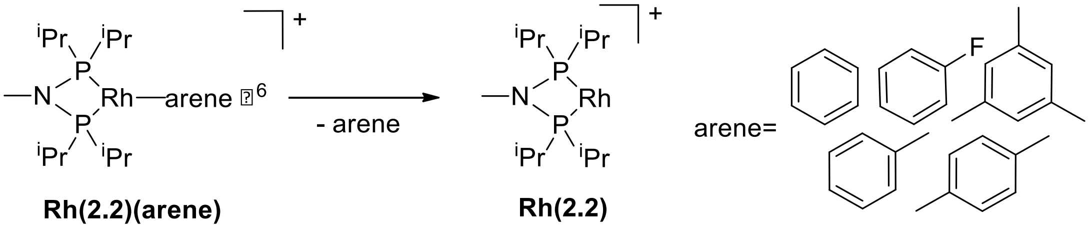

Scheme 2.2. Dissociation scheme for [Rh(2.2) η^6 – (arene)]$^+$ complexes, where arene is fluorobenzene, benzene, toluene, xylene, or mesitylene, the anion is $[BAr^F_4]^-$.

The resulting arene complex was probed by ESI–MS in each case, and each complex was selected for CID and fragmented (Figure 2.3).

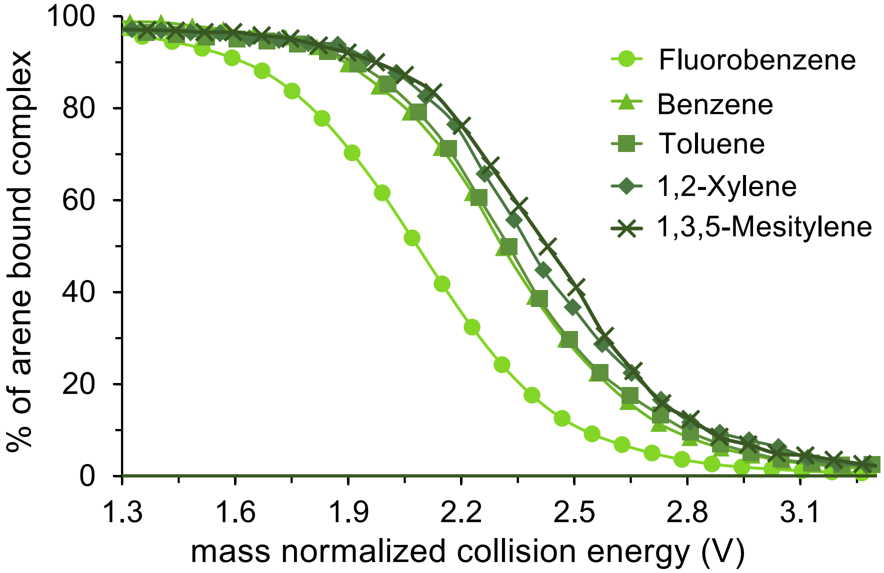

Figure 2.3. CID data form MS/MS of arene ligands complexes [Rh(arene)(2)]$^+$

The data in Figure 2.3 show that the fluorobenzene complex is substantially easier to fragment than any of the hydrocarbon-only arenes. The remaining four complexes [Rh(**2**)(C_6H_{6-n} Me_n)]$^+$ (n = 0-3) dissociate their arene at about the same collision energy. There is a slight trend of electron-rich arenes being more difficult to dissociate despite steric effects acting to weaken the strength of the metal-ligand bonding.

Finally, the data obtained using the collision cell CID method was compared to that obtained using the in-source CID method (Figure 2.4). The 50% fragmentation voltages for collision cell CID experiments against the in-source CID values shows a good, almost linear, correlation; demonstrating the validity of both approaches to produce a qualitative ordering.

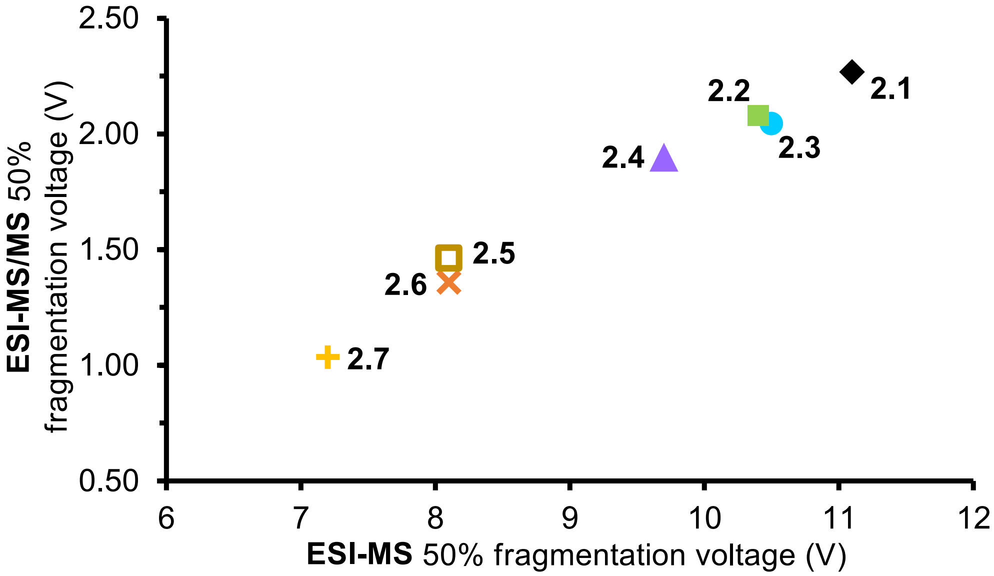

Figure 2.4. Correlation between exit voltage ESI-MS experiments and collision cell ESI-MS/MS experiments.

2.3 Conclusions

A collection of CID experiments were performed to probe the relative dissociation energy of an arene from a variety of η^6-arene complexes of the type $[Rh(L_2)(\eta^6\text{-arene})][BAr^F_4]$. These experiments showed that the sterics of the phosphine substituents influences the binding affinity of η^6-C_6H_5F, with ^{t}Bu groups demonstrating the greatest binding affinities, while ^{i}Pr and ^{i}Bu groups demonstrated the least of those tested. The bite angle of the bisphosphine ligands were also seen to influence the binding affinity of the arene with smaller bite angles increasing binding affinity. Increasingly electron withdrawing substituents on the arene reduced the binding affinity of the arene and more electron-rich arenes had a greater binding affinity. Overall, it is likely that these trends reflect a combination of arene binding strength and stabilization of the low–coordinate $[Rh(L_2)]^+$ fragment in the gas–phase. These simple in-source and collision cell CID experiments can be performed without any extra modifications to standard ESI-MS(/MS) instruments, and are potentially useful processes for the qualitative comparison of the relative stabilities of various organometallic complexes.

2.4 Experimental

Solvents were HPLC grade and purified on an MBraun solvent purification system. Standard Schlenk technique was used to achieve air-free conditions. ESI-MS/MS experiments were recorded using a Micromass Q-Tof *micro* instrument in positive ion mode using pneumatically assisted electrospray ionization. Typical experimental parameters were: capillary voltage, 2900 V; sample cone voltage, 15V; extraction voltage, 0.5 V; Source temperature, 84°C; desolvation temperature, 184°C; cone gas flow, 100 L/h; desolvation gas flow, 200 L/h; MCP voltage, 2400 V. Samples were prepared by dilution in fluorobenzene to a concentration of 0.15 mM and introduced into the source at 10mLmin^{-1} via a syringe pump. Data collection was carried out in continuum mode and spectra were collected by selecting the parent ion of interest by the quadrupole. A scan time of 5 s per spectrum was used. The collision cell voltage was set to 0 V initially and increased by increments of 1 V per scan, up to a maximum of 60 V using the program Autohotkey (freely available from http://www.autohotkey.com/). Resultant data was corrected to the centre of mass according to the formula

$$\mathrm{E}_0 = \frac{\mathrm{E}_{\mathrm{lab}} \times \mathrm{m}_A}{(\mathrm{m}_A + \mathrm{m}_l)} \tag{2.1}$$

where E_{lab} is the collision cell voltage, m_A is the mass of the collision gas and m_I is the mass of the target ion. In the case of studying the differing effects of different arenes, a small volume (0.1-0.3 mL) of an arene was added into a solution of **1** in fluorobenzene. The solution was let stir for 2 hours before data collection was initiated.

Rhodium complexes were synthesized according to literature methods and in-source CID was performed by the Weller group.[28,43]

3 Exploring the Mechanism of the Hydroboration of Alkenes by amine–boranes Catalysed by $[Rh(xantphos)]^+$

Chapter 3 features contributions to a collaborative study with Prof. Andrew Weller and coworkers (University of Oxford) that resulted in a publication[44]. The full work was a mechanistic study of hydroboration of amine-boranes utilizing NMR for initial rate and isotope labeling experiments, and PSI-ESI-MS for reaction profile and resting state determination. My contribution was in the PSI-ESI-MS experiments. This publication showed that $[Rh(xantphos)]^+$ fragments act as effective catalysts at 0.5 mol % catalyst loadings for hydroboration of the alkene tert-butylethene (TBE) using the amine-borane $H_3B{\cdot}NMe_3$ and yields the linear product. Reductive elimination of the product was shown to be the likely rate limiting step of this reaction, and the system was shown to be ineffective for other alkenes such as 1-hexene or for phosphine-boranes as that resulted in decomposition and P-B bond cleavage. This work adds to the scientific understanding of how catalytic reactions, specifically this hydroboration reaction, progresses from substrates to products.

3.1 Introduction

Hydroboration, the addition of a B-H bond across an unsaturated C-C bond, is a versatile reaction that produces organoboranes which can be further functionalized leading to important products in organic synthesis.[45] Transition metal catalyzed hydroboration allows for control of regioselectivity of hydroboration. [46–50] Four coordinate amine-boranes (generally $H_3B{\cdot}NMe_3$) have been used in uncatalyzed hydroboration reactions where the N-B bond cleavage is proposed to produce a reactive

BH_3 molecule,[51] while iodine-induced hydroboration is proposed to operate via an intermediate that retains the B-N bond.[52] The role of transition metal catalysts in these processes has also been studied.[51,53–55] Amine-boranes have potential as hydrogen storage materials and as precursors in oligomeric and polymeric B-N materials that can be produced through dehydrocoupling. These B-N polymers are isoelectronic to traditional carbon polymers, and may prove to have interesting and useful properties.[55]

3.2 Results and Discussion

The mechanism of the reaction (Scheme 3.1) was investigated through NMR studies of initial rates and isotopic labeling. These experiments determined that the likely rate limiting step is reductive elimination of the linear hydroboration product **3*P*** and that the alkene and borane activations are reversible. The resting state of the system was probed using PSI ESI-MS.

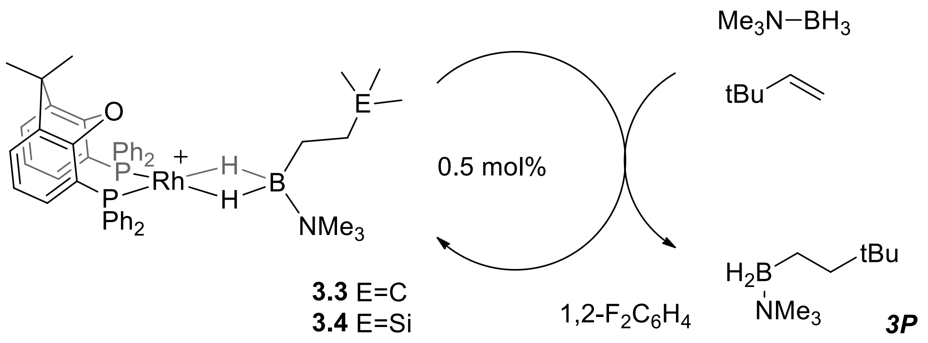

Scheme 3.1. Catalytic hydroboration of TBE and $H_3B{\cdot}NMe_3$ with $[Rh(xantphos)]^+$. $[Bar^F{}_4]^-$ anions not shown.

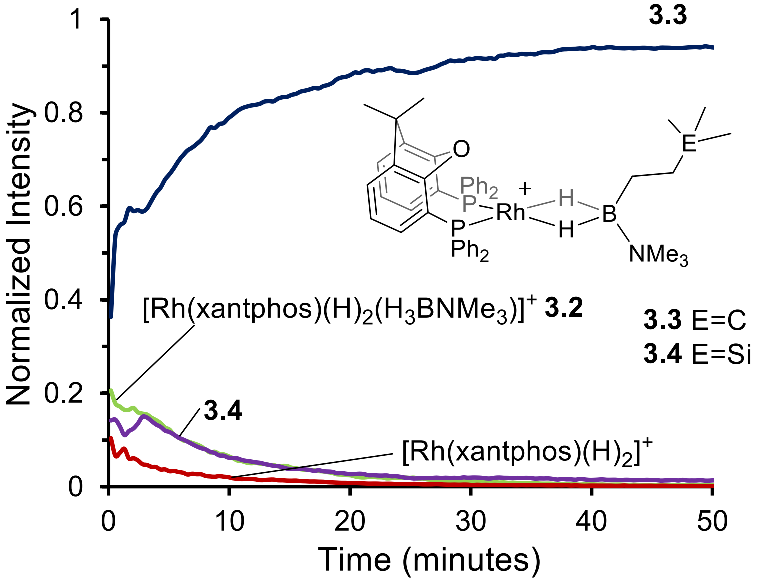

Figure 3.1. PSI ESI-MS reaction profile of TBE with $H_3B{\cdot}NMe_3$ catalysed by 3.4. Conditions: $H_3B{\cdot}NMe_3$, 0.006 M, TBE 0.013 M; 3.4, 0.001 M, 1,2-$F_2C_6H_4$. The reaction proceeded to 80% conversion.

The change in resting state from **3.4** to **3.3** was probed using PSI ESI-MS. The advantage of this technique is that it allows for very high data density over a wide dynamic range, in comparison to NMR. It is also ideal for analysing complex mixtures, as separated occurs within the MS and ideally each species produces a single signal on the mass spectrometer. Thus this technique is extremely well suited to analyzing the evolving mixture which is a catalytic reaction. Figure 3.1 shows the temporal profile of the catalytic reaction using **3.4**. This experiment was run at 15 mol%, which was determined to be the best conditions for the optimal concentration necessary for PSI ESI-MS. At the start of the reaction the resting state of the catalyst moves from **3.4** to **3.3**, consistent with the NMR experiments. These ESI-MS experiments also revealed the presence, at early stages of the reaction of three other species. The first is identified as $[Rh(xantphos)(H_3B{\cdot}NMe_3)]^+$, (*m/z* = 754.24; calc. 754.20). This species could be a Rh(I) sigma-bound amine–borane complex, or a Rh(III) B–H activated hydrido-boryl. $[Rh(xantphos)(H_2)]^+$ (*m/z* = 683.15; calc. 683.11) and $[Rh(xantphos)(H)_2(H_3B{\cdot}NMe_3)]^+$ (**3.2**) are also observed, a small amount of **3.2** is suggested to form parallel with **3.5** during catalysis as shown in Scheme 3.2.

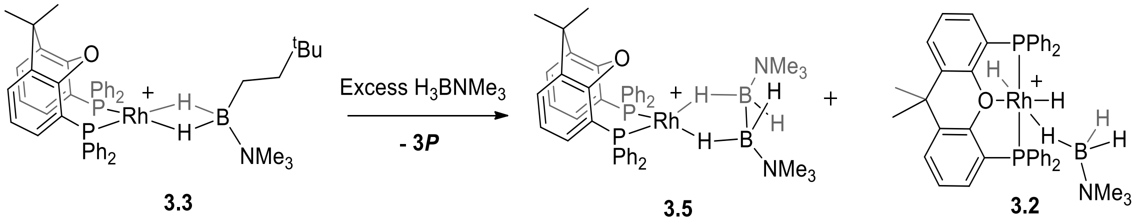

Scheme 3.2. Formation of complex 3.5 upon addition of excess $H_3B{\cdot}NMe_3$ to 3.3. $[Bar^F{}_4]^-$ anions not shown.

$[Rh(xantphos)(H_3B{\cdot}NMe_3)]^+$ and **3.2** decay at a very similar rate to **3.3**, suggesting that the build-up of the hydroboration product **3*P*** during catalysis pushes any equilibria to favour **3.2**. This observation is also consistent with product inhibition from initial rate experiments.

3.3 Conclusions

$[Rh(xantphos)]^+$ fragments act as effectives catalyst for hydroboration of TBE using the amine-borane $H_3B{\cdot}NMe_3$. The reaction was initially studied by the Weller group using initial rate methods and labeling studies that suggested that reductive elimination of the linear hydroboration product is rate limiting in the early stages of catalysis. PSI ESI-MS was used to study this reaction, and more information about the reaction was gained. Rhodium hydride species that were not detected by ^1H NMR spectroscopy was observed by MS, demonstrating that ESI-MS is much more sensitive to their observation than ^1H NMR.

3.4 Experimental

All manipulations were performed under an argon or nitrogen atmosphere using standard Schlenk and glove-box techniques. Glassware was oven dried at 130 °C overnight and flamed under vacuum prior to use. Pentane, hexanes, CH_2Cl_2 and MeCN were dried using a Grubbs type solvent purification system (MBraun SPS-800) and degassed by successive freeze–pump–thaw cycles. 1,2-$F_2C_6H_4$ was dried over CaH_2, vacuum distilled and stored over 3 Å molecular sieves. $H_3B{\cdot}NMe_3$ was purchased form Aldrich and sublimed prior to use. TBE was purchased from Aldrich dried over CaH_2 and vacuum distilled prior to use.

ESI-MS reaction monitoring by PSI was performed accordingly: A Schlenk flask under nitrogen containing **3.4** (4.7 mg, 0.0028 mmol) and $H_3B{\cdot}NMe_3$ (1.4mg, 0.019 mmol) was pressurized to 1.5 psi using 99.998% purity argon gas and connected to the mass spectrometer *via* a short length of PEEK tubing. Collection on the mass spectrometer was initiated. A solution of TBE (4.8uL, 0.038 mmol) in 1,2-$F_2C_6H_4$ (3 mL) was injected into the pressurized Schlenk flask through a septum. Mass spectra were collected on a Micromass Q-ToF *Micro* mass spectrometer in positive ion mode using pneumatically assisted electrospray ionization: capillary voltage, 2900 V; sample cone voltage, 15V; extraction voltage, 0.5 V; Source temperature, 92°C; desolvation temperature, 192°C; cone gas flow, 100 L/h; desolvation gas flow, 200 L/h; collision voltage, 2 V; MCP voltage, 2400 V. Data was summed over 10 seconds, no further smoothing of the data was performed.

Synthesis of $Rh(\kappa^2{}_{P,P}\text{-xantphos})(\kappa^2\text{-}H_2B(CH_2CH_2SiMe_3){\cdot}NMe_3$ and other experimental procedures are described elsewhere.[44]

4 Rh Catalyzed Selective Partial Hydrogenation of Alkynes

Chapter 4 features my contribution to a collaborative study with Dr. Jingwei Luo (University of Victoria) and Prof. Andrew Weller and coworkers (University of Oxford) that resulted in admission of a manuscript to *Organometallics*, that has been accepted with pending revisions.[56] This work was the mechanistic study of the hydrogenation of a charge-tagged alkyne $[Ph_3P(CH_2)_4C_2H]^+[PF_6]^-$, catalyzed by a cationic rhodium complex $[Rh(P^cPr_3)_2(\eta^6\text{-FPh})]^+[B\{3,5\text{-}(CF_3)_2C_6H_3\}_4]^-$ (P^cPr_3 = triscyclopropylphosphine, FPh = fluorobenzene) PSI ESI-MS was used to monitor reaction progress. This work demonstrates the use of ESI-MS in conjunction with NMR, kinetic isotope effects and numerical modeling using Copasi[57] for determining a mechanism of reaction.

4.1 Introduction

Rhodium catalyzed hydrogenation of alkenes and alkynes is a classic catalytic organometallic reaction.[58–60] The mechanism of the reaction has been studied by a wide range of methods.[61–69] It is a complicated reaction, beyond the catalytic species there are off-cycle equilibria between catalyst dimers and monomers along with the hydrogenated versions of both the dimers and the monomers and between di- and tri-phosphine species. The reaction has been studied by our group as well, using ESI-MS, where a charged phosphine ligand $[Ph_2P(CH_2)_4PPh_2Bn]^+[PF_6]^-$ was doped into a reaction mixture consisting of an alkene, hydrogen and Wilkinson's catalyst, using chlorobenzene as a solvent.[70] A large variety of rhodium complexes consistent with the known speciation of this reaction mixture were observed. Because ESI-MS operates only on ions, the overall progress of the reaction was not tracked. Using a charged substrate allows for the tracking of that charged species throughout its progress in the catalytic cycle, ideally permitting monitoring of overall reaction progress as well as observation of intermediates that include that charged species. The use of a charge-tagged substrate is shown in our study of the hydrogenation of a charged alkyne by Wilkinson's catalyst.[71]

Cationic rhodium complexes are known for hydrogenation of alkynes from Schrock and Osborn's work,[72] and since then these type of complexes have served as precursors in various studies of homogeneous (especially enantioselective) catalysis.[73–78]

4.2 Results and Discussion

The reaction profile of the hydrogenation of a charge-tagged alkyne $[Ph_3P(CH_2)_4C_2H]^+[PF_6]^-$, catalyzed by a cationic rhodium complex $[Rh(P^cPr_3)_2(\eta^6\text{-}FPh)]^+[B\{3,5\text{-}(CF_3)_2C_6H_3\}_4]^-$ shown in Figure 4.1 was found to be very different from that catalyzed by Wilkinson's catalyst, $Rh(PPh_3)_3Cl$. For Wilkinson's catalyst the rate of the alkyne hydrogenation was found to be three times faster than the rate of the alkene hydrogenation, and the turnover limiting step was found to be phosphine dissociation from the $Rh(PPh_3)_3Cl$ to form the 14- electron active catalyst $Rh(PPh_3)_2Cl$. [71] For the catalyst $[Rh(P^cPr_3)_2(\eta^6\text{-}FPh)]^+[B\{3,5\text{-}(CF_3)_2C_6H_3\}_4]^-$ the alkyne hydrogenation was found to be about 50 times faster than the hydrogenation of the alkene, and production of the hydrogenated product was zero order in alkyne or alkene. No intermediates were observed that included both rhodium and the charged tag.

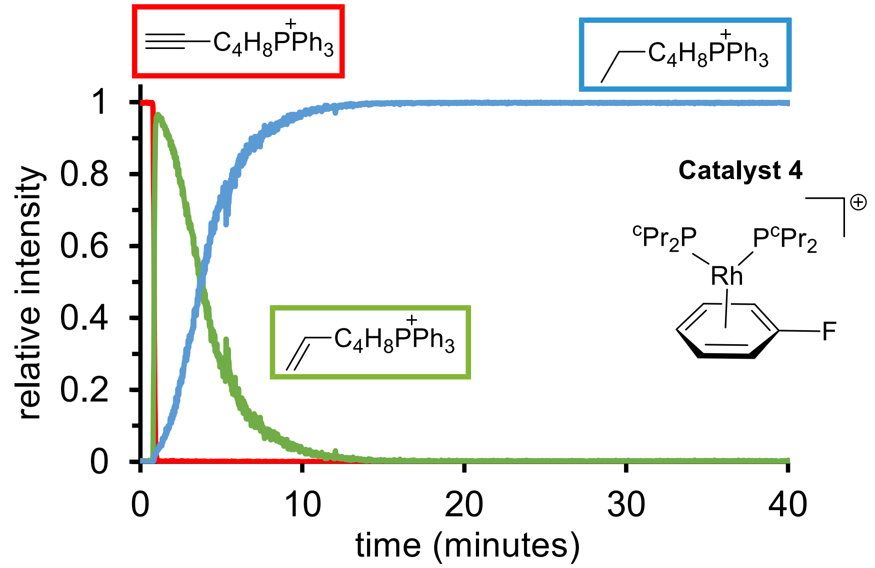

Figure 4.1. Hydrogenation of a charge tagged alkyne $[Ph_3P(CH_2)_4C_2H]^+[PF_6]^-$. by $[Rh(P^cPr_3)_2(\eta^6\text{-}PhF)]^+[B\{3,5\text{-}(CF_3)_2C_6H_3\}_4]^-$ as the catalyst.

This complete work presents three different possible mechanisms (Path A, B, C) of hydrogenation that could be present, and throughout the work, evidence is presented towards determination of the dominant mechanism. The three possible mechanisms are shown in Figure 4.2.

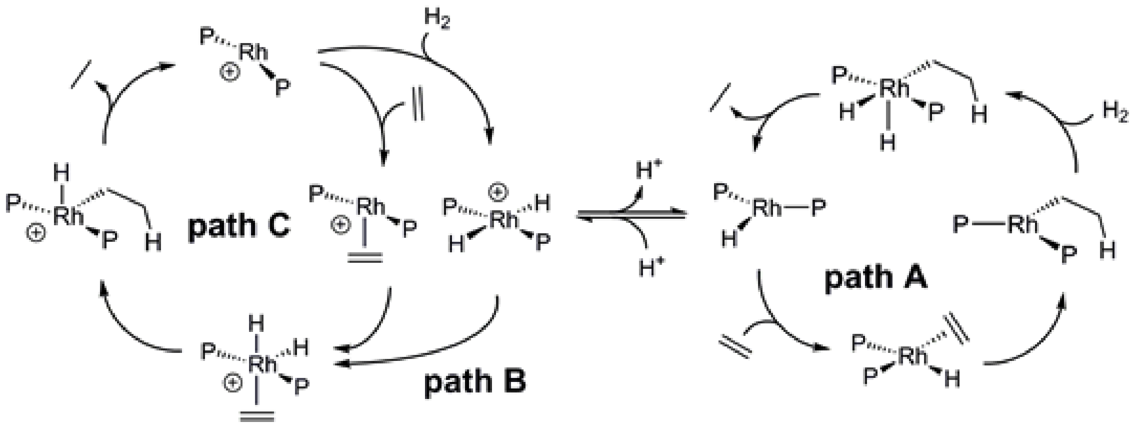

Figure 4.2. Three possible mechanisms of alkene hydrogenation by a cationic rhodium complex proposed by Osborn and Schrock .[72]

Path A involves addition of H_2 to $[RhL_n]^+$ then deprotonation to form an active neutral catalyst of the form $RhHL_n$ which is followed by alkene coordination, migration, H_2 addition, and reductive elimination of an alkane. Path B involved addition of H_2 then coordination of alkene to $[RhH_2L_n]^+$, followed by migration and reductive elimination of the product alkane. Path C is the same as Path B, except the order of H_2 and alkene reactivity is reversed. Osborn and Schrock considered path A to predominant in the polar solvents acetone, 2-methoxyethanol and tetrahydrofuran, except where binding of the alkene was particularly strong, such as in the selective hydrogenation of dienes.[72]

All three mechanisms were considered as possible candidates to explain our observations, which were:

(a) When examining $[RhP_2(FPh)]^+$ in the presence of H_2 by ^{1}H NMR spectroscopy, neither $RhHL_n$ (Path A) nor $[RhH_2L_n]^+$ (Path B) could be detected.

(b) $RhHP_2$(alkene), $RhRP_2$ and RhH_2RP_2 were not observed. If Path A was operative, any of these intermediates would be expected to be observable as monocations (due to the charged tag) using ESI-MS. If Path A was operative, at least one of these should be detected.

(d) Neither Path A nor Path B provided sensible solutions with numerical modeling. Numerical modelling proved most tractable for Path C, with excellent correlation to experimental data. These numerical modeling experiments showed that there exist plausible sets of rate constants for Path C that fit nicely to the experimental data, while none could be found for Path A or Path B.

Together these results pointed towards an operable Path C, to strengthen the arguments further, the effect of a base on the reaction was tested. Addition of bases such as triethylamine ought to accelerate reactions proceeding through a fast Path A thanks to the deprotonation equilibrium being perturbed in the direction of $RhHP_2$.

This was tested through monitoring by ESI-MS the addition of 5 equivalents (to catalyst) of triethylamine to the reaction solution. Acceleration of the overall reaction was not observed. Instead, the reaction was slowed in the presence of triethylamine (Figure 4.3), and the reaction became less selective for the alkyne over the alkene. The reaction reached a maximum of 50% in alkene only, very similar to the degree of selectivity exhibited by Wilkinson's catalyst.[71]

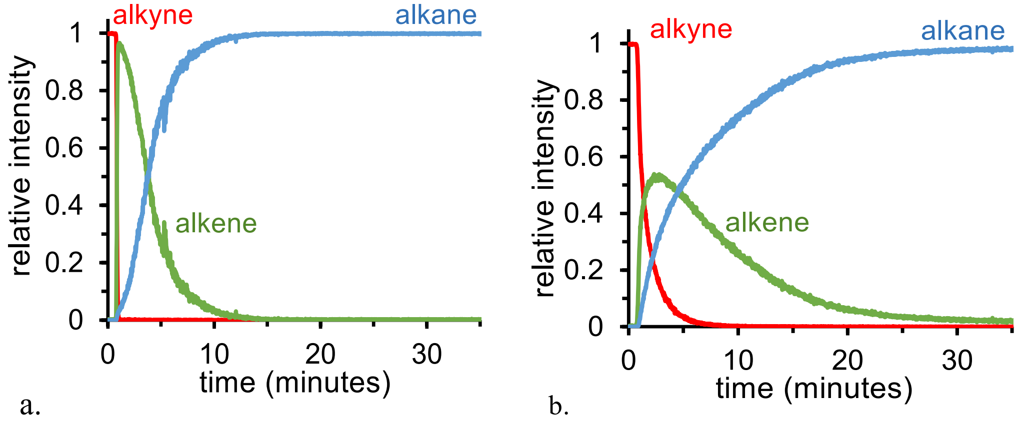

Figure 4.3. a. PSI ESI-MS traces for the control reaction, $[Ph_3P(CH_2)_4C_2H]^+[PF_6]^-$ (2.4mM), 3 psi hydrogen gas, $[Rh(P^cPr_3)_2(\eta^6\text{-FPh})]^+[BAr^F{}_4]^-$ (10% catalyst loading) in FPh.
b. PSI ESI-MS traces for reaction of $[Ph_3P(CH_2)_4C_2H]^+[PF_6]^-$ (2.4mM), 3 psi hydrogen gas, $[Rh(P^cPr_3)_2(\eta^6\text{-FPh})]^+[BAr^F{}_4]^-$ (10% catalyst loading) with NEt_3 (5 equiv. 1.2mM) in FPh.

The addition of NEt_3 to $[RhP_2]^+$ in the presence of H_2 was also tested, and resulted in disappearance of the signal due to $[RhP_2]^+$ and the appearance of $[HNEt_3]^+$, suggesting the formation of neutral $RhHP_2$. Which could be active during reaction conditions including the basic trimethylamine, forcing the reaction to go by Path A. Under the forced Path A conditions the reaction showed much less selectivity for the alkyne over the alkene, suggesting that Path A is less selective to alkynes than Path C or Path B.

4.3 Conclusions

Experiments revealed that the hydrogenation of an alkyne catalyzed by a cationic rhodium complex $[Rh(P^{c}Pr_3)_2(\eta^6\text{-}FPh)]^+[B\{3,5\text{-}(CF_3)_2C_6H_3\}_4]^-$ is first order in catalyst and first order in hydrogen. Alkyne hydrogenation was much faster than alkene hydrogenation. The turnover-limiting step is proposed to be oxidative addition of hydrogen to the alkyne (or alkene) bound complex, and this explains the observed primary kinetic isotope effect of $k_H/k_D = 2.1 \pm 0.2$. Addition of triethylamine caused a dramatic reduction in rate, suggesting a deprotonation pathway is not the active mechanism. All this evidence pointed to the operative mechanism being Path C, which was also supported by numerical modeling, Path C involves coordination of alkene to $[RhL_n]^+$, followed by addition of H_2, then migration and reductive elimination of the product alkane.

4.4 Experimental

Fluorobenzene was freshly distilled from CaH_2 before use. All other solvents were dispensed from an MBraun solvent purification system immediately before use. All reactions were under nitrogen or argon atmosphere. Chemicals and solvents were purchased from Aldrich and used without subsequent purification. The charged alkyne was prepared by a previously published method.[71] All mass spectra were collected by using a Micromass Q-Tof *micro* mass spectrometer in positive ion mode using pneumatically assisted electrospray ionization: capillary voltage, 3000 V; extraction voltage, 0.5 V; Source temperature, 90°C; desolvation temperature, 180°C; cone gas flow, 100 L/h; desolvation gas flow, 100 L/h; collision voltage, 2 V (for MS experiments); collision voltage, 2-80 V (for MS/MS experiments); MCP voltage, 2700 V.

ESI-MS reaction monitoring using pressurized sample infusion. A Schlenk flask was used for these experiments. A 10 ml fluorobenzene solution of [**3**][PF_6] (10-20 mg, 2.1-4.2 mM) was monitored using the PSI-ESI-MS setup. The Schlenk flask was pressurized to 3 psi using 99.999% purity hydrogen gas. $[Rh(P^{c}Pr_3)_2(\eta^6\text{-FPh})]^+[BAr^F{}_4]^-$ (1.0-6.0 mg, 0.75-4.5 μmol, 1-20% catalyst loading) was dissolved in 1 mL of fluorobenzene and injected into the well-stirred Schlenk flask via a septum. The solution end of PEEK tubing was protected with a standard cannula filter system to avoid the tube being blocked by any insoluble by-products. Data were processed by normalizing the abundance of each species to the total ion count of all species identified as containing the tag. No smoothing of the data was performed.

Compounds were synthesized according to literature methods,[71] further experimental contributions can be found in the publication that resulted from this work.[56]

5 Multiple methods of Realtime Monitoring of a Hydroacylation reaction

Chapter 5 features contributions to a collaborative study with Prof. Andrew Weller (University of Oxford). The Weller group developed the catalyst used in this study, $[Rh(P(^iPr)_2NMeP(^iPr)_2)FPh]$ [tetrakis[3,5-bis(trifluoromethyl)phenyl]borate] ($([BAr^F{}_4]^-)$) **5.A**, and had published before on its use as a hydroacylation catalyst.[28] They characterized the catalyst by NMR and ESI-MS, and studied its activity compared to other similar rhodium catalysts for the hydroacylation of a β-S-substituted aldehyde with 1-octene and 1-octyne. They found that the catalyst was active at 1% catalyst loadings, and was selective for alkynes over alkenes. The work in this chapter expands uses this system to showcase a new concept for mechanistic analysis: coupling of an orthogonal spectroscopic technique with PSI-ESI-MS. The reaction was studied by PSI ESI-MS while employing charged tags, allowing for observation of key intermediates, and interesting chemical discoveries. The use of IR in conjunction with ESI-MS led to rate information about the overall reaction along with dynamic information about catalytic speciation. The work in this chapter illustrates the power of coupling multiple methods of detection together in the study of catalytic reactions. Coupling of these techniques allows for detection over many magnitudes of concentration, and creates a more complete picture of what is happening within catalytic reaction mechanism which all too often is seen as a “black box”.

5.1 Hydroacylation Literature Review

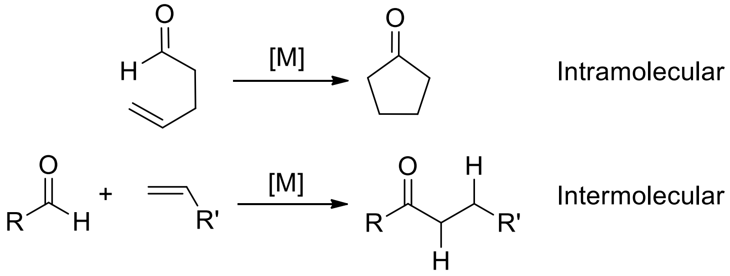

Scheme 5.1. General hydroacylation reaction of an alkene.

Hydroacylation is an atom economical addition of a hydrogen and an acyl group across a C-C multiple bond (double or triple bond). This is a powerful reaction for commercial applications. Great development of the hydroacylation reaction has occurred in the last 30 years, including the expansion of the scope of the reaction to the minimization of deleterious side reactions. The first hydroacylation reaction was reported by Sakai in 1972 in his work on the synthesis of prostanoids,[79] in an intramolecular reaction which employed chlorotris-(triphenylphosphine)rhodium (I) (Wilkinson's catalyst) to convert 1-al-4-enes into cylopentanones at room temperature. In Sakai's work a significant side product was also observed, the cyclopropane derivative produced from decarbonylation. Subsequently, the scope of intramolecular hydroacylation was expanded upon by Milstein.[80] Success in intramolecular hydroacylation led to the development of the intermolecular analogue. During these developments the majority of hydroacylation catalysts to this day still continue being rhodium centres. Intermolecular hydroacylation was first reported by Miller in 1980.[81] The move to intermolecular systems presented new challenges. Successful intramolecular systems would not necessarily work for the intermolecular processes. In the intramolecular reaction, after the first coordination event, the subsequent coordination is no longer disfavoured by entropy, and would be expected to happen much faster. When combining two different molecules at the catalyst, as is required in intermolecular hydroacylation, two different coordination events must occur independently of each other. This translates to a larger potential window of time that exists after the coordination of the first substrate and before the next coordination event for the. The intermediate species that is formed is unstable and can undergo decomposition. The most likely path of decomposition at this step of the reaction is reductive decarbonylation.[82] Another possible side reaction is the aldol reaction, this has been found to occur when alkyl aldehydes are employed.[83]

The mechanism of hydroacylation is proposed to go by oxidative addition of an aldehyde to the metal centre forming an acyl-hydride intermediate that is prone to reductive decarbonylation. This is followed by coordination of the alkene (alkyne) to the metal and 1,2-insertion of the alkyl into the M-H bond. The processed is finished off by reductive elimination of the product ketone.[84] (Scheme 5.2)

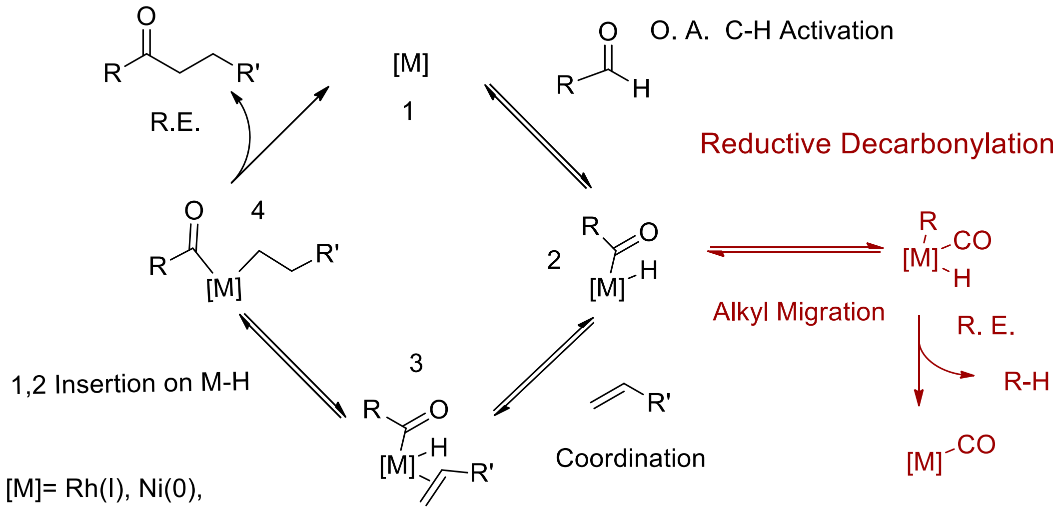

Scheme 5.2. Hydroacylation reaction mechanism.

Support for this mechanism is was found in the work of Suggs in 1978 where he isolated an acyl-hydride intermediate and showed it to be active in the hydroacylation reaction, reporting a 55% product yield (Scheme 5.3) .[82] He found that decarbonylation does not happen at room temperature on the isolated intermediate, and proposed that the reason for this is that the four-membered ring that would be an intermediate towards decarbonylation is not expected to be stable.

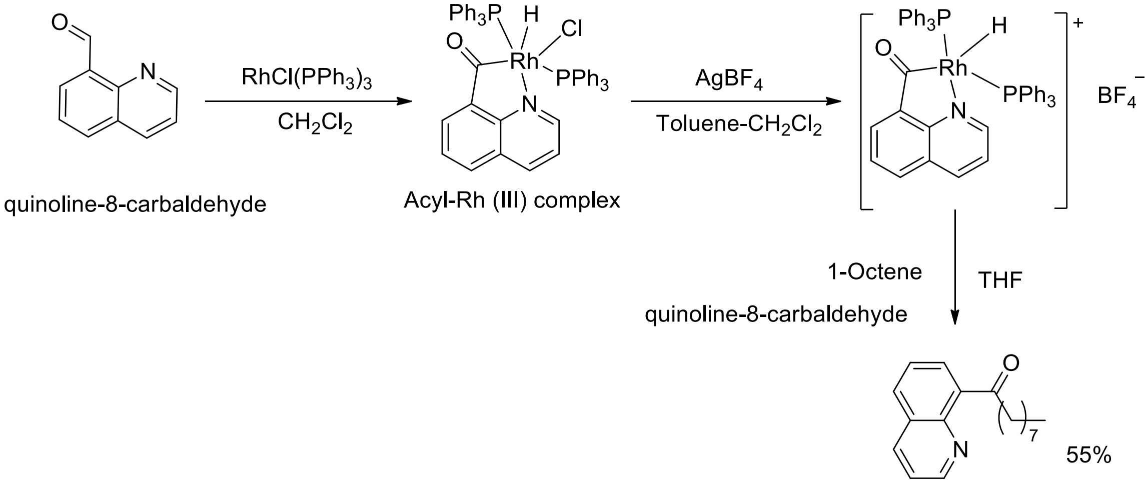

Scheme 5.3. Suggs' isolation of Rh(III) acyl-hydride complex, and subsequent reactivity as a hydroacylation catalyst.

Minimizing reductive decarbonylation has been seen as the key to development of successful catalytic systems, as the decarbonylation process yields an unreactive catalyst, and breaks down the substrate aldehyde, minimizing yield and consuming resources. Optimizing reaction conditions for the minimization of decarbonylation is possible. The use of a carbon monoxide atmosphere to disfavour the forward reaction of decarbonylation has been employed.[85] Coordinating solvents or an excess alkene or alkyne can be used to stabilizing the acyl-hydride intermediate by blocking vacant sites and disfavouring decarbonylation (Figure 5.1).[86] Acetone is a solvent commonly used for hydroacylation reactions as it is weekly coordinating, such that it does not slow the overall reaction by coordinating too strongly to the intermediate, but does interact well enough in order to stabilize against decarbonylation.

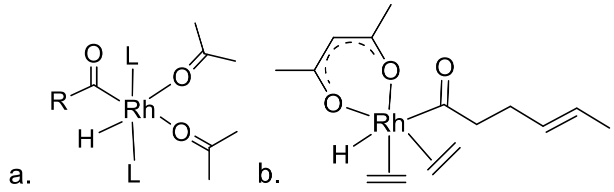

Figure 5.1. Stabilization of acyl-hydride intermediates by: a. solvents, b. excess substrate.

Chelation of the aldehyde to the metal centre, or chelation of the alkene to the metal centre has also shown great worth as a strategy to deal with decarbonylation and the aldol process can be suppressed by changing certain reaction conditions.[83] The first intermolecular hydroacylation was described by Miller [81] in 1980, where enals were employed as the aldehyde and the reaction was a coupling of an enal and ethylene as shown in Scheme 5.4. The intramolecular product cyclopentanone was detected as a product at less than 1%. They found that saturated aldehydes resulted in no product formation.

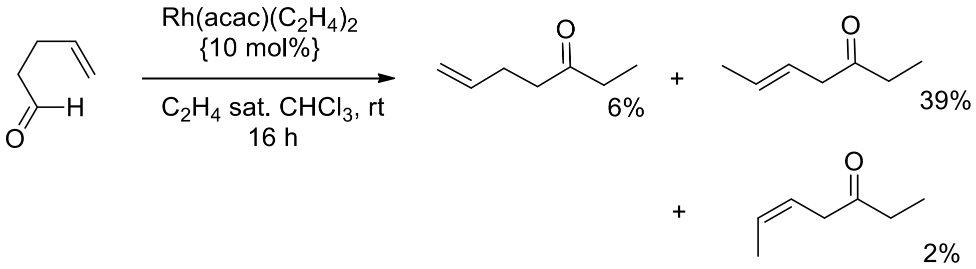

Scheme 5.4. Hydroacylation of 4-pentenal and ethene by Rh(acac)(C_2H_4)$_2$, an example of alkyne chelation.

After the initial findings by Miller, Vora showed that Z-4-heptanals under identical conditions could be combined with ethylene to form 6-nonen-3-one.[87] (Scheme 5.5)

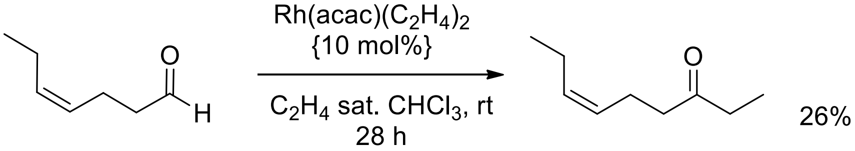

Scheme 5.5. Hydroacylation of Z-4-hentenal and ethene by Rh(acac)(C_2H_4)$_2$, an example of alkyne chelation.

Both of these results led to the conclusion that internal alkene coordination to the metal centre, essentially chelation of the aldehyde (Figure 5.2), was necessary for the reaction to occur.

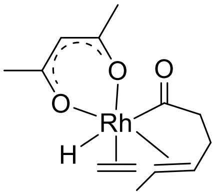

Figure 5.2. Possible structure of acyl-hydride intermediate with chelated enal.

Salicylaldehyde has also been employed as the aldehyde in conjunction with various alkenes and alkynes, using a catalyst produced from $[RhCl(COD)]_2$ and 1,1'-bis(diphenylphosphino)ferrocene (dppf). It was found that reactivity was high for vinyltriethylsilane and allenes, and minimal decarbonylation was observed.[88,89]

A similar system using salicylaldehyde as the aldehyde and 1,4- and 1,5-dienes has been established with good yields under mild conditions. 1,6-dienes were found to produce considerably lower yields. This system uses Wilkinson's catalyst in 20% catalyst loading at room temperature (Scheme 5.6). A drawback is that the branched isomer is preferentially formed over the linear isomer in a 4:1 ratio. They also showed that the reaction was possible in good yields with other 2-hydroxy aldehydes, but that the absence of the hydroxyl group did not produce the hydroacylation adduct.[90,91]

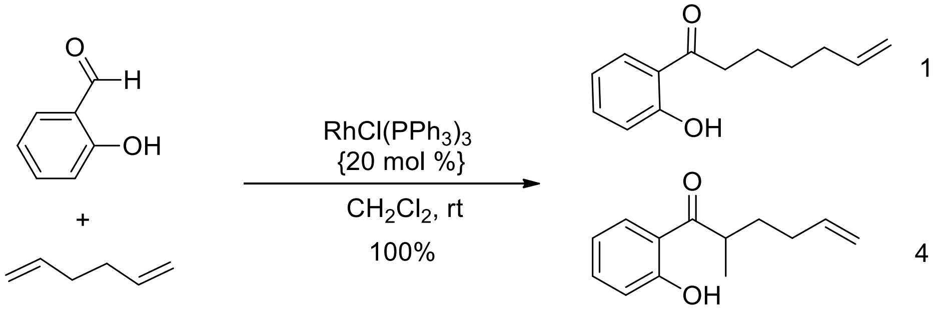

Scheme 5.6. Hydroacylation of salicylaldehyde and a 1,5-hexadiene by $Rh(Cl)(PPh_3)_3$, an example of aldehyde chelation.

The minimal decarbonylation with higher yields for 2-hydroxy aldehydes versus unsubstituted aldehydes was attributed to the proposed chelating intermediate that salicylaldehyde can form upon oxidative addition to the metal (Figure 5.3).

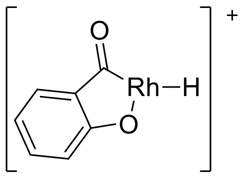

Figure 5.3. Chelating acyl-hydride intermediate resulting from salicylaldehyde, an example of O-chelation.

Similar to O-chelation is the method of S-chelation, where a sulfur-containing group on the aldehyde is used for the purpose of creating a chelating aldehyde. β–methylsulfide substituted propanal and β-thioacetal substituted aldehydes have been shown to produce good yields in conjunction with functionalized electron-poor alkenes using $[Rh(dppe)][ClO_4]^-$ at 50°C . This system also showed good results with terminal alkynes as they were selective for linear isomers with relatively good E-selectivity and internal alkynes could be employed but required longer reaction times.[92,93] Neither of these systems were functional for neutral alkenes such as 1-octene. A catalyst produced from $(Rh(COD)Cl)_2$ with bis[(2-diphenylphosphino)phenyl] ether (DPEphos) and $Ag(ClO_4)$ in acetone was found to be able to catalyze electron neutral alkenes such as 1-hexene with β-MeS-propanal, in 70% yield (Scheme 5.7). This system was also active for alkynes such as 1-hexyne.[94]

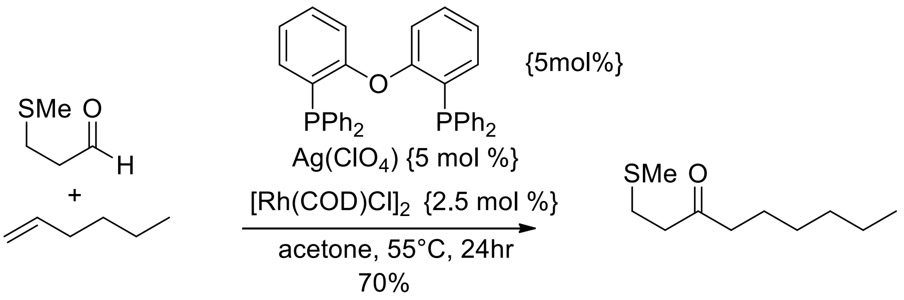

Scheme 5.7. Hydroacylation of methylthiopropanal and a 1-hexene, an example of aldehyde chelation S-chelation.

This rhodium DPEphos catalyst could also facilitate the reaction of enones with simple β-S-aldehydes, whereas the dppe derived rhodium catalyst under similar conditions in the past gave reductive aldol products instead. [95] This result was attributed to the flexibility and hemilability of the DPEphos ligand, which can adopt a variety of coordination modes and geometries, stabilizing the catalyst and resulting in a longer lived catalyst and increased activity (Figure 5.4).

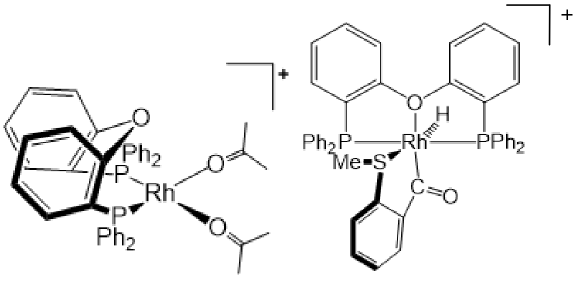

Figure 5.4. DPEphos ligand binding in different modes.

Stabilization of the acyl-rhodium intermediate can also be achieved by using a chelating alkene. N,N-dialkyl acrylamides as the alkene can be used with a range of alkyls and aryl aldehydes. The proposed intermediate has the bidentate alkene chelating to the metal (Figure 5.5).[96]

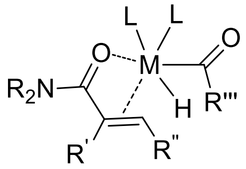

Figure 5.5. Chelating the alkene to the metal.

Catalyst design has also focussed on minimizing decarbonylation, and catalystshave improved since Wilkinson’s catalyst was first used. Rhodium with chelating bisphosphine ligands have shown promise as very active catalysts for alkyne hydroacylation (Figure 5.6). These were however, found to undergo decarbonylation when alkenes were utilized, with a trend toward smaller bite angle phosphine ligands, which were more active in catalysis.[28,29]

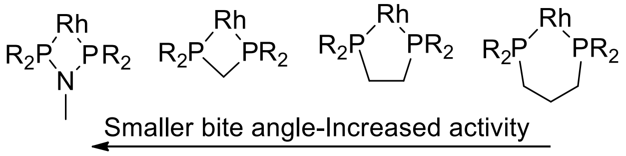

Figure 5.6. Rhodium with bisphosphine ligands of differing bite-angles.

Enantioselectivity of the hydroacylation reaction is currently being explored, with the use of different phosphine ligand systems leading to the formation of preferentially endo- or exo-isomers of the hydroacylation product (Scheme 5.8).

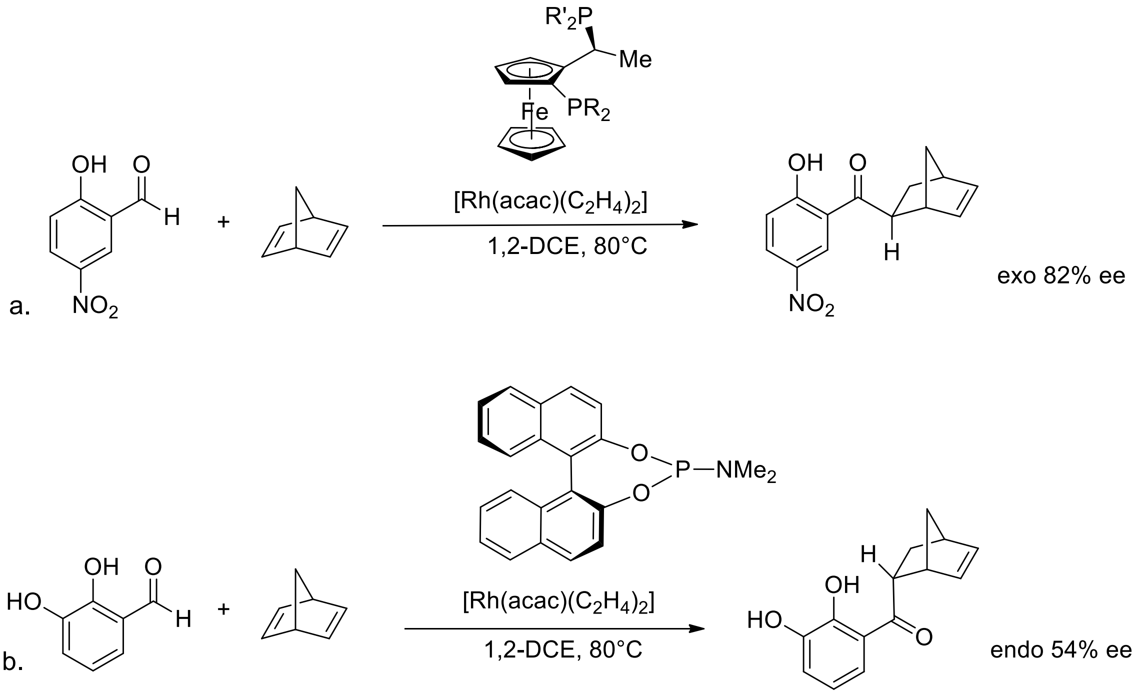

Scheme 5.8. a. Reaction scheme resulting in exo-selectivity, b.reaction scheme resulting in endo-selectivity.

Selectivity can be explained by the bidentate ligand causing the norbornadiene to bind in only one way, a monodentate manner, leading to the exo-selectivity. Endo-selectivtity could be achieved with the use of a monodentate phosphoramidate ligand.[97]

In a minority of cases, metals other than rhodium have been developed for catalysis. $RuH(CO)(PPh_3)_3$ is used as a catalyst for the addition of 1,3-dienes to aldehydes at relatively low catalyst loadings, 5 mol % at 90° C in toluene. A variety of dienes and aryl and alkyl aldehydes were found to produce branched β,γ-unsaturated ketones as products in good yields.[98] The proposed mechanism of this is different from that of rhodium catalyzed hydroacylation in that the initial step is the diene addition to the ruthenium hydride to form a π-allyl-ruthenium intermediate. The aldehyde can bind to this intermediate through a six-membered transition state, forming a ruthenium alkoxide, which can undergo β-hydride elimination forming the hydroacylation adduct and regenerating the ruthenium hydride.

Cobalt (I) bis-olefin complexes (Figure 5.7) have been shown to effectively catalyze addition of aromatic and alkyl aldehydes to vinyl trialkylsilanes, activity is shown for a broad range of aldehydes with vinyltrimethylsilane. The trimethylsilane substitution on the alkene is necessary as this allows for facile dissociation of the alkenes from the metal centre. While the conditions of the reaction are favourable, including room temperature, low catalyst loadings, and no requirement for a CO atmosphere; a drawback to this system is the requirement of vinyl silanes.[99]

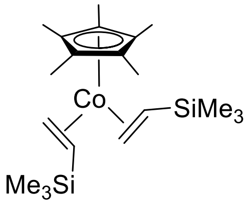

Figure 5.7.Cobalt hydroacylation catalyst developed by Brookhart.

Nickel (0) catalysts have shown effectiveness for alkyne but not for alkene hydroacylation. Ni(COD)$_2$ at 5 mol% could combine simple alkyl and aryl aldehydes with internal alkynes in good yields, to preferentially form the *E*-isomer of the enone product. The mechanism for this reaction is similar to rhodium catalyzed alkene hydroacylation and is also proposed to go through an acyl nickel hydride intermediate.[100]

5.2 Mechanistic Analysis of the Hydroacylation Reaction

The reaction studied in this work is that of a β-S-substituted aldehyde with an alkyne, the catalyst **5.A** is known to be selective to alkynes (Scheme 5.9). β-S-substitution of the aldehyde is necessary as this allows for chelation of the aldehyde to the metal which provides stability and protection from decarbonylation to the acyl-hydride intermediate. The reaction was initially studied in acetone, which is weakly coordinating and offers added stabilization to the reactive intermediate, but later it was determined that the reaction does not require a weakly coordinating solvent, and works well in 1,2-dichloroethane.

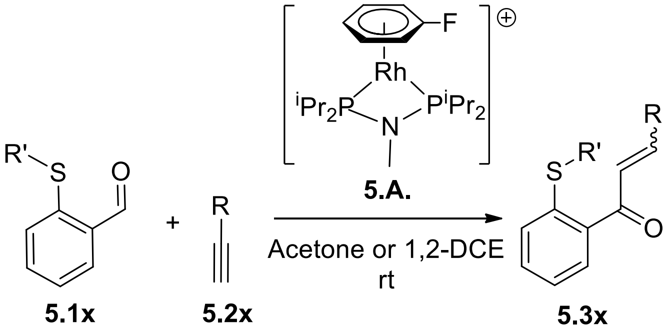

Scheme 5.9. Hydroacylation reaction scheme applying to charge tagged or neutral substrate catalyzed by [Rh(PNP^{i}pr)(FPh)]$^+$ [BAr$^F{}_4$]$^-$.

5.3 The Hydroacylation reaction studied by PSI ESI-MS with charged tags

5.3.1 Introduction

In order to study overall reactions we have employed the method of charge tagging, where a charged tag is attached onto a substrate in order to track it through reaction progress. In the design of the charged tags, efficiency in the ESI process was considered. In a polar solvent a greasy non-coordinating ion would have a higher efficiency than a small highly charged ion that is likely to strongly ion pair.[101] This is because only excess positive (or negative, depending on ionization mode) ions are observed in ESI-MS (ions that are paired do not make it into the mass selector). This phenomenon is called surface activity, as these large greasy ions are found to be at the surface of the droplets.[10] Charged tags with a high surface activity dominate the spectra and provide similar response factors for all the ions that incorporate that tag, thus a flat total ion current can be seen during a reaction involving this substrate and it is possible to relate intensities to concentrations. The charged tag should also have non-coordinating counter-ions to minimize ion pairing, which would results in a decrease in sensitivity and formation of aggregates.[71]

Phosphonium and ammonium charged tags were designed and used in the hydroacylation reaction (Scheme 5.9). We tested the use of a tagged aldehyde, as well as a tagged alkyne in conjunction with neutral counterpart substrates. The method was effective at studying the overall reaction of substrate use and product formation, and mono and di-cationic catalytic species were also observed.

5.3.2 Results and discussion

Three types of cationic charged tags were developed and tested, trimethylammonium **5.11**, tributylammonium **5.23**, and triphenylphosphonium **5.21** and **5.22** (Figure 5.8). These were paired with anions tetrafluoroborate ($[BF_4]^-$), hexafluorophosphate ($[PF_6]^-$), and tetrakis[3,5-bis(trifluoromethyl)phenyl]borate ($[BAr^F{}_4]^-$). The ideal charged tag should be easy to prepare in high purity, be inert in the reaction, and allow for a constant total ion current throughout the reaction, thus indicating similar ESI-MS response for all reactive species produced.

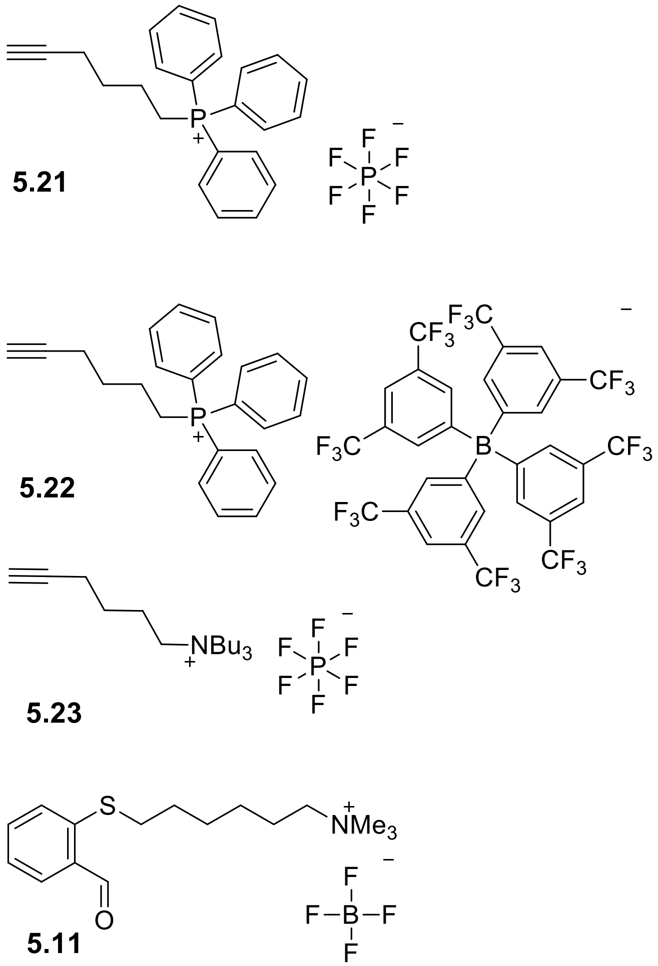

5.21

5.22

5.23

5.11

Figure 5.8**.** Charge tagged substrates employed.

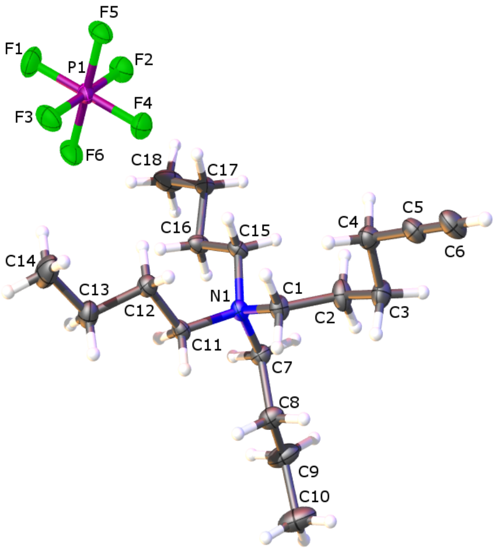

Figure 5.9. X-ray Chrystal structure of **5.23.**

The amenability of the charge tagged substrates shown in Figure 5.8 in the hydroacylation reaction catalyzed by **5.A.** (Scheme 5.9) was studied by PSI ESI-MS in positive ion mode. This was done by mixing a solution of the catalyst into a solution containing the charge tagged substrate (aldehyde or alkyne) and neutral partner substrate (alkyne or aldehyde) and monitoring the change in speciation by PSI ESI-MS that occurs during the mixing process and afterwards. If the charge tagged substrate is amenable to this reaction, the charged tag and the catalyst should be visible by MS, and both species should produce traces over time. In addition, the formation of product should be traceable throughout the reaction, and the total ion count should remain constant once all the tagged substrate is added.

The phosphonium tagged alkyne **5.21** was tested by addition of the alkyne to a reaction solution containing the catalyst **5.A** and the neutral aldehyde 2-(methylthio)benzaldehyde (**5.1**). Upon addition there was immediate disappearance of catalyst signal. Within 10 minutes there was no formation of product observed (Figure 5.10). This indicated that the charged tag was interfering with the reaction, be it the cationic tag on the substrate or the hexafluorophosphate anion paired with the charged tag.

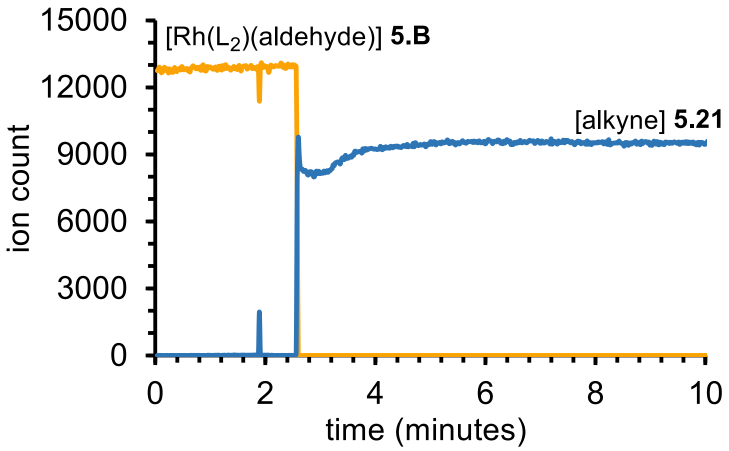

Figure 5.10. PSI ESI-MS reaction profile for the addition of **5.21** to a solution of catalyst **5.A** and aldehyde **5.1**. Conditions: 1.5 mM aldehyde, 2.3 mM alkyne, 0.15 mM catalyst, in acetone as solvent, 22°C.

It was hypothesized that the problem with the charge tag was the interaction of the $[PF_6]^-$ anion with the Rh catalyst. Hexafluorophosphate is considered a weakly-coordinating anion, but could react with a very electrophilic metal centre, rendering the "non-coordinating ion" non-inert.[102–104] To test this hypothesis, the same cationic tag was tested with a different anion, $[BAr^F_4]^-$. $[BAr^F_4]^-$ is much less prone to fluoride abstraction, and less coordinating than either $[PF_6]^-$ or $[BF_4]^-$,[105] also, it is shown to be unreactive with this catalyst, as it is the anion pair to the rhodium cation. Consequently a $[BAr^F_4]^-$ anion pairing along with the same phosphonium cation (**5.22**) was attempted under conditions of sub-stoichiometric amounts of alkyne to catalyst. A solution of the alkyne **5.22** was added to a solution of catalyst **5.A** and aldehyde **5.1** such that catalyst to charged alkyne would be a ratio of 3 to 2. Figure 5.11 shows that upon addition of the charge tagged alkyne to the catalyst solution, the catalyst signal dropped substantially, and was replaced by the charged tag, but no product was seen to form.

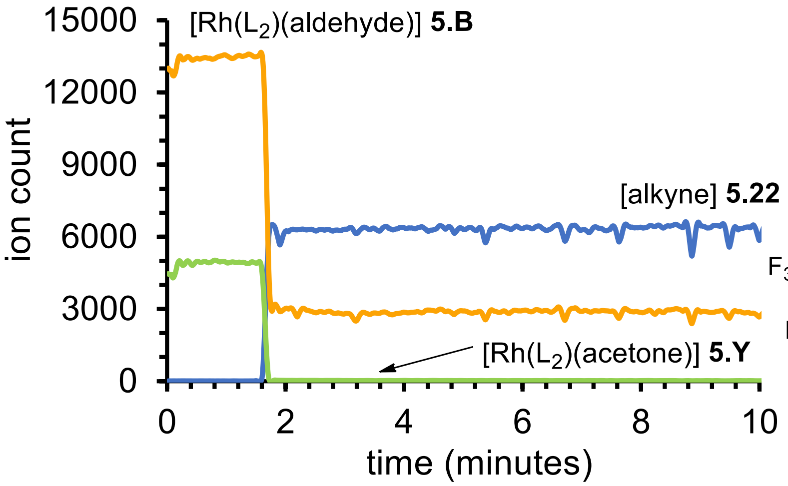

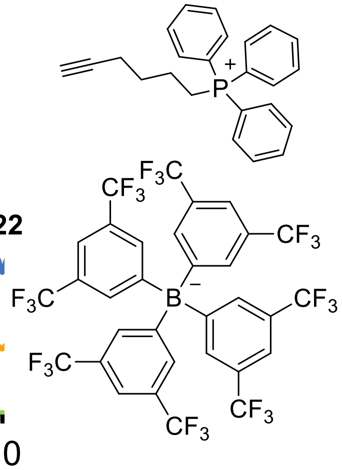

5.22

Figure 5.11 PSI ESI-MS reaction profile for the addition of **5.22** to a solution of catalyst **5.A** and aldehyde **5.1**. Conditions: 1.5 mM aldehyde **5.1**, 0.2 mM alkyne **5.22**, 0.3 mM catalyst **5.A**, in acetone as solvent, 22°C no product was produced.

This test determined that the cation must be the culprit in the disappearance of catalyst signal, thus we moved on to exploring different cations. Ammonium cations were tested next. Trimethylammonium tagged aldehyde **5.11** showed good results in that no catalyst poisoning was observed, but to optimize the electrospray process a greasier version of an ammonium tag was designed. The tributylammonium tag was used as it should be over represented during the ESI process and should have a sufficiently good response that the total ion count should remain relatively constant in either reactant, catalyst-bound, or product form. Tributylammonium tagged hexyne **5.23** was seen to be effective for hydroacylation and the catalyst signal did not disappear upon introduction of the charge tagged substrate.

5.3.2.1 A charged aldehyde and neutral alkyne for reaction monitoring:

A charged aldehyde **5.11** and 1-octyne (**5.2**) were reacted in the presence of catalyst **5.A** (Scheme 5.10).

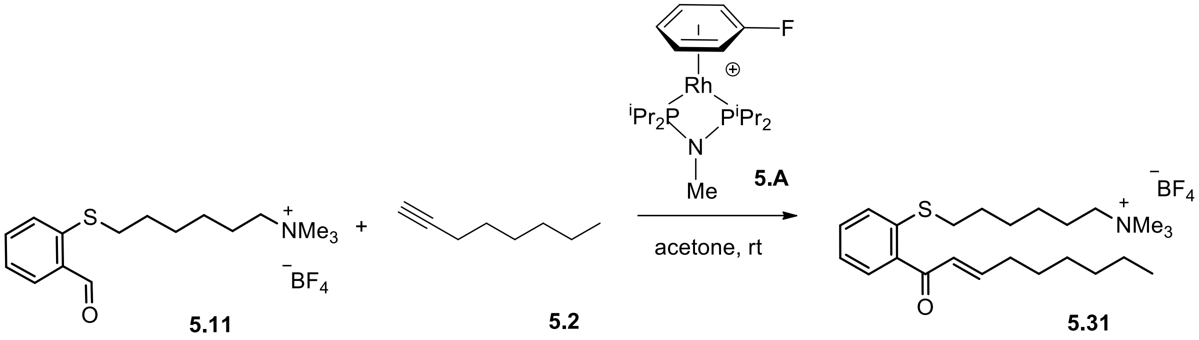

Scheme 5.10 Hydroacylation of charge tagged aldehyde and 1-octyne catalyzed by $[Rh(PNP^ipr)(FPh)]^+$ $[BAr^F{}_4]^-$.

Monitoring this reaction by PSI ESI-MS resulted in the reaction profile shown in Figure 5.12, showing the decrease in aldehyde **5.11** signal (blue) after the addition of the catalyst, producing the ketone **5.31** product (purple). The catalyst is observed upon addition with one (**5.Y**) or two (**5.Z**) acetones coordinated (light and dark green), and these decrease over time and are replaced by a dication of *m/z* 378.2 (pink). The mass and charge is consistent with the product bound to the catalyst **5.D1**.

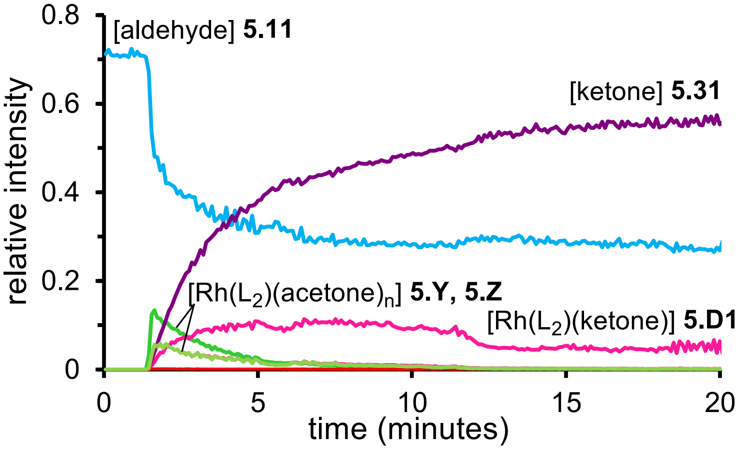

Figure 5.12. PSI ESI-MS trace for reaction conditions: 1.5 mM aldehyde **5.11**, 2.3 mM alkyne (1-octyne), 0.15 mM catalyst, in acetone as solvent, 22°C.

Examining all the traces that were produced throughout the reaction yielded important information. Firstly, the starting aldehyde turns into product in what appears to be a first order reaction, with a fast rate at the beginning of reaction, slowing down over time. Secondly, not all the starting material was used up in the reaction, at the end of reaction the signal for the aldehyde had only decreased to about half of what it was at the start of reaction. The ketone product signal had increased by more than the aldehyde signal had decreased. This suggests that the product ketone has a higher surface activity in the ESI process than the aldehyde, which is expected as the ketone product is greasier by an 8-carbon chain than the aldehyde starting material.

Next, we can examine the traces that contain the rhodium catalyst, the first instances of catalyst that are observed appear seconds after a solution of catalyst **5.A** in acetone had been added to the reaction. The version of the catalyst that we observe has acetone bound instead of FPh as in catalyst **5.A**, we see two version of this, *m/z* 424.1 (calc: 424.1) a 14-electron species where one acetone is coordinated, and *m/*z 482.2 (calc: 482.2) a 16-electron species where two acetones are coordinated (Figure 5.13) . Under a small increase in collision voltage in the collision cell the species at *m/z* 424.1 dissociates to *m/z* 366.1 which is $[Rh(L_2)]^+$ (calc: *m/*z 366.1), and the species at *m/z* 482.2 dissociates to *m/z* 424.1 and *m/z* 366.1. This evidence suggesting a weakly bound ligand of mass 58.1 Da, consistent with the acetone adduct. Acetone is a weakly coordinating solvent, and as it is in such greater abundance than FPh, it is not surprising that the rhodium complex is speciated in this manner.

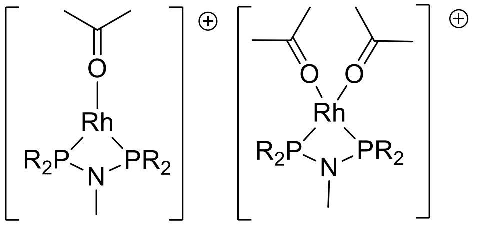

5.Y **5.Z**

Figure 5.13. Proposed structure of catalyst acetone adducts **5.Y** and **5.Z.**

The acetone adducts **5.Y** and **5.Z** decrease in abundance, and in their place grows in a peak at *m/z* 378.2, which has an isotope pattern with peaks separated by *m/z* 0.5 indicative of a dication. CID of *m/z* 378.2 (Figure 5.14) shows the dissociation of the dication into two monocations of *m/z* 366.3, characteristic of $[Rh(L_2)]^+$, and *m/z* 390.4 which is characteristic of ketone product **5.31**.

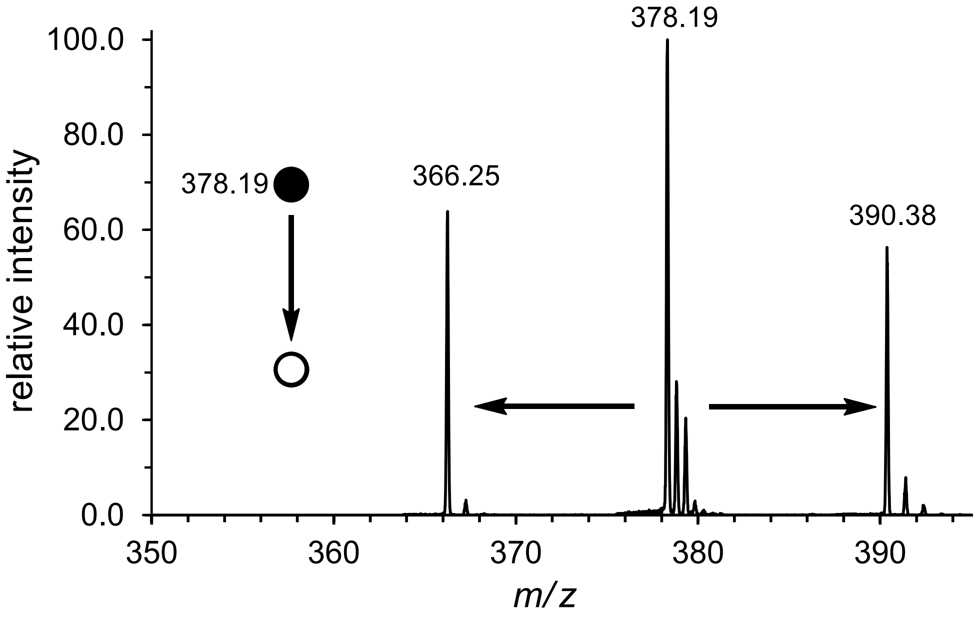

Figure 5.14. MS/MS CID dissociation of the dication *m/z* 378.2. **5.D1**.

The isotope pattern was also found to match the predicted isotope pattern of **5.D1.** as seen in Figure 5.15.

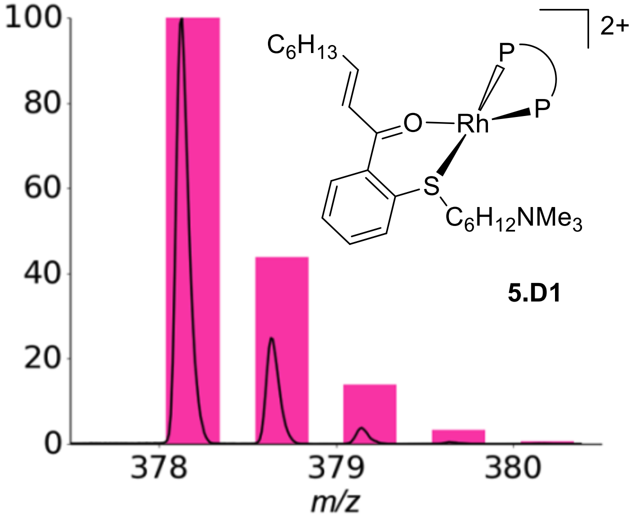

Figure 5.15**.** Experimental isotope pattern (black line) and predicted isotope pattern (pink bars) with proposed structure for **5.D1**.

The signal of **5.D1** stays relatively stable throughout the remainder of the reaction, but does seem to decrease near the end, indicating the resting state of the reaction, being that the product ketone is the species binding most strongly to the catalyst that is in the reaction. This also suggests that possible product inhibition is happening by the product as catalyst is trapped in the product bound version and might be less reactive than acetone adducts of the catalyst.

Looking into the baseline of this reaction, peaks were observed that had the mass of the intermediate acyl-hydride formed upon oxidative addition of the aldehyde to the rhodium centre (Figure 5.16). The trace due to the dicationic species with *m/z* 323.0 is found to exhibit behaviour characteristic of an intermediate, with an initial increase in signal upon addition of the catalyst, then a decrease in signal as the reaction progresses.

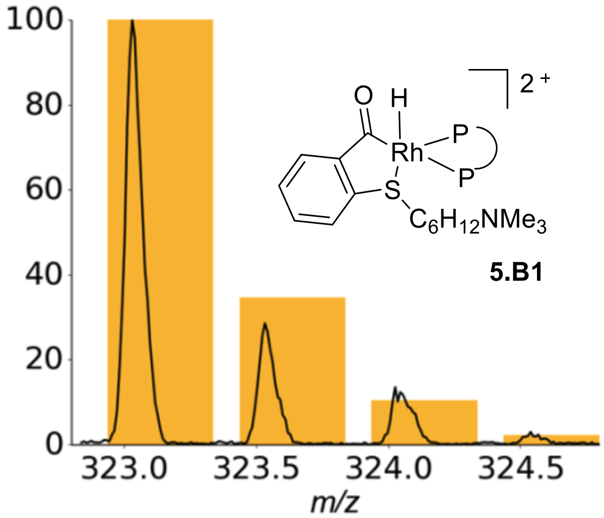

Figure 5.16. Experimental isotope pattern (black line) and predicted isotope pattern (orange bars) with proposed structure for **5.B1**.

5.3.2.2 Using a neutral aldehyde and charged alkyne for reaction monitoring:

The ammonium charge tagged alkyne **5.23** was reacted with 2-(methyl)thiobenzaldehyde **5.1** catalyzed by **5.A** to compare the reaction profile that would result to that of the reaction of a charged aldehyde and neutral alkyne (Scheme 5.11Scheme 2.1). It was expected that if the charged tag does not interfere in the reaction, the two profiles should be similar in that we should expect to see free alkyne at the beginning of the reaction, upon addition of the catalyst there should be coordination of the alkyne and aldehyde to the catalyst to present the resting state of the catalyst as the product bound version of the catalyst, which over time will yield free product. Sole coordination of the alkyne to the catalyst $[Rh(L_2)(NBu_3C_6H_9)]^{2+}$ was not expected to be seen in any great intensity due to the weakness of η^2-alkyne-Rh coordination, which would likely result in dissociation of alkyne during the ESI process and hence appear as $[Rh(L_2)]^+$.[71]

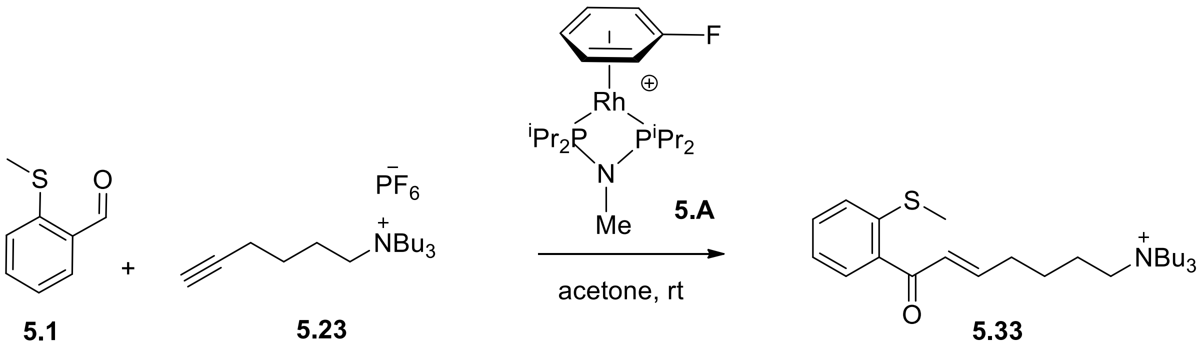

Scheme 5.11**.** Hydroacylation of charge tagged alkyne and 2-(methyl)thiobenzaldehyde **5.1** catalyzed by $[Rh(PNP^ipr)(FPh)]^+$ $[BAr^F{}_4]^-$.

Utilizing an ammonium-tagged-alkyne (**5.23**) we expected to see alkyne abundance decrease with formation of ketone product (Figure 5.17). Note the reaction contains a ratio of 1.5:1 alkyne to aldehyde, and therefore only 2/3 of the alkyne would be expected to be depleted by the end of the reaction.

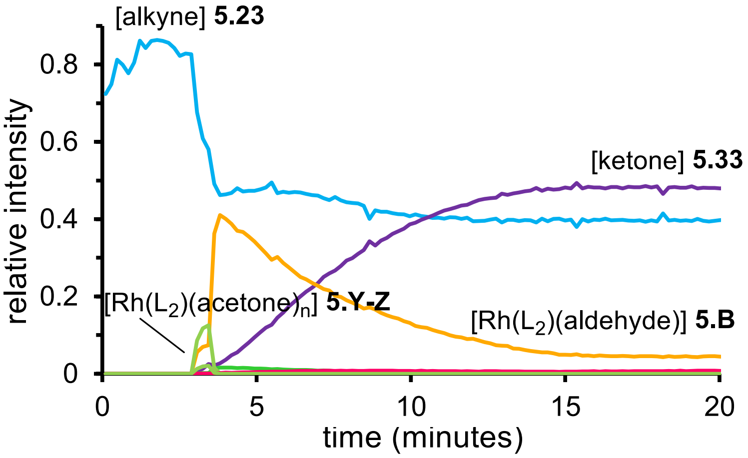

Figure 5.17**.** PSI ESI-MS Reaction profile, conditions: 1.5 mM aldehyde, 2.3 mM alkyne, 0.15 mM catalyst, in acetone as solvent, 22°C.

What we observe is the charged alkyne substrate present at the beginning of the reaction, which plummets to the baseline when the catalyst is injected, yet the alkyne does not get replaced by a signal that contains the charged alkyne. This indicates that the alkyne has actually not decreased in concentration, rather the signal due to the alkyne has decreased due to being outcompeted in the electrospray process by the catalyst. The catalyst form that is observed is the aldehyde bound to the catalyst, namely the acyl-hydride intermediate **5.B**. After this initial decrease in signal of alkyne, the alkyne signal does not appear to change much over the rest of the reaction, with only a slight decrease in its intensity, yet product forms, which is proof that alkyne must have been consumed. These apparent inconsistencies are most likely a result of oversaturation of the detector by the starting alkyne where the concentration of the alkyne is outside of the linear range of the detector. Therefore when the actual concentration of the alkyne is decreasing, the decrease in signal is not initially observed. $[PF_6]^-$ aggregates of **5.23** were also observed, indicating a concentration issue. Another feature that is most likely due to oversaturation of alkyne signal is that the catalyst signals are disproportionally large compared to the substrate signals. A 10% catalyst loading to aldehyde was used, which would be a 6.7% loading to the alkyne, thus if the catalyst and substrates yielded signals proportional to their concentrations, catalyst should be only 6.7% of the signal due to the substrate at any time.

Looking more closely at this data, the initial catalyst solvent adducts (Figure 5.17, green), quickly forms the acyl-hydride intermediate **5.B** (expected as an intermediate) that decreases over time. Its *m/z* and isotope pattern confirmed its identity (Figure 5.18). Over the duration of the reaction the ketone product is formed but we do not observe the product bound version of the catalyst as we had seen in the charged-tagged aldehyde version of this reaction.

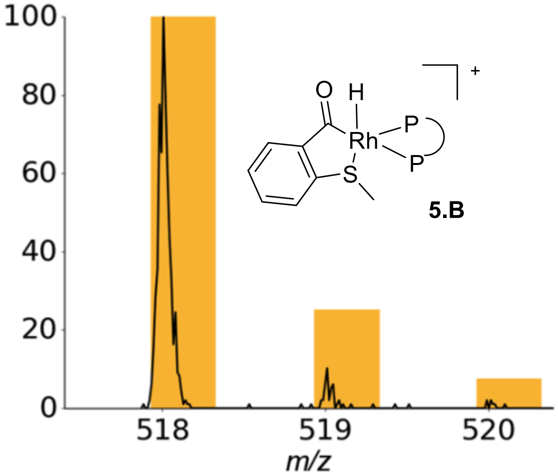

Figure 5.18. Experimental isotope pattern (black line) and predicted isotope pattern (orange bars) with proposed structure for **5.B**.

We observe the acyl-hydride intermediate for longer in the reaction of the tagged alkyne **5.23** than we do when employing the tagged aldehyde **5.11**, suggesting that the alkyne coordination step is slower in comparison when using **5.23** rather than 1-octene. This result is possibly due to the steric hindrance on coordination or because of electrostatic repulsion as both metal centre and alkyne would be positively charged. A possible improvement in the design on the charge tagged alkyne would be greater separation between the charged tag and the alkyne group, and more structural rigidity in that linkage in order to keep the ammonium further away from the metal centre to cause less interference with alkyne coordination. The product bound version of the catalyst was not observed, possibly due to the charged tag promoting dissociation from the metal in a greater amount than when utilizing the charged aldehyde **5.11** and neutral 1-octyne.

5.3.3 Conclusions of charge tagging

We observe the acyl-hydride intermediate which supports that the aldehyde adds to the metal before the alkyne inserts. The charged tag substrates utilized gave differing results for the dynamics of reactant species between substrates. These results point to the importance of considering the interference of the charged tag within the reaction when deciding upon a charged tag. Different charged tags were found to affect the relative speed of different steps within the reaction. During these tagging studies, concentrations of charged substrates that were extremely high for traditional mass spectrometry were employed (i.e. 1.5 mM aldehyde). These high concentrations affected the quality of our data, incurring saturation of the detector, clogging of the ESI capillary, and commonly resulted in cross contamination between reactions. Concentration problems are inherent in these type of systems, as substrates in catalytic reactions are generally at much higher concentrations than the catalyst, and attempting to monitor both the catalyst and the substrates with the mass spectrometer is not ideal. When conditions are optimized for the monitoring of the catalytic species, the substrates saturates, and when optimized for the substrate, the catalyst is in such low concentration that systematic catalyst poisoning, and detection of the catalyst becomes issues. These problems encountered led the development of a system that would employ two methods of detection to study the two parts of a catalytic reaction, the low concentration catalytic species would be studied by PSI ESI-MS, while the higher concentration substrates and products could be studied by FT-IR spectroscopy.

5.4 IR-MS

Infrared spectroscopy in conjunction with PSI-ESI-MS was used in order to track the changes in concentration of neutral reaction substrates, products, and charged catalytic species simultaneously. A benefit of this setup was that we used systems of detection that are each sensitive at the concentrations that a reaction would be run at, the substrate and products are being monitored with a method that is optimal at millimolar to molar concentrations, while the catalyst is being monitored by MS which is great at monitoring at milimolar to micromolar concentrations. The two techniques together opens up our dynamic range across which we can observe the reactions unfolding. In using this method that we developed, both the IR and the MS are monitoring the same reaction solution, removing the error that would be present between experiments if two different experiments had to be set up. Using these tandem methods we can map what the catalyst is doing throughout the progress of the reaction.

5.4.1 IR-MS Method development

A Bruker ALPHA FT-IR with a flow cell was used along with a KNF Simdos 02 dosage pump for circulation of the reaction solution, both of which are shown in Figure 5.19. The Simdos is a new version of the Stepdos by KNF, which is a dosing pump that is designed for delivering corrosive and chemically reactive liquids at a specified dosage rate.[106]

Figure 5.19. a. Bruker Alpha FT-IR and a Harrick transmission flow cell. b. KNF Lab Simdos 02 pump.

Simultaneous monitoring of a reaction solution by both methods was achieved by running solution in parallel from the same reaction flask to both instruments as is shown in Figure 5.20. This method uses the PSI ESI-MS method along with a circulating loop to the FT-IR. The rate of circulation through the loop to the transmission cell and back into the flask was determined to be optimal at 2.5 ml/minute, allowing for a minimal time lag between reaction progress and sampling time instances. The tubing used had an inner diameter of 200 μm, narrow enough to allow for small volumes being taken up in the tubing while wide enough not to create appreciable back pressure in the circulation pump. A 100 μm path-length was used in the transmission cell because this allowed for a strong signal, while also letting the flow cell have a minimal volume. The total volume loop made up of the flow-cell, tubing, and pump-head was determined to be 700 μL. Thus at a circulation rate of 2.5 ml/minute, the loop would be cleared every 17 seconds, so a scanning rate of a set of IR scans every 20 seconds was decided on.

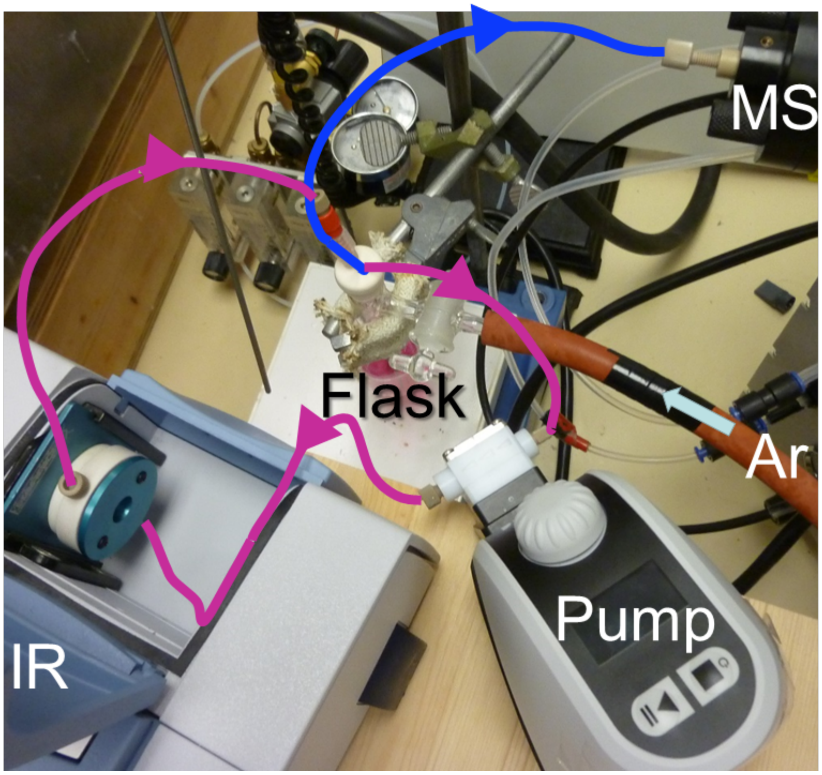

Figure 5.20**.** Reaction monitoring setup with reaction solution continually fed to ESI-MS by an overpressure applied by an argon cylinder (blue arrow), and circulation of the reaction solution through the flow cell of the FT-IR by the pump (pink arrows).

A neutral substrate version of the hydroacylation reaction shown in Scheme 5.9 was studied with this method of IR-MS. Charged tags were not used as the overall reaction of the neutral substrates could be tracked by monitoring the IR absorption due to the carbonyl stretch.

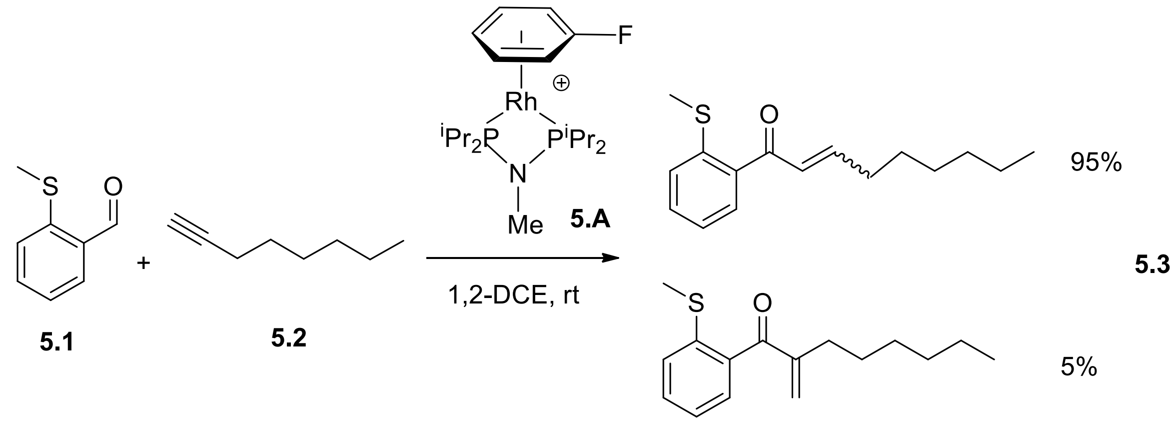

Scheme 5.12. Hydroacylation reaction with neutral substrates for monitoring by IR-PSI ESI-MS.

1,2-Dichloroethane (DCE) was used as solvent instead of acetone to avoid the strong IR absorption in the ketone region due to the carbonyl stretch in acetone. The catalyst has proven to be just as effective in non-coordinating solvents such as dichloromethane and DCE as in weakly coordinating solvents such as acetone when catalyzing the reaction shown in Scheme 5.12. [28] DCE was chosen as solvent for its high boiling point, which would allow for heating of the reaction, and its IR absorption properties which leaves a relatively open window between 2900-1500 cm^{-1}.

The aldehyde showed strong carbonyl stretches at 1695 cm^{-1} and 1680 cm^{-1} and absorptions at 1589 and 1560 cm^{-1} due to aromatic stretches (Figure 5.21).

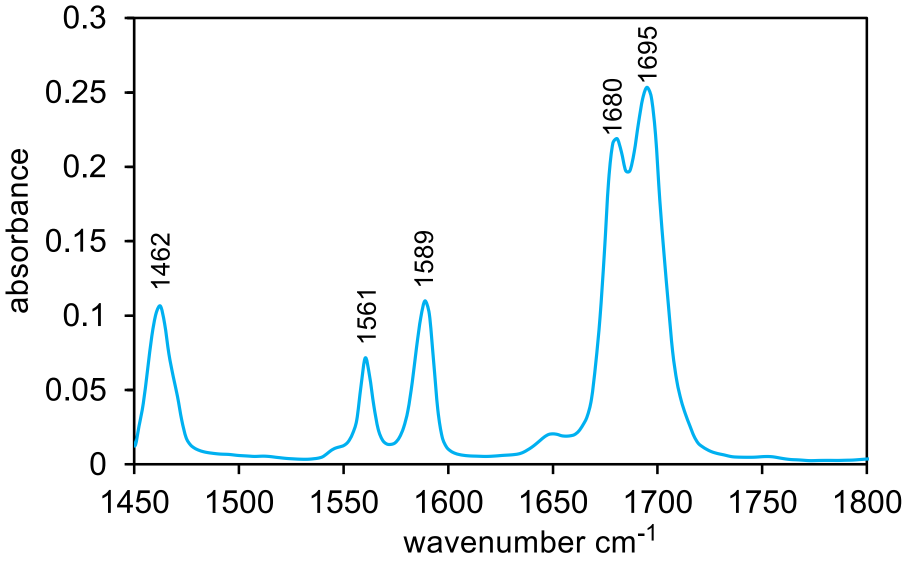

Figure 5.21. IR absorbance spectrum of 2-(methylthio)benzaldehyde (**5.1**) and 1-octyne mixture in DCE (16 s data collection for 16 co-additions).

The product formed at the end of the reaction had a very different IR spectrum (Figure 5.22). The alpha-beta unsaturated ketone has a carbonyl stretch at 1650 cm^{-1}, which is lower than an aliphatic ketone carbonyl due to the conjugation in the molecule. The alkene part of that molecule has a C=C stretch at 1615 cm^{-1} which is a strong absorption, consistent with literature as the absorption frequency of an alkene conjugated with a carbonyl group is generally found at lower frequencies and the intensity of the absorption can be strong; the C=C stretches can be as strong as a carbonyl stretch.[26]

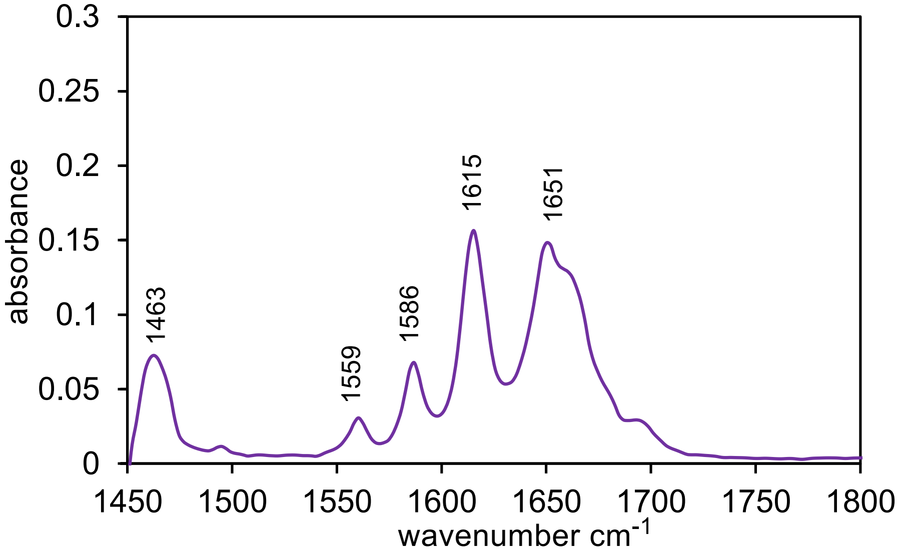

Figure 5.22. IR absorbance spectrum of 1-(2-(methylthio)phenyl)non-2-en-1-one and 1-octyne after reaction in DCE (16 s data collection for 16 co-additions).

The strong carbonyl stretches were determined to be good candidates for tracking of reaction progress, and a calibration curve (Figure 5.23) showed the area of the carbonyl stretch of 2-(methythio)benzaldehyde to be proportional to concentration of that species over a concentration range that would be amenable to the reaction.

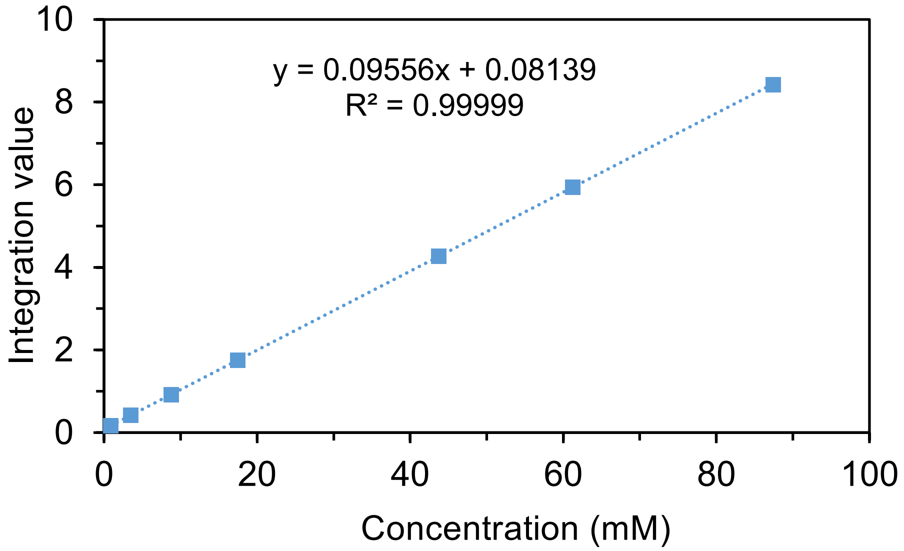

Figure 5.23.Calibration curve for 2-(methylthio)benzaldehyde showing the linear relationship between concentration and integration of the carbonyl stretch 1620-1740cm^{-1} up to 90mM concentration (16 s data collection for 16 co-additions).

5.4.2 Results and discussion for IR-MS studies

The change in the absorbance intensities of the carbonyl stretches was monitored throughout a reaction to produce Figure 5.24, where the aldehyde stretch decreases in intensity while the ketone and alkene stretches increase in intensity, there are well defined isosbestic points indicating the clean conversion of one species into the other.

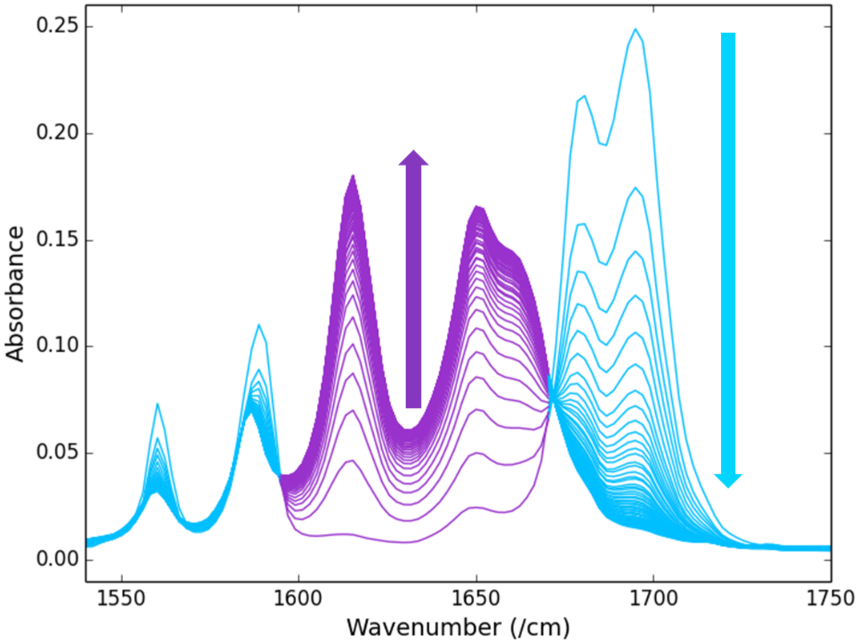

Figure 5.24**.** Overlaid absorbance spectra over time of a reaction, conditions: 75 mM aldehyde **5.1**, 1.13 mM alkyne **5.2**, 3.75 mM catalyst **5.A.** (5% loading) in DCE as solvent, rt. Blue indicated absorbance due to aldehyde **5.1**, purple absorbance due to product **5.3**. (16 s data collection for 16 co-additions, 4 s resting period)

Reaction profiles were created from these spectra to show substrate depletion and product formation. A plot of the average of 10 reactions with one standard deviation error for each data point is shown in Figure 5.25.

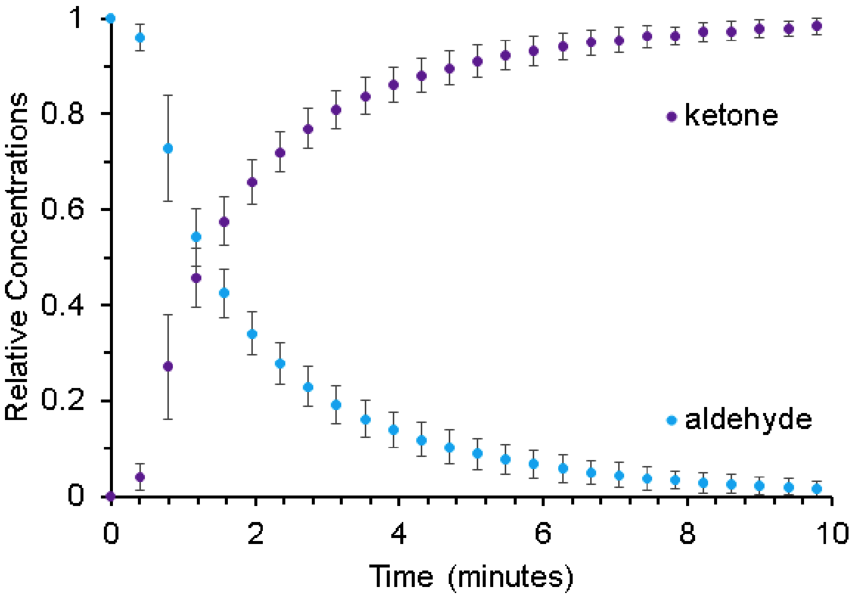

Figure 5.25. IR reaction profile, conditions: 75 mM aldehyde **5.1**, 1.13 mM alkyne **5.2**, 3.75 mM catalyst **5.A.** (5% loading) in 12-DCE as solvent, rt. Blue indicated substrates, purple indicates product. Error bars are ± one standard deviation of each data point for 10 trials.

The error in each data point corresponds to the point during the reaction that it is measured, the error is larger at the beginning of the reaction; by about 10 minutes the error is much smaller, indicating that by 10 minutes the reaction is reliably over. The reaction follows first order to aldehyde concentration dynamics as is shown in Figure 5.26 where the natural log of the relative concentration of aldehyde is plotted against time to yield a linear relationship for the reaction with a 5% catalyst loading.

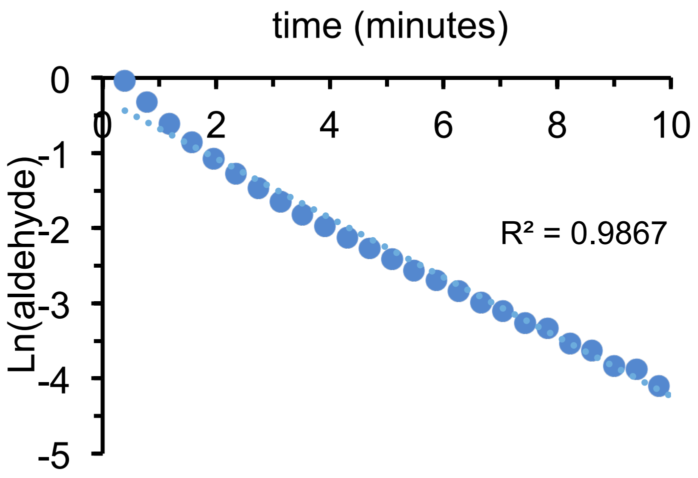

Figure 5.26. Plot of natural log of the signal intensity due to aldehyde against time shows a linear relationship.

The effect of catalyst concentration on rate of reaction was tested, with catalyst loading of 1, 3, 4, and 5%, corresponding to concentrations between 0.75 to 3.75 mM. The reaction rate constants were found to be reliably lower for lower catalyst concentrations, and a near linear relationship that deviates from linearity more at lower concentration is reported in Figure 5.27.

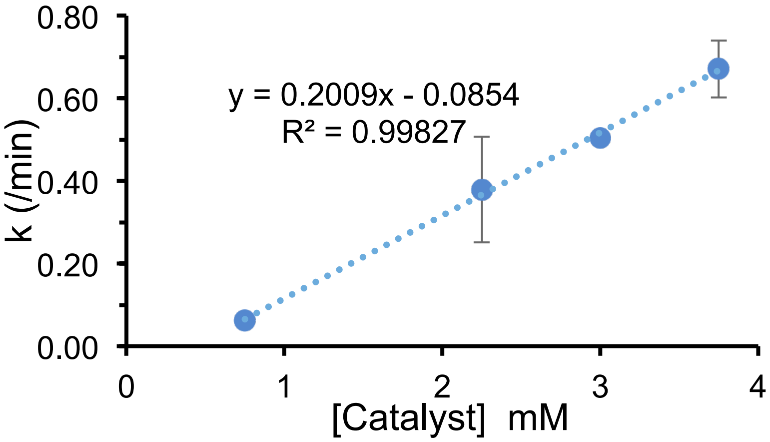

Figure 5.27. Catalyst concentration effect on rate constant for reaction 1-5% catalyst loadings, .

The relationship does not appear to pass through the origin, instead it appears as if a zero rate constant would be found at about 0.4 mM catalyst concentration. This effect is most likely due to degradation of the catalyst by reaction with some small fixed amount of a poison in the reaction matrix. If the degradation causing reactant is at a constant amount in all these reactions, then a larger percentage of catalyst degradation would be expected at the lower catalyst loadings. This greater catalyst decomposition at low catalyst loadings is also consistent with MS results. By MS the total ion count decreases significantly over time of reaction with low catalyst loadings such as 1%. This phenomenanon is not observed to such an extent at higher catalyst loadings such as 5%. Figure 5.28 shows the total ion count and a the trace of an internal standard by MS for a catalytic reaction at 1% catalyst loading over 10 minutes.

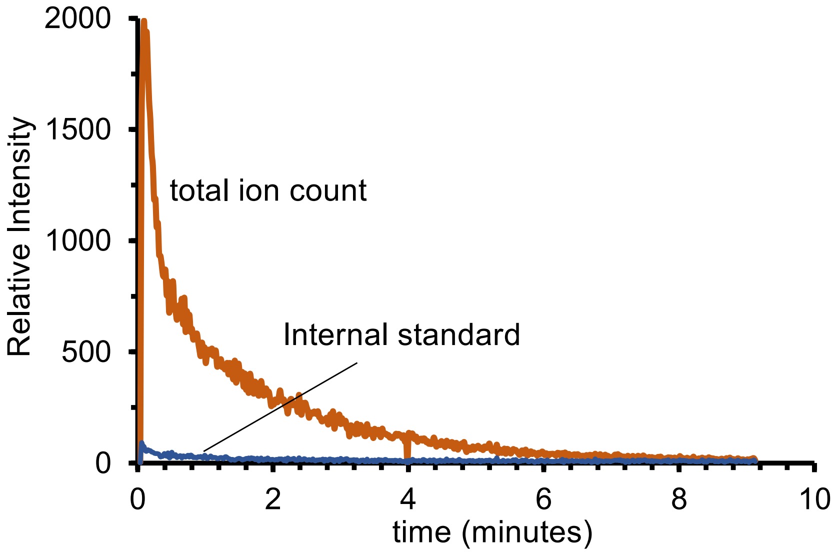

Figure 5.28**.** MS total ion count (brown) and internal standard (navy) intensities over time of a reaction. Conditions: 75 mM aldehyde **5.1**, 1.13 mM alkyne **5.2**, 0.75 mM catalyst **5.A.** (1% loading) in DCE as solvent, rt.

The effect of alkyne loading on rate of reaction was tested, with alkyne concentrations between 0.08 and0.75 M which corresponded to of 1 to 10× alkyne loading to aldehyde. The reaction rate constants were found to increase slightly with increasing amount of alkyne concentration (Figure 5.29).

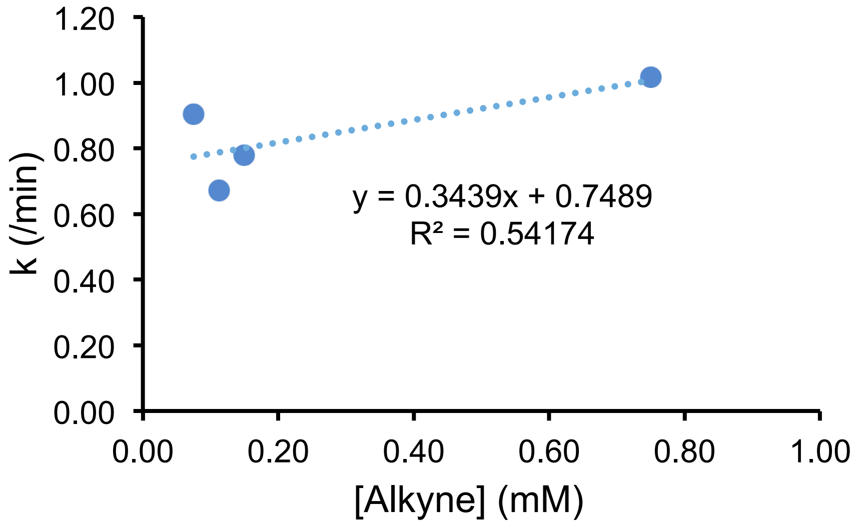

Figure 5.29. Alkyne loading effect on rate constant for reaction 1-10x alkyne equivalents.

The possible increase in rate constant with higher alkyne equivalents could be an effect of a more disfavoured decarbonylation pathway with increasing alkyne concentration. With higher concentrations of alkyne, the coordination of the alkyne to the acyl-hydride intermediate is sped up, minimizing the time the time the catalyst spends as that reactive intermediate which is prone to decarbonylation. The alkyne stabilized intermediate can then undergo migration to form product instead of undergoing decarbonylation. This minimization of decarbonylations allows for more of the active catalyst to be present, thus a slight increase in the rate constants can be observed.

The effect of temperature on rate of reaction was tested, the reaction was performed at temperatures from 0 to 42°C (Figure 5.30). The reaction rate constants were found to increase with increasing temperature.

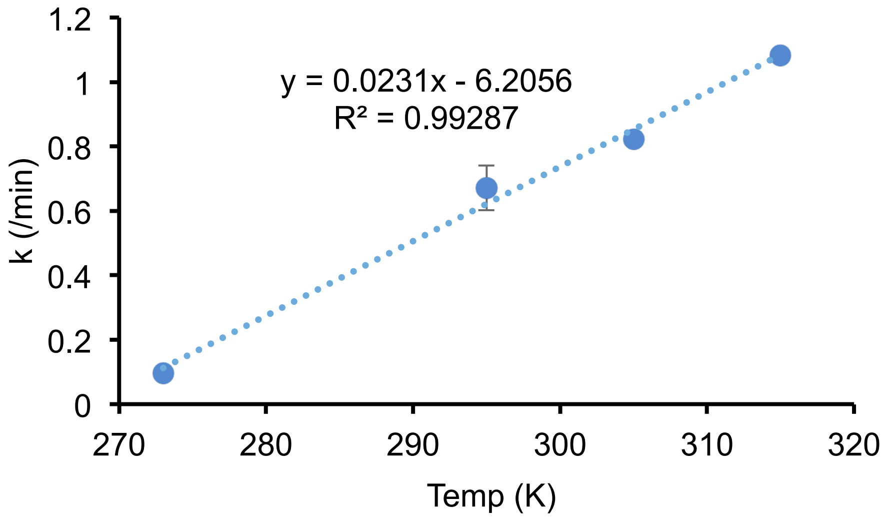

Figure 5.30.Temperature effect on rate constant for reaction, 273 to315 K.

In summary of all the reaction conditions, observing just the starting material use and product formation we came up with Table 5.1 of reactions from which we conclude that the reactions are first order to aldehyde, small positive order to alkyne, dependent of catalyst, and for higher reaction temperatures, and the reaction goes faster.

Experiment	Temp °C	[Cat] M	% Cat loading	[ald] M	[alkyne] M	k (/min)	rate (M/min)
standard	22	0.0038	5	0.075	0.11	0.67	0.050
temperature	0	0.0038	5	0.075	0.11	0.10	0.007
temperature	32	0.0038	5	0.075	0.11	0.82	0.062
temperature	42	0.0038	5	0.075	0.11	1.1	0.081
cat loading	22	0.0030	4	0.075	0.11	0.50	0.038
cat loading	22	0.0023	3	0.075	0.11	0.38	0.028
cat loading	22	0.0008	1	0.075	0.11	0.06	0.005
1[alkyne]	22	0.0038	5	0.075	0.08	0.90	0.068
10[Alkyne]	22	0.0038	5	0.075	0.75	1.0	0.076
2[alkyne]	22	0.0038	5	0.075	0.15	0.78	0.058
1/2[ald],1/2[cat],1/2[Alk]	22	0.0019	5	0.038	0.06	0.34	0.013
1/2[ald]	22	0.0038	10	0.038	0.11	0.95	0.036

Table 5.1. Reaction conditions and reaction rate constants.

ESI-MS was used to simultaneously monitor the reaction over time in positive ion mode as the IR data was collected to produce abundance traces for all species detected. These traces produced varied over an abundance range of roughly 5 orders of magnitude. These traces can be categorized according to abundance, and role of species in the reaction seen in Figure 5.31. The catalyst was added at time 0 minutes.

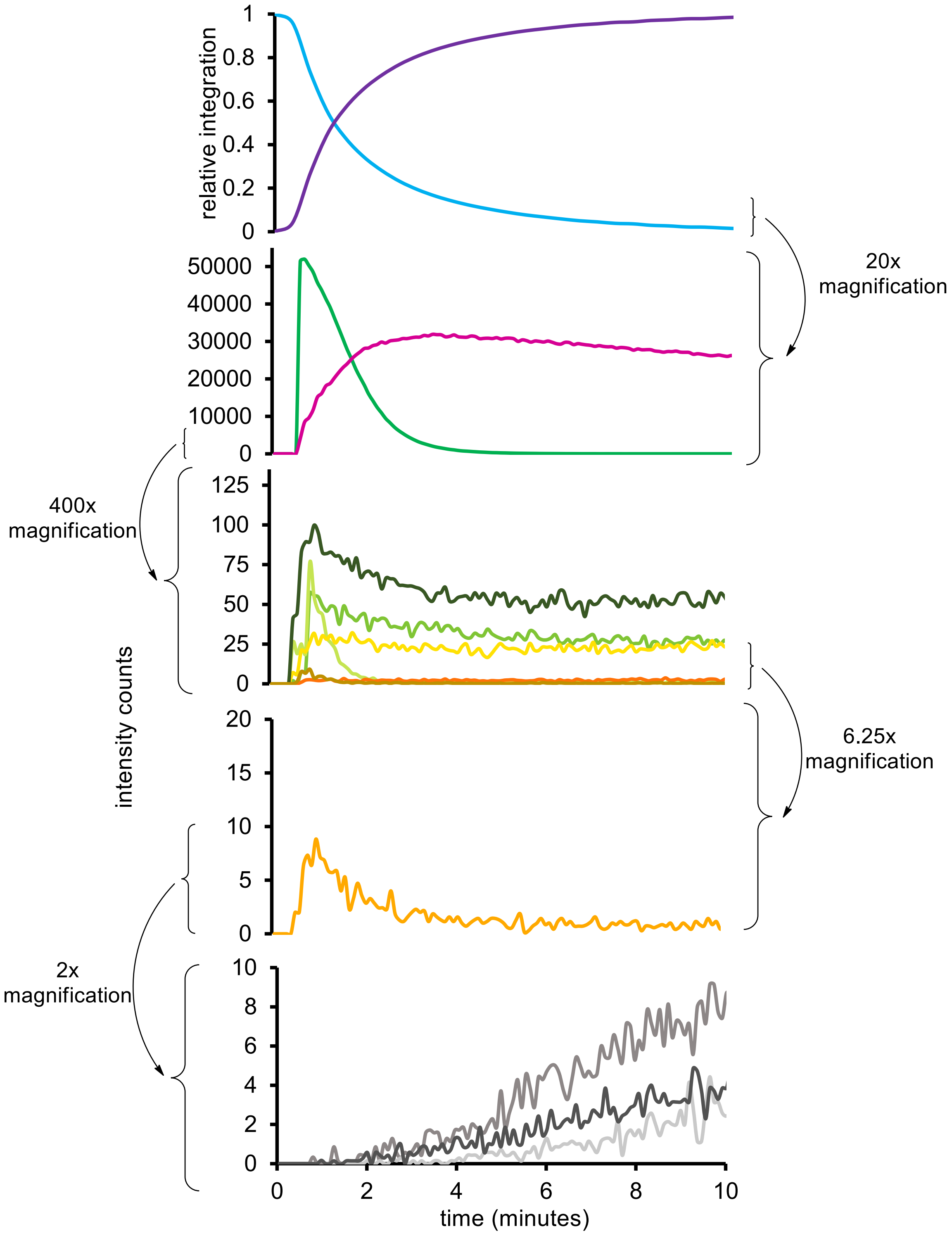

Figure 5.31. Reaction traces for all species in reaction solution.

There is a 30 second delay between the addition of the catalyst to solution and the start of data collection by MS due to a delay time in transferring solution from the reaction vessel to the MS. The first plot shown in Figure 5.31 was determined by IR, showing the aldehyde to ketone transformation. The remaining plots were all generated by ESI-MS. The most abundant species seen in the MS (at 1/20th the concentration of aldehyde and ketone) are shown in Figure 5.32.

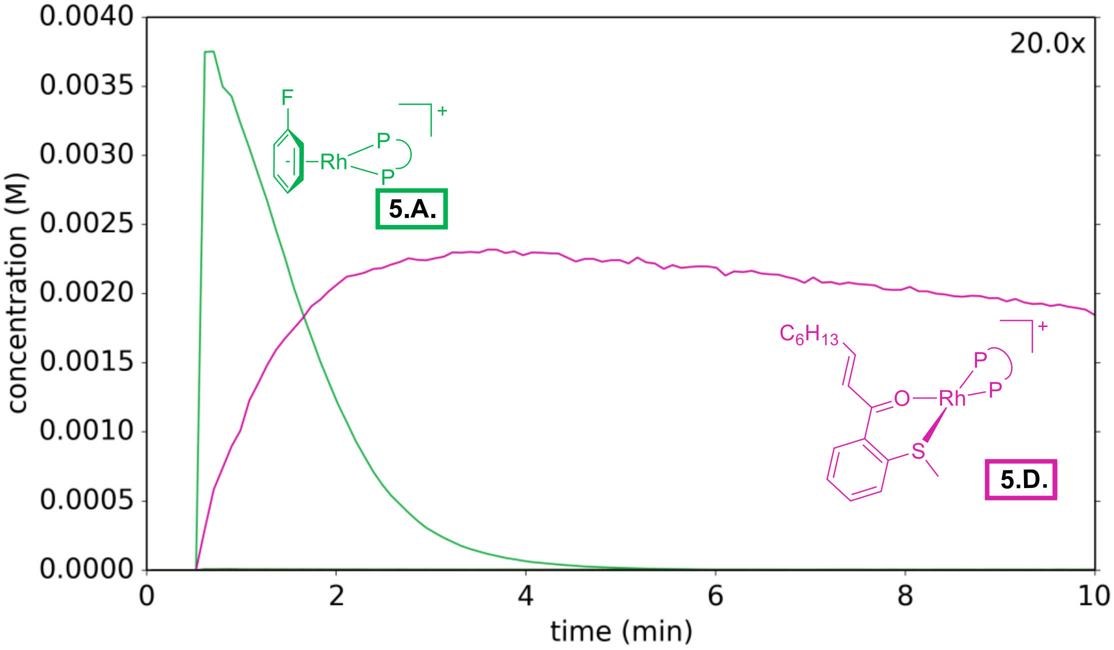

Figure 5.32. PSI ESI-MS reaction profile, showing most abundant species. Conditions: 75 mM aldehyde **5.1**, 1.13 mM alkyne **5.2**, 3.75 mM catalyst **5.A.** (5% loading) in DCE as solvent, rt.

The identity of these traces were determined by isotope matching and MS/MS (Figure 5.33). The green trace **5.A.** is the starting catalyst, which decreases after initial addition, in place of which we see formation of **5.D.**, the product ketone bound version of the catalyst which by its behaviour indicates a resting state of the catalyst.

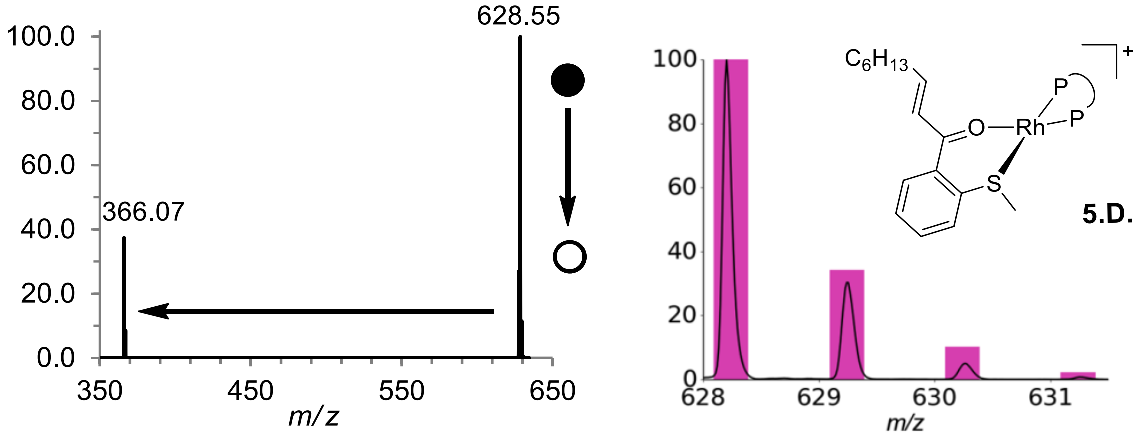

Figure 5.33. MS/MS CID of the cation *m/z* 628.6 **5.D.**(left) and experimental isotope pattern (black lines) superimposed with predicted isotope pattern of the predicted structure (coloured bars) with inset of proposed structure of **5.D** (right).

The loss of 262.5 Da is that of the product ketone, to yield the catalyst $[Rh(L_2)]^+$ at *m/z* 366.1. By repeating this reaction 7 times, an average with standard deviation of the traces was produced, portrayed in Figure 5.34. These traces show that the results are highly replicable.

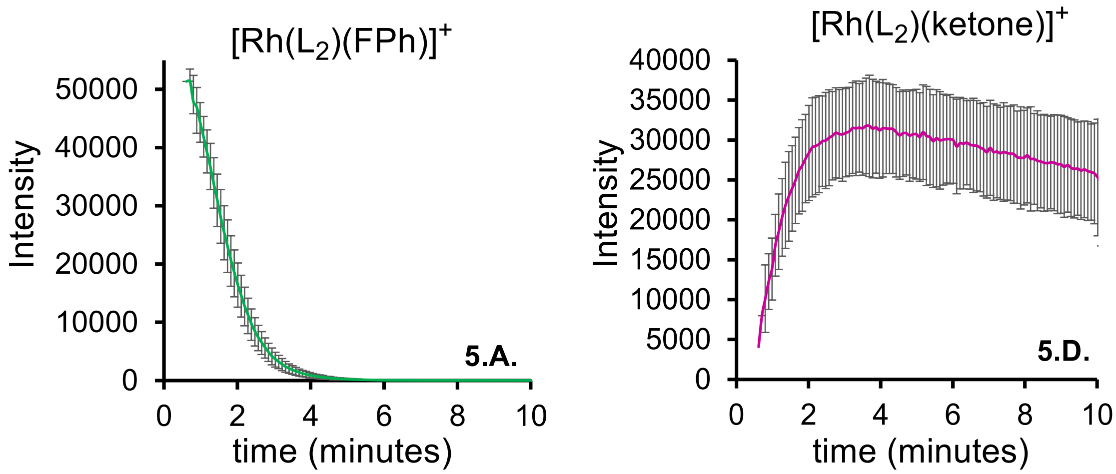

Figure 5.34. PSI ESI-MS reaction traces of **5.A**. (left) and **5.D** (right) error bars are ± one standard deviation of each data point for 7 trials.

The next set of traces are at a much lower abundance, 8000× lower abundance than substrates and products, and were found to be mainly catalyst impurities.

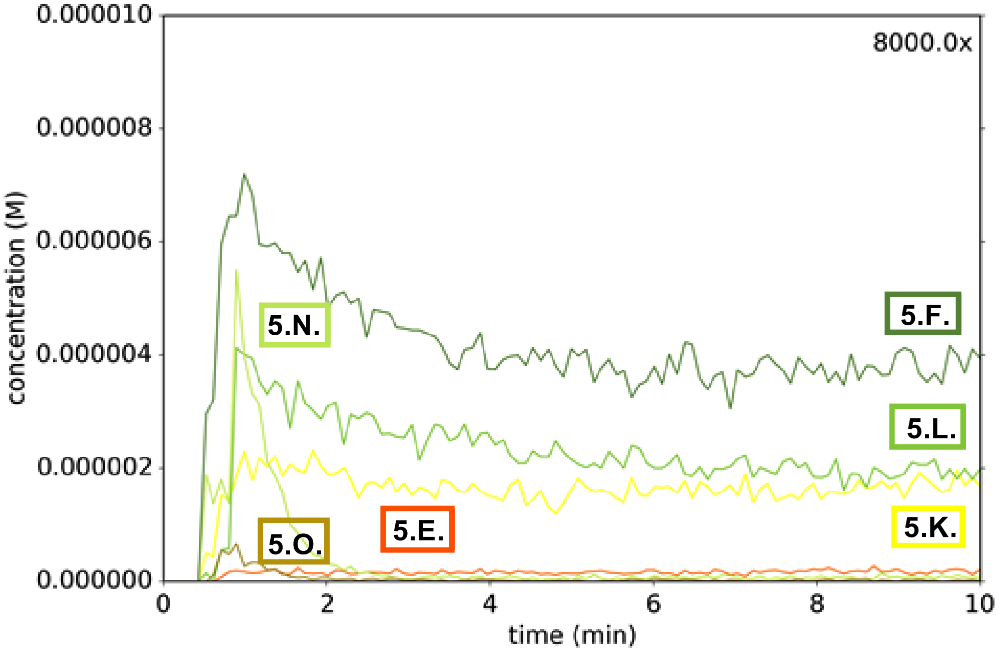

Figure 5.35. PSI ESI-MS reaction profile, showing intermediate abundance species. Conditions: 75 mM aldehyde **5.1**, 1.13 mM alkyne **5.2**, 3.75 mM catalyst **5.A.** (5% loading) in DCE as solvent, RT.

Species **5.F**. appears when catalyst is added and remains throughout the reaction, although at a lesser abundance than at the beginning of the reaction. **5.F**'s identity was determined to be the decarbonylated version of the acyl-hydride bound catalyst. The isotope pattern matched quite well and MS/MS of that peak gave results indicative of the decarbonylation product (Figure 5.36). The presence of this species indicate that there is a small amount of decarbonylation happening, and the decarbonylation pathway is not shut down completely with this catalyst, or under the reaction conditions applied. The dynamics of this trend indicates that this species is formed more at the beginning of the reaction, but does decrease in abundance, indicating that its formation is reversible, or it is degrading into something else.

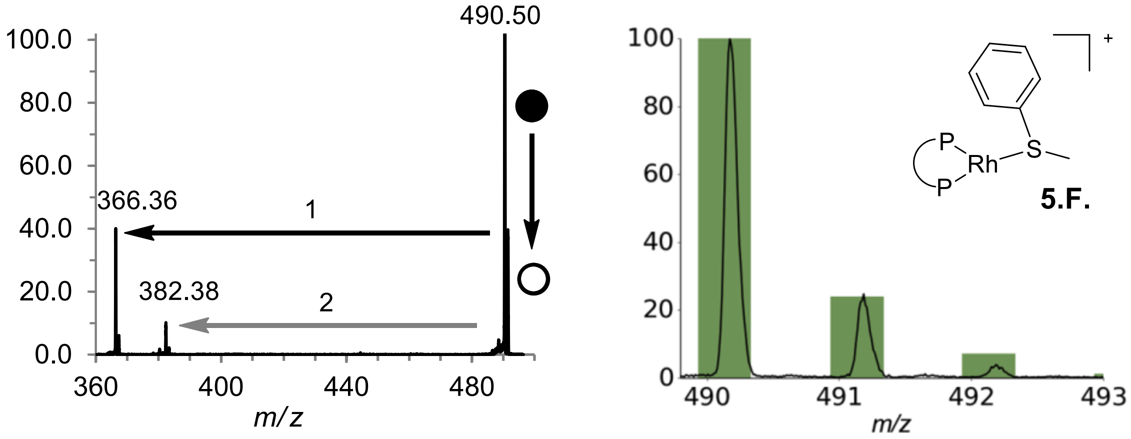

Figure 5.36. MS/MS CID of the cation *m/z* 490.5 **5.F**. (left) and experimental isotope pattern (black lines) superimposed with predicted isotope pattern of the predicted structure (coloured bars) with inset of proposed structure of **5.F** (right).

The MS/MS of complex **5.F.** has an initial neutral loss 1 of 124.14 Da, forming the unsaturated $[Rh(L_2)]^+$ at *m/z* 366.4 That loss being that of SMePh which would be the decarbonlylated product of the aldehyde. The decarbonylation pathway is understood to go through a reversible carbonyl deinsertion, which is followed by reductive elimination of the alkyl and also possible loss of CO.[107,108] A prediction of the possible decarbonylation pathway is shown in Scheme 5.13. A second loss of 108.1 Da is also observed, probably cyclooctadiene, to render the cation *m/z* 382.4 which most likely is $[Rh(L_2)O]^+$. Thus it is most likely that there are two overlapping species present within the MS/MS that is presented here.

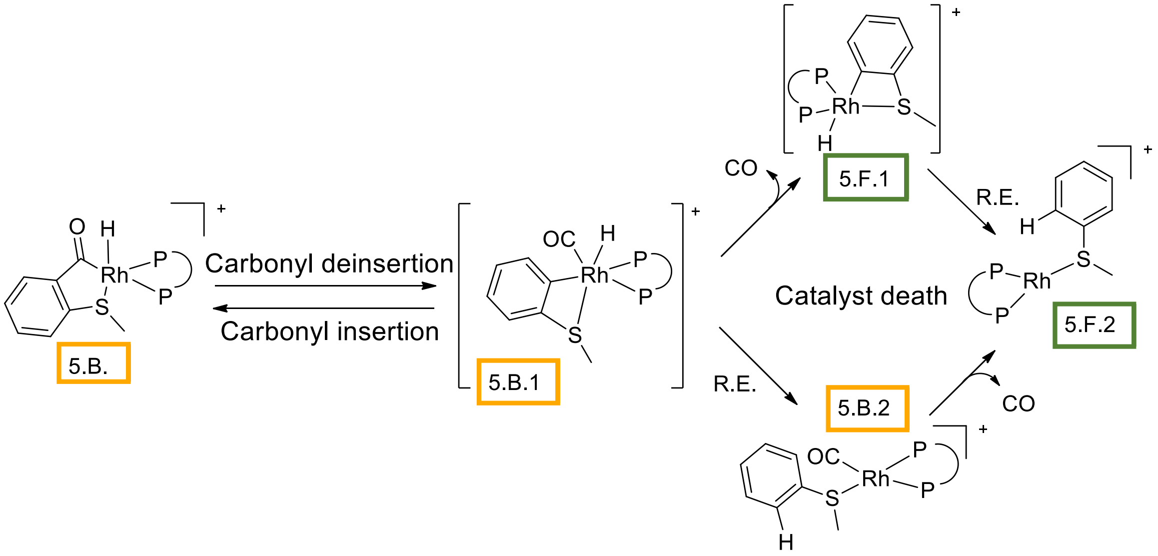

Scheme 5.13. Possible decarbonylation mechanisms.

The species that would be observed if this mechanism is true had been broken into two categories, by *m/z* ratio. **5.B**, **5.B.1**, and **5.B.2** are isobaric while **5.F.1** and **5.F.2** are isobaric. By ESI-MS we were not able to distinguish between the **5.B** species as they are also expected to produce the similar MS/MS dissociation patterns, the loss of CO and the loss of MeSPh should be seen, **5.B** might be expected to lose CO first a lower collision energies than MeSPh, while **5.B.2** might be expected to lose MeSPh at lower energies than its CO. Distinguishing between **5.F.1** and **5.F.2** could be possible based on the bond dissociation energy of MeSPh, less energy should be required for that dissociation in **5.F.2** than **5.F.1**, but the overall dissociation pattern should be the same. **5.F.1** is unlikely to be stable due to the strain on the four membered ring thus **5.F.2** is probably the structure of **5.F** that is being detected.

The light green trace **5.L** also appears when the catalyst is added, was determined to be present in the starting catalyst, and stays relatively constant throughout duration of the reaction.

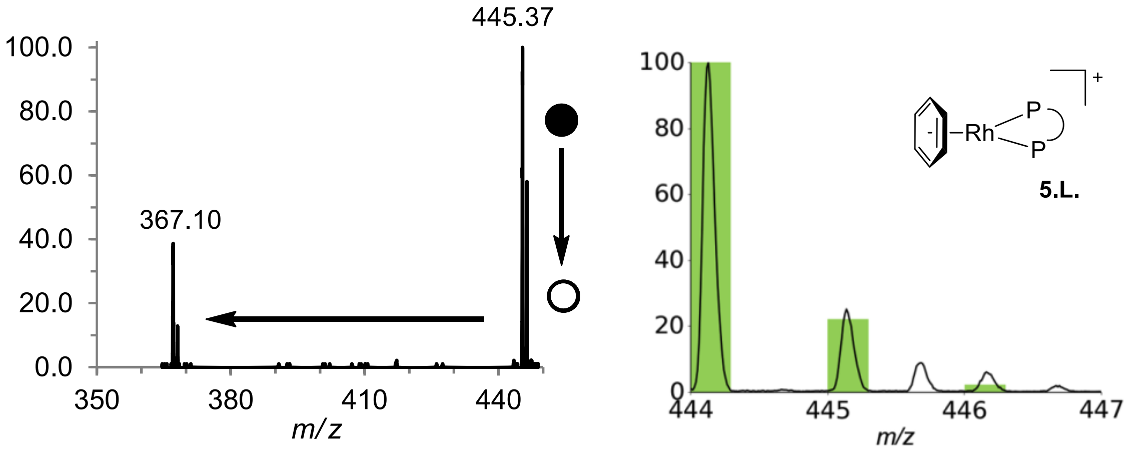

Figure 5.37. MS/MS CID of the cation *m/z* 445.4 **5.L**(left) and experimental isotope pattern (black lines) superimposed with predicted isotope pattern of the predicted structure (coloured bars) with inset of proposed structure of **5.L** (right).

The MS/MS of **5.L** was found to be the neutral loss of 78.3 Da, which was determined to be benzene, to produce the fragment $[Rh(L_2)]^+$ at *m/z* 367.1 (Figure 5.37). An explanation for the presence of benzene is that the catalyst was synthesized in fluorobenzene, which inevitably contains a small amount of benzene. The $[Rh(L_2)]^+$ preferentially binds to benzene over FPh as was shown in Chapter 2.

The yellow trace **5.K** appears when the catalyst is added, was determine to be present in the starting catalyst, and exhibited a temporal evolution that indicates it does not take part in the reaction, remaining at essentially the same abundance throughout reaction progress.

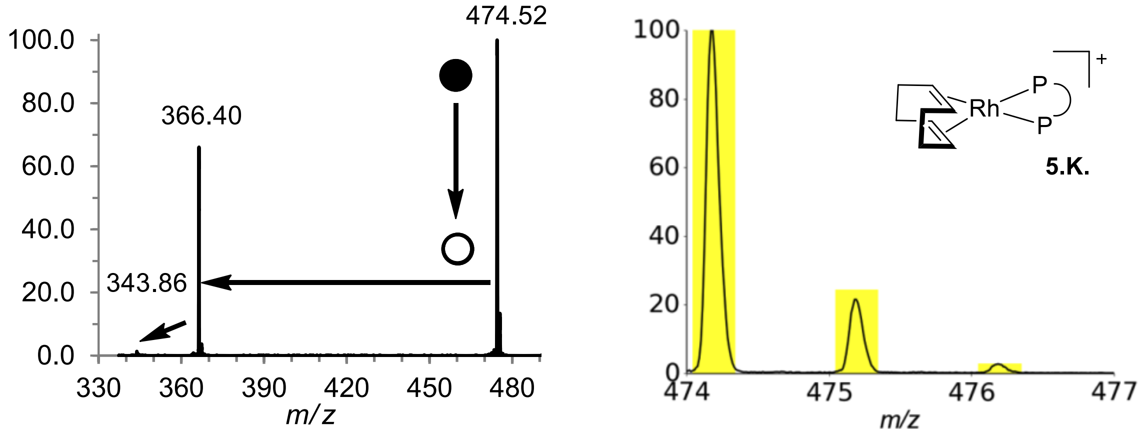

Figure 5.38. MS/MS CID of the cation *m/z* 474.5 **5.K** (left) and experimental isotope pattern (black lines) superimposed with predicted isotope pattern of the predicted structure (coloured bars) with inset of proposed structure of **5.K** (right).

MS/MS of **5.K.** shows the neutral loss of 108.1 Da to the formation of the fragment $[Rh(L_2)]^+$ at *m/z* 366.4 (Figure 5.38). This mass corresponds to that of cyclooctadiene (COD). The starting catalyst **5.A** is synthesized from $[Rh(COD)_2]^+$ through a hydrogenation in the presence of the bisphosphine ligand and FPh. **5.K** is an incomplete product of the reaction for the synthesis of the starting catalyst **5.A**. Again, its temporal evolution is such that it is inert in the reaction would be expected as the COD ligand would bind strongly to Rh with the advantageous chelate effect.

The dynamics of the light green trace **5.N** indicates that it is taking part in the reaction as it goes away rapidly throughout the fastest part of the reaction, it was also determined to be present in the starting catalyst solution.

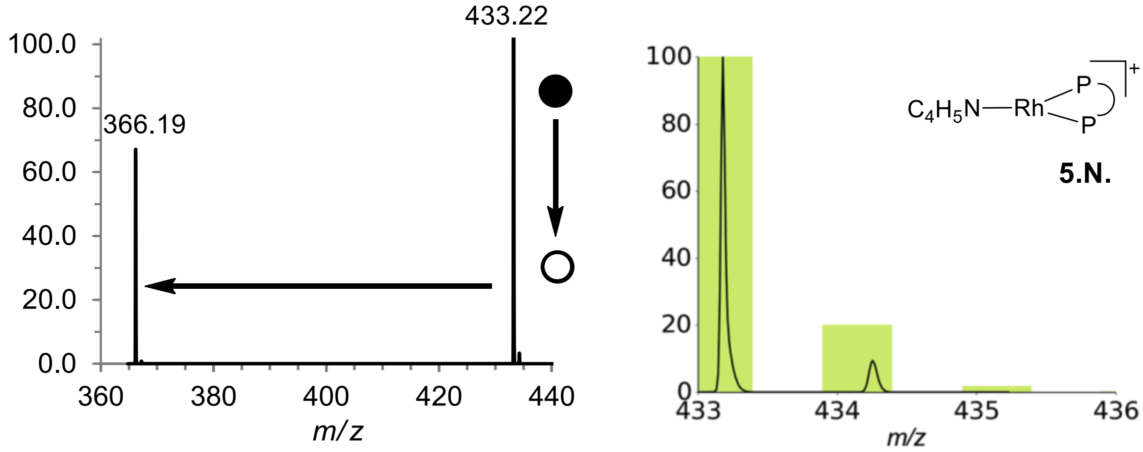

Figure 5.39. MS/MS CID of the cation *m/z* 433.2 **5.N** (left) and experimental isotope pattern (black lines) superimposed with predicted isotope pattern of the predicted structure (coloured bars) with an inset of proposed structure of **5.N** (right).

The structure of **5.N** has not been assigned, but its mass and MS/MS information has indicated that it is made up of $[Rh(L_2)]^+$ and a neutral mass of 67 Da (Figure 5.39). The most accurate mass prediction for the neutral mass lost is the formula C_4H_5N. A structure to satisfy this formula could be that of pyrrole, thus the identity of **5.N** could be $[Rh(L_2)(pyrrole)]^+$. Pyrrole is used as a stabilising agent in some chlorinated solvents, acting to slow oxidation and condensation reaction.[109] The pyrrole could be acting as an L-type ligand with the nitrogen as a 2 electron donor, to then be displaced by the aldehyde **5.1** in the hydroacylation reaction, **5.N** thus acting as a precatalyst. This hypothesis was tested by addition of pyrrole to a solution of **5.A** in DCE and observing the speciation by MS as shown in Figure 5.40.

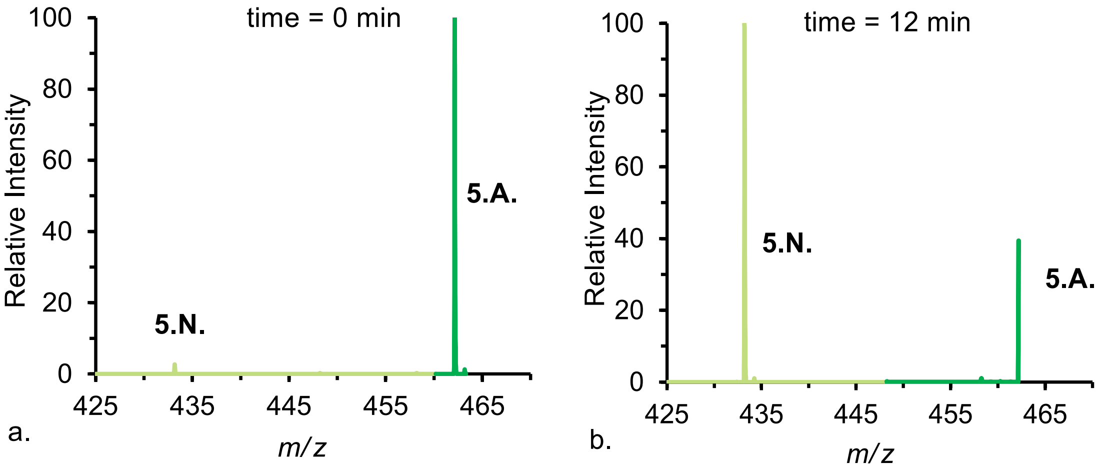

Figure 5.40. Speciation of **5.A** to **5.N** a. before addition of pyrrole, b. 12 minutes after addition of pyrrole to a solution of **5.A**. in DCE.

After 12 minutes the majority of the rhodium was now in the form of **5.N** which adds to the plausibility of **5.N** being the pyrrole adduct as shown in Figure 5.39.

5.E was found to be present in the initial starting solution of the catalyst and stays constant throughout the reaction. It is proposed that **5.E** is made up of [Rh(L_2)(E)] where E is an L type ligand off mass 111 Da. As this is an odd mass, it is likely to contain an odd number of nitrogens. MS/MS of this species was collected and the most likely chemical formula for this would be $C_7H_{13}N$ which would have a monoisotopic mass of 111.1 Da (Figure 5.41).

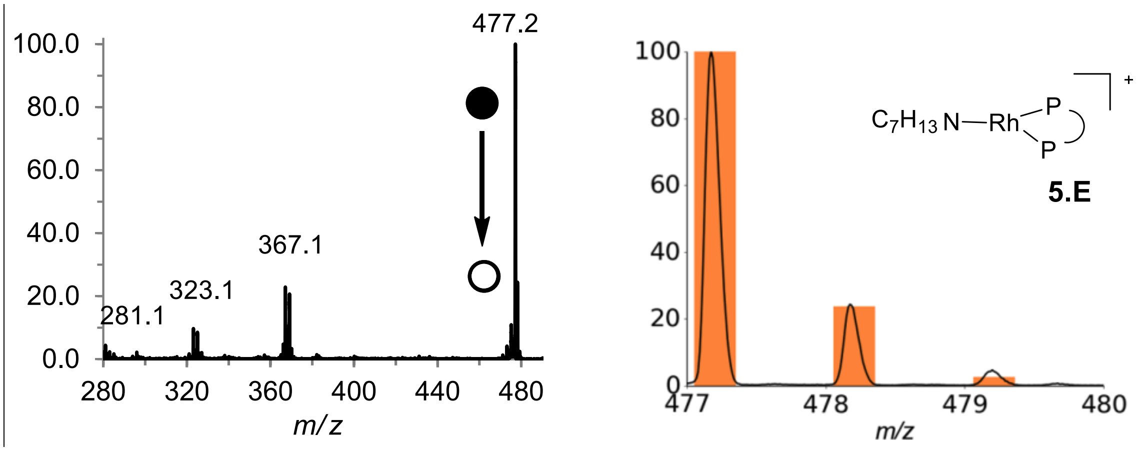

Figure 5.41. MS/MS CID of the cation *m/z* 477.2 **5.E** (left) and experimental isotope pattern (black lines) superimposed with predicted isotope pattern of the predicted structure (coloured bars). Inset of proposed structure of **5.E** (right).

A species at *m/z* 478.2 was seen to be present at start of reaction, but diminished in intensity over the duration of reaction. Through MS/MS and isotope matching **5.O** was determined to a version of the starting catalyst where the ligand had undergone oxidation to form a phosphine oxide (Figure 5.42).

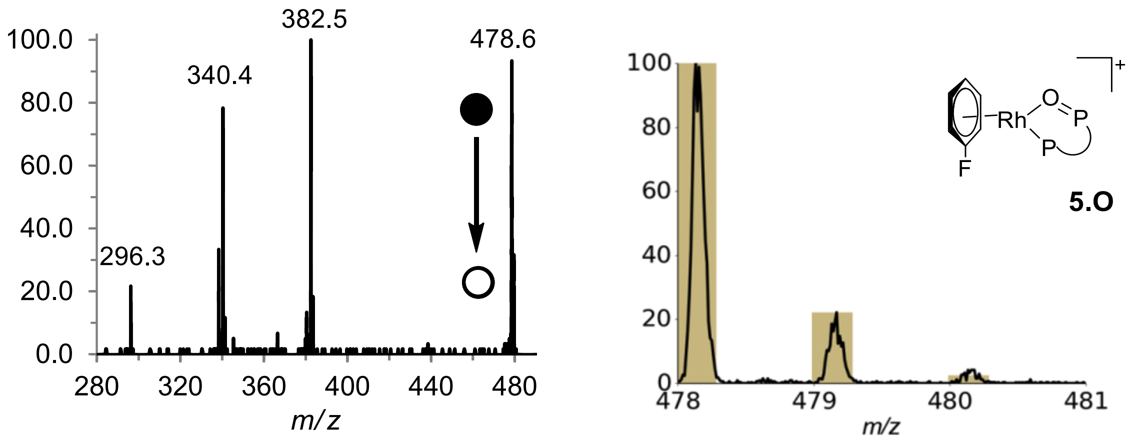

Figure 5.42. MS/MS CID of the cation *m/z* 478.2 **5.E** (left) and experimental isotope pattern (black lines) superimposed with predicted isotope pattern of the predicted structure (coloured bars). Inset of proposed structure of **5.E** (right).

By repeating the catalytic reaction 7 times, an average with standard deviation of the traces was produced, portrayed in Figure 5.43. These traces show that the results are replicable.

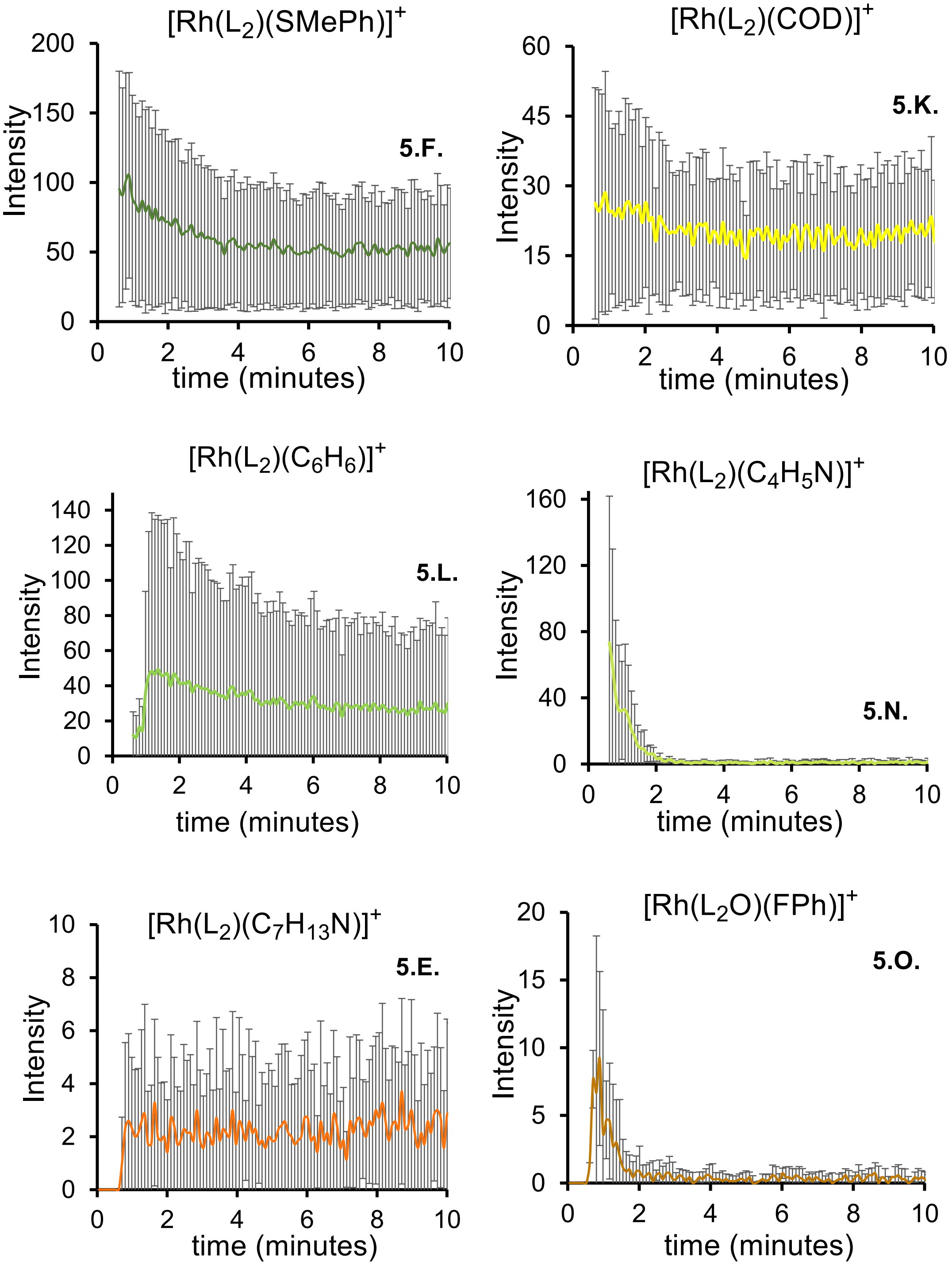

Figure 5.43. PSI ESI-MS reaction traces of **5.F**., **5.K**, **5.L.**, **5.N**., **5.E**, **5.O**. error bars are ± one standard deviation of each data point for 7 trials.

The next trace are at a much lower abundance, 50,000× lower abundance than the substrates and products, and were found to be catalytic intermediates (Figure 5.44).

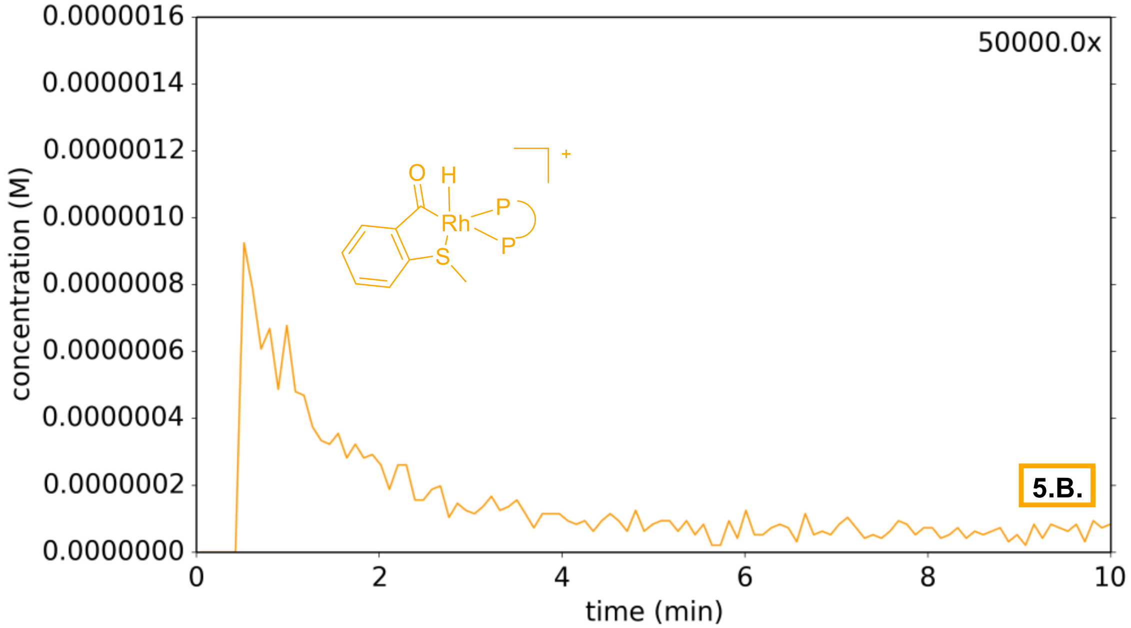

Figure 5.44. PSI ESI-MS reaction profile, low abundance species. Conditions: 75 mM aldehyde **5.1**, 1.13 mM alkyne **5.2**, 3.75 mM catalyst **5.A.** (5% loading) in 1,2–dichloroethane as solvent, rt.

The dynamics of **5.B** indicates that it is taking part in the reaction as it goes away rapidly throughout the fastest part of the reaction, and it was determined to **not** be present in the starting catalyst, thus it has to be an intermediate.

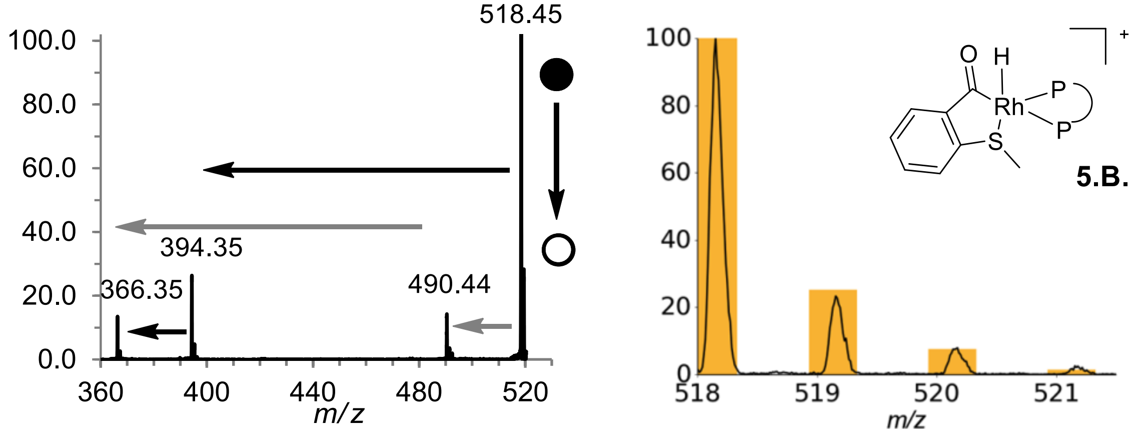

Figure 5.45. MS/MS CID of the cation *m/z* 518.5 **5.B** (left) and experimental isotope pattern (black lines) superimposed with predicted isotope pattern of the predicted structure (coloured bars) with inset of proposed structure of **5.B** (right).

MS/MS of **5.B.** shows the neutral loss of 124.1 Da followed by 28.0 Da as is shown by black arrows, to form the fragment $[Rh(L_2)]^+$ at *m/z* 366.4. The grey arrows show the loss of 28.0 Da, followed by the loss of 124.1 also resulting in the fragment $[Rh(L_2)]^+$ at *m/z* 366.4. The loss of 28 corresponds to the loss of a CO, while the loss of 124.1 corresponds to the loss of MeSPh. The CID process is causing the reductive decarbonylation for the elimination of MeSPh and CO separately.

By repeating this reaction 7 times, an average with standard deviation of the traces was produced, portrayed in Figure 5.46. These traces show that the results are replicable.

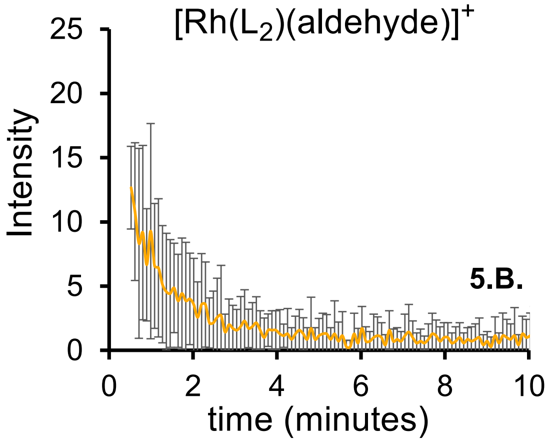

Figure 5.46. PSI ESI-MS reaction traces of **5.B**, error bars are ± one standard deviation of each data point for 7 trials.

The least abundant traces will be discussed next, at a magnification of 100000× on the Y-axis. All of these species grew in over time, a trend that would be predicted of decomposition products. These are portrayed in grey and they are not considered to be active in the reaction mechanism towards creating ketone product (Figure 5.47).

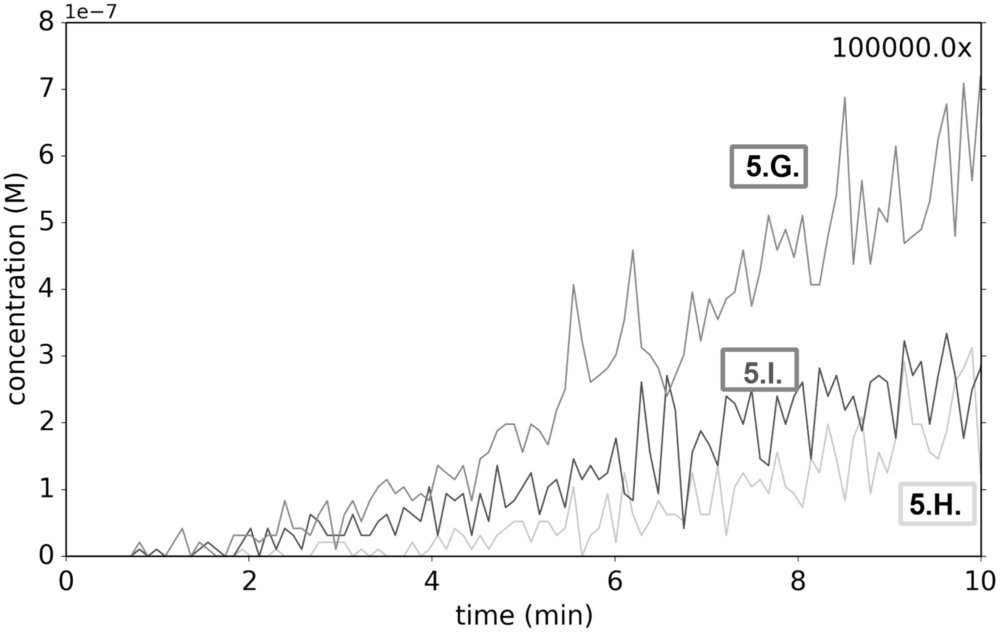

Figure 5.47. PSI ESI-MS reaction profile, decomposition product, ultra-low abundance species. Conditions: 75 mM aldehyde **5.1**, 1.13 mM alkyne **5.2**, 3.75 mM catalyst **5.A.** (5% loading) in DCE as solvent, rt.

5.G. - **5.I.** was characterized through MS/MS CID and isotope matching (Figure 5.48).

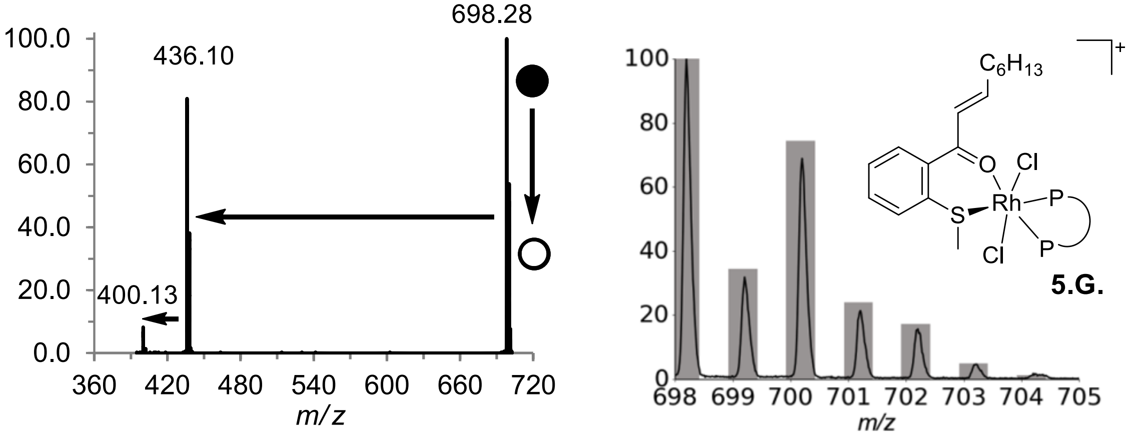

Figure 5.48. MS/MS CID of the cation *m/z* 698.3 **5.G** (left) and experimental isotope pattern (black lines) superimposed with predicted isotope pattern of the predicted structure (grey bars) with inset of proposed structure of **5.G** (right).

The initial loss of 262.2 Da is due to the loss of the ketone product, this is followed by a loss of 35, to reach a *m/z* 400.1, from which at higher collision voltages would likely dissociate to 366.0 *m/*z which would be $[(\mathrm{Rh}(L_2))]^+$. As one reaches higher collision voltages, sensitivity drops as more ions are accelerated into the collision gas and lose charge, this was the case at higher voltages, thus no higher collision voltage data was collected. The chlorides can be a result of trace amounts of chloride in the DCE solvent[110] which over time bind to the rhodium catalyst.

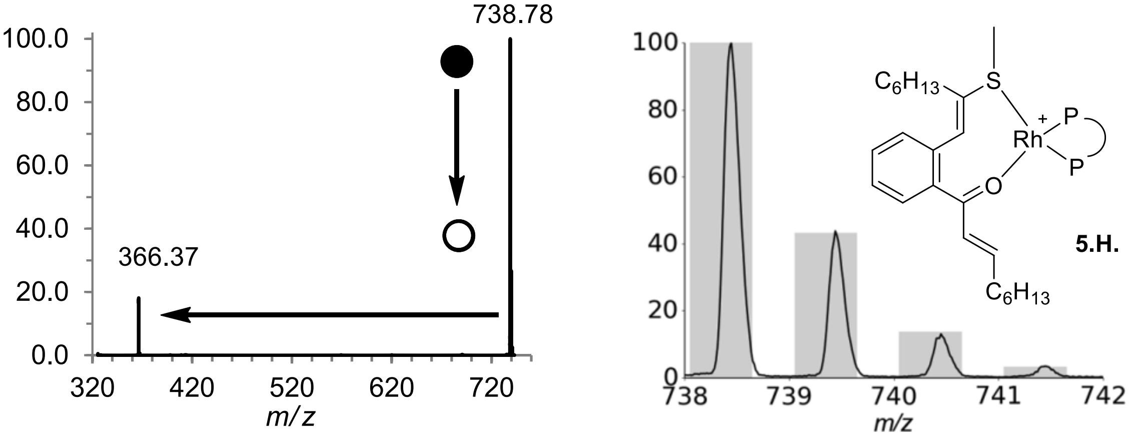

Figure 5.49. MS/MS CID of the cation *m/z* 738.78 **5.H** (left) and experimental isotope pattern (black lines) superimposed with predicted isotope pattern of the predicted structure (grey bars) with inset of proposed structure of **5.H** (right).

5.H dissociates to 366.0 *m/*z $[(\mathrm{Rh}(L_2))]^+$ by neutral loss of 372.4 Da which is the mass of one aldehyde and two of the alkynes employed (Figure 5.49). As an overabundance of alkyne was used during these reactions, it is reasonable that this species may form. It is possible that **5.H.** forms form **5.D.** reacting with another alkyne, or that there is another parallel reaction that is happening which is C-C bond formation to form an α-β unsaturated alkyne, which then undergoes hydroacylation at the alkyne to form the double alkyne inserted hydroacylation product. There is literature precedent for Rh catalyzed coupling of alkynes[111,112], but in the absence of the observation of any alkynecoupled rhodium species, we disregarded this possibility. The possibility of **5.D.** reacting to form the species **5.H.** is possible by carbothiolation where an alkyne is inserted in the carbon-sulfur bond. Carbothiolation has been shown to be active in similar catalytic systems[113–115] and would explain the behaviour of the product bound trace **5.D.** as it has a slight decreases over time of reaction, it could be forming **5.H.** **5.I** has an *m/z* 32 greater than **5.H.** And **5.I** is thus predicted to be an oxygenated version of **5.H** (Figure 5.50).

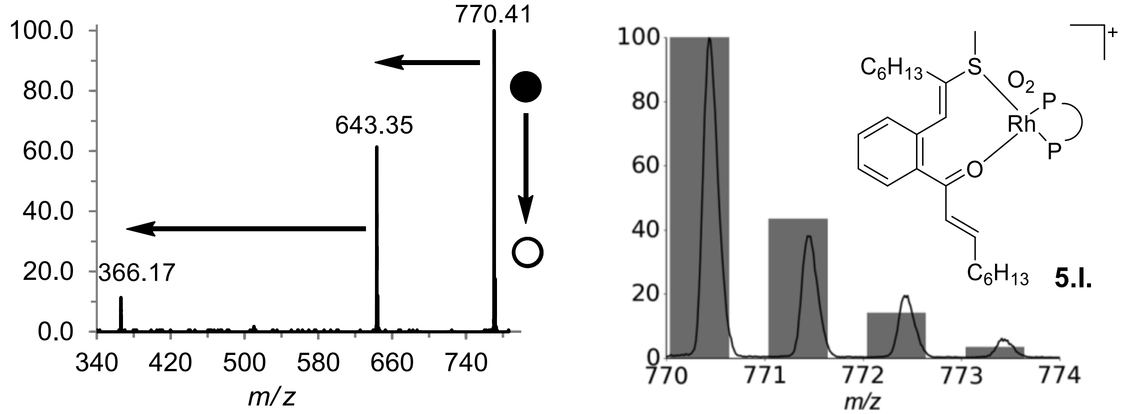

Figure 5.50. MS/MS CID of the cation *m/z* 770.4 **5.I** (left) and experimental isotope pattern (black lines) superimposed with predicted isotope pattern of the predicted structure (grey bars) with inset of proposed structure of **5.I** (right).

The MS/MS of **5.I.** is perplexing as there is an initial loss of 127.1 Da, followed by a loss of 277.2 Da for the formation of the catalyst fragment *m/z* 366.2 $[(Rh(L_2)]^+$ (Figure 5.50). Both losses are odd numbers, which would indicate that they each contain an odd number of nitrogens. The 127 could be iodide, or it could actually be 126 and actually be the mass of one alkyne (110) with one oxygen (16), while the 277 loss could be the loss of the product alkyne (262) and one oxygen (16) (total of 278). The exact structure and formula of **5.I** is still unknown at this time.

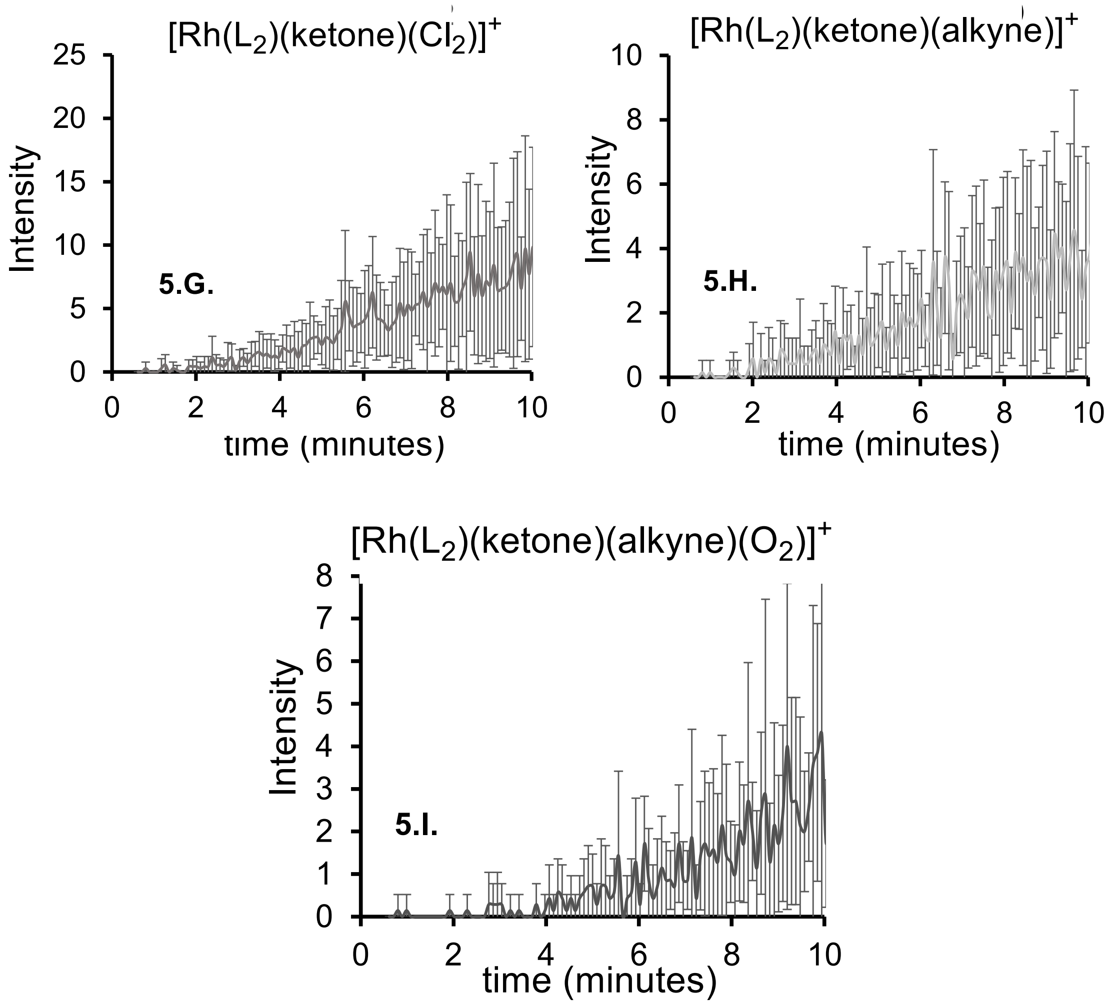

Figure 5.51. PSI ESI-MS reaction traces of **5.G.**, **5.H**, and **5.I.** error bars are ± one standard deviation of each data point for 7 trials.

We were able to reproduce the reaction 7 times, where we can see that the percentage error appears much smaller for the high concentration species (Figure 5.34, Figure 5.43), than the low concentration species (Figure 5.46, Figure 5.51), but that for all of these low concentration species shown here, they do follow their trends within error and the trends that they exhibit can be trusted. For example the intermediate behaviour, being formed initially then decreasing as the reaction progresses, and the decomposition products forming continuously.

Putting all of that information together we were able to come up with a mechanism (Figure 5.52) where coloured and grey species had been observed.

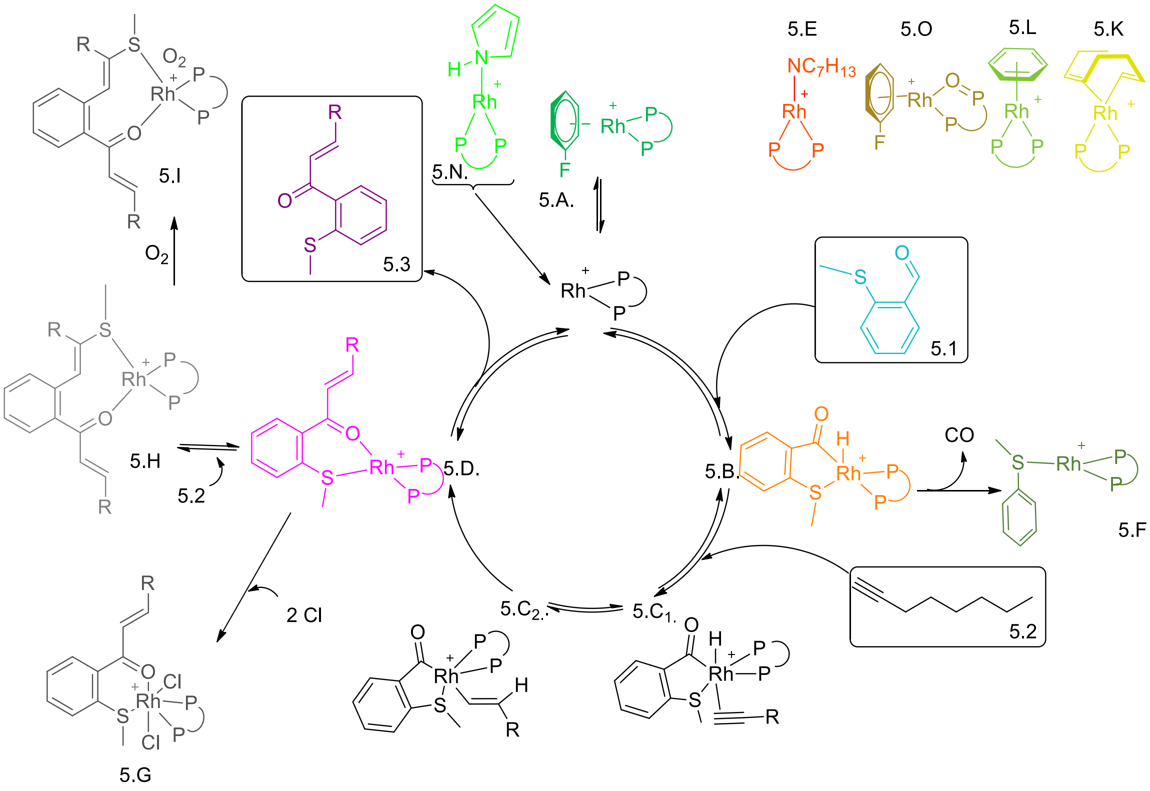

Figure 5.52. Proposed reaction mechanism, coloured and grey species were observed by IR or ESI-MS.

5.4.3 Conclusions

We reported on the hydroacylation of an alkyne as catalyzed by a cationic rhodium catalyst **5.A** using flow IR to measure the overall progress and PSI-ESI-MS to measure the temporal evolution of catalytically-relevant species. IR-MS showed to be an effective method of studying catalytic reactions as we were able to measure abundances across five orders of magnitude. This technique gave new insight into the hydroacylation reaction (Scheme 5.9Scheme 2.1). It was determined that the reaction is first order in aldehyde concentration, is small but positive in order to alkyne concentration, and has temperature dependence. We were able to track the dynamics of the acyl-hydride intermediate that forms during reaction, and also monitor the appearance of a decarbonylated side product that is due to catalyst reductive decarbonylation. The resting state of the catalyst was found to be the product ketone bound catalyst. Different off cycle species of the catalyst were identified, namely a chlorine-poisoned catalyst **5.G** due to trace impurities in solvent, the formation of a doubly alkyne inserted product bound catalyst **5.H** as well as a possible oxygenated version of that doubly alkyne inserted product **5.I**. The formation of these doubly alkyne insertion products could be minimized if alkyne was not used in excess. However, the excess alkyne can serve to minimize the poisonous decarbonylation pathway, especially with the lack of a coordinating solvent. Favourably the formation of these double insertion products is much slower than the reaction of the formation of the target ketone product **5.3,** so the best way to get the most yield with the least amount of by-products out of this reaction would be to isolate the product immediately after formation, not letting the reaction continue to incorporate alkyne into the product that had formed.

5.5 Conclusions

Catalytic reactions are especially difficult to study under real reaction conditions, mainly because the abundance of the catalyst is much lower than that of the substrates. Few techniques are sensitive enough to determine the catalyst speciation while at the same time ignoring the large quantities of substrate, products and solvent around. We have exploited the high dynamic range of electrospray ionization mass spectrometry (ESI-MS) along with the use of charged tags to enable detection of otherwise-neutral species and pressurized sample infusion (PSI) to provide continuous monitoring of catalytic reactions. While this method is powerful, the dynamic range was still limited to about three orders of magnitude, so the catalytic species observed were for the most part the resting state and/or the most abundant species. The charged tags employed were also found to interfere with catalysis, and revealed reaction dynamics that were not representative of the same reaction in the absence of the charged tag. To harness the full potential of ESI-MS to probe even deeper into even less abundant species, ESI-MS was linked with a less sensitive technique to monitor overall reaction progress. This left the ESI-MS to focus solely on the low abundance, catalytically relevant species. The method of tandem measurement by an additional method along with ESI-MS is promising and can be applied to other methods as well, beyond IR, such as UV-Vis and NMR, as IR might not be suitable for all reactions.

5.6 Experimental

General

Solvents were HPLC grade and purified on an MBraun solvent purification system. Acetone was obtained from Alfa Aesar, dried over calcium sulfate, fractionally distilled, followed by storage over molecular sieves for a minimum of 24 to a maximum of 48 hours. 1,2-dichloroethane was obtained from Caledon Labs, vacuum distilled, then stored over 4 Å molecular sieves for minimum 48 hours prior to use.
2-(methylthio)benzaldehyde was synthesized then vacuum distilled prior to use. 1-octyne was obtained from Sigma Aldrich, dried over calcium hydride, and distilled before use. Charged aldehyde **5.11** was supplied by Indrek Pernik from the Weller group, Oxford. All other chemicals were supplied by Sigma Aldrich, Acros, or Alfa Aesar and used without further purification. Standard inert atmosphere glovebox and Schlenk technique was used to achieve air-free conditions when rhodium complexes or air sensitive phosphines were handled. ^{1}H NMR was calibrated to $CHCl_3$ in $CDCl_3$ at 7.27 ppm.

Synthesis of N-(diisopropylphosphino)-1,1-diisopropyl-N-methylphosphinamine (PNP^{ipr})

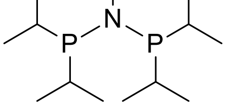

Chlorodiisopropylphosphine (1.0g 6.55 mmol) was added dropwise to a solution of methylamine hydrochloride (0.221 g, 3.275 mmol) and trimethylamine (1.37 ml, 9.83 mmol) in 20 ml dichloromethane. The resultant solution was stirred at room temperature overnight. The suspension obtained was filtered through alumina with dichloromethane as eluent then through a standard cannula filter. The solvent was removed under reduced pressure to yield a clear colourless oil. (0.278g, 32%) ^{1}H NMR: (300MHz, CDCl$_3$) δ 1.09 (24H, m), 1.97 (4H, sept, J 7.1 Hz), 2.67 (3H, t, ^{3}JPH 2.5 Hz); ^{31}P{^{1}H} NMR: (121 MHz, CDCl$_3$) δ 92.71 (s).Method adapted from literature, and characterization is consistent.[28]

Synthesis of [bis-cyclo-octa-1,5-diene-rhodium(I)]$^+$[BAr$^F{}_4$]$^-$ ([Rh(COD)$_2$]$^+$ [BAr$^F{}_4$]$^-$)

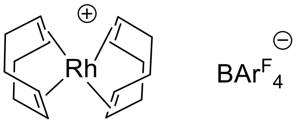

1,5-Cyclootadiene (0.127 ml, 1.03 mmol) was added dropwise to Chloro(1,5-cyclooctadiene)rhodium(I) dimer (0.1658 g, 0.336 mmol) in dichloromethane (1.8 ml) at room temperature, to this stirring solution was added dropwise a suspension of sodium [tetrakis[3,5-bis(trifluoromethyl)phenyl]borate] in dichloromethane (3.5 ml), resulting in a colour change to dark red. The solution as stirred for 20 minutes, then filtered through anhydrous MgSO$_4$ into hexanes, resulting in deep red crystals. These crystals were washed with hexanes (x3) and recrystallized from dichloromethane/hexanes. (0.650 g, 81%) ^{1}H NMR: (300MHz, CDCl$_3$) δ 2.43 (16H, s, COD-CH$_2$), 5.12 (8H, s, COD-CH), 7.56 (4H, s, Ph), 7.71 (8H, s, Ph); ESI-MS (+) *m/z* 319.8 (calc: 319.09), (-) *m/z* 862.9 (calc: 863.06). Method adapted from literature, characterization is consistent.[116]

Preparation of [Rh(PNP^{ipr})(FPh)]$^+$ [BAr$^F{}_4$]$^-$ (5.A)

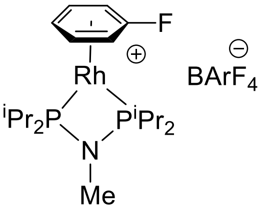

PNP ^{ipr} in FPh (2.83 ml, 0.09M) was added to a solution of $[Rh(COD)_2]^+$ $[Bar^F{}_4]^-$ (300 mg, x mmol) in FPh (5 ml). Upon addition of the ligand the solution changed colour from dark red to bright orange. The solution was stirred for one hour at room temperature. 3 successive freeze-pump thaw cycles was followed by filling the reaction vessel with H_2 at -196°C, sealing the flask, and letting it warm to room temperature. The solution was then stirred at room temperature for 1.5 hours, the solvent was removed *in vacuo* from the resultant bright yellow solution. The oily solid obtained was washed and sonicated with hexanes 3x, followed by recrystallization from FPh/Hexanes to produce small bright yellow crystals. $^{31}P\{^1H\}$ NMR: (121 MHz, $CDCl_3$) δ 80.98 (dd, ^1J(PRh) 178 Hz, J (PF) 4 Hz). ^1H NMR: (300 MHz, $CDCl_3$) δ 1.05-1.09 (24H, m, CH_3), 2.01-2.19 (5H, m, CH), 2.58 (3H, t, ^{3} J (PH) 9.8 Hz, N-CH_3), 5.94 (1H, t, J 6.0 Hz, η^6-FPh), 6.60 (2H, m, , η^6-FPh), 6.70 (2H, m, η^6-FPh), 7.57 (4H, s), 7.74 (8H, s) Method adapted from literature, characterization is consistent.[116]

Synthesis of 2-(Methylthio)benzaldehyde (5.1)

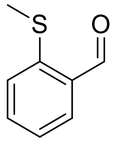

A solution of methanethiol sodium salt (17.7 mL, 3.0 M in water, 53.1 mmol) was added dropwise to a solution of 2-fluorobenzaldehyde (5.09 mL, 48.3 mmol)) in DMF (60 mL) at room temperature. The reaction was stirred for 16 hours after which water (40 mL) was added to the mixture. The product was extracted with Et_2O (3′ 20 mL). The organic layers were washed with water (20 mL) and brine (3 ′ 10 mL) then dried over $MgSO_4$ and concentrated under reduced pressure. The crude oil was purified by flash column chromatography on silica (20% EtOAc/Hexanes) to obtain aldehyde **5.5** as a yellow oil (5.5 g, 75%). IR: *v* ($C_2H_4Cl_2$, BaF_2):1462, 1560, 1589, 1680, 1695 cm^{-1}. ^1H NMR: δ (300MHz, $CDCl_3$) 2.51 (3H, s), 7.29 (1H, td, J 7.5 Hz and J 1.3 Hz), 7.33 (1H, d, J 7.9 Hz), 7.55 (1H, td, J 7.8 Hz and 1.8Hz), 7.82 (1H, dd, J 7.6 Hz and 1.6 Hz), 10.28 (1H, s); Method adapted from literature, and characterization is consistent. [117]

Charterization of 1-(2-(methylthio)phenyl)non-2-en-1-one (5.3)

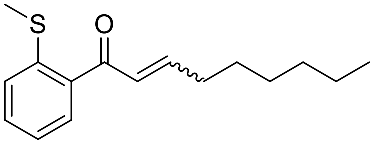

IR: *v* ($C_2H_4Cl_2$, BaF_2):1463, 1559, 158, 1615, 1651 cm^{-1}

^1H NMR: δ (300MHz, $CDCl_3$) 0.90 (3H, m), 1.34 (8H, m) (should be 8H), 2.29 (2H, qd, J 7.1 Hz and J 1.4 Hz), 2.44 (3H, s), 6.64 (1H, dt, J 15.5Hz and 1.4Hz), 6.88 (1H, dt, J 15.5 Hz and 6.9 Hz), 7.20 (1H, td, J 7.4 Hz and 1.3 Hz), 7.35 (1H, d, J 8.0 Hz), 7.44 (1H, td, J 7.5 Hz and 1.5 Hz), 7.58 (1H, dd, J 7.8 Hz and 1.3 Hz).

Synthesis of hex-5-yn-1-yltributylammonium iodide (5.203)

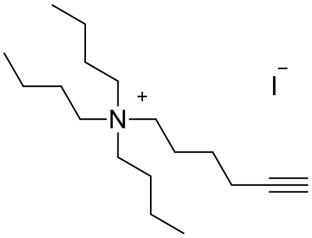

Tributylamine (3.56 g, 4.58 ml, 19.22 mmol) was dissolved in 10ml toluene at 75°C in a Schlenk flask equipped with a reflux condenser. 6-iodo-1-hexyne was added drop wise over 10 minutes (1 g, 0.633 ml, 4.8 mmol). The solution was stirred at temperature for 72 hours, and the product was isolated as a brown oily solid. ESI-MS (+) 265.9 (calc. 266.28), and 186.0 impurity as HBu_4N (calc. 186.2).

Synthesis of hex-5-yn-1-yltributylammonium hexafluorophosphate (5.23)

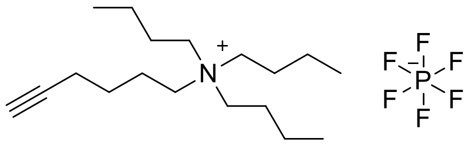

1.289 g (7.67 mmol) sodium hexafluorophosphate was dissolve in water (4 ml) and added dropwise to 0.911 g (2.315 mmol) of **5.203** dissolved in methanol (8 ml). A white precipitate formed immediately, this white solid was washed three times with water, recrystallized from cold methanol, and then dried under vacuum overnight. ^{1}H NMR: (300 MHz, $CDCl_3$) δ 3.21 (8H, m); 2.33 (2H, td, J 6.6 and 2.6 Hz); 2.00 (1H, t, J 2.49 Hz); 1.80 (2H, m); 1.63 (8H, m); 1.44 (6H, hex, J 7.4Hz); 1.01 (9H, t, J 7.32 Hz). ^{13}C NMR: (75 MHz, $CDCl_3$) δ 13.49, 19.61, 20.28 , 23.74, 24.32, 58.78, 69.84 ppm ESI-MS (+) *m/z* 266.9 (calc: 266.28), (-) *m/z* 145.0 (calc:144.96). m.p. 180°C. Crystallographic data available in Appendix B.

Catalytic Reaction Monitoring

Monitoring of IR was done with a Bruker Alpha FT-IR fitted with a transmission flowcell with BaF_2 windows, a 100 μm pathlength, and a 5 μL cell volume. A single sided interferogram was collected, and a Blackman-Harris 3-Term apodization function was applied. For each experiment 16 scans were averaged over 16 s, with a 4 s resting period. The reaction solution was circulated through the flow cell via tubing of i.d. 250 μm using a Simdos 02 Pump with a flow rate of 2.5 mL/min. A background of DCE was collected prior to each experiment, after which the pump was purged with argon gas to dry the apparatus.

Monitoring of ESI-MS was done on a Micromass Q-Tof *micro* mass spectrometer in positive ion mode using pneumatically assisted electrospray ionization: capillary voltage, 2900 V; sample cone voltage, 15V; extraction voltage, 0.5 V; source temperature, 84°C; desolvation temperature, 184°C; cone gas flow, 100 L/h; desolvation gas flow, 200 L/h; collision voltage, 2 V; MCP voltage, 2400 V (later on 2500V). No smoothing of the data was performed. Continuous sample introduction over the entire reaction time was achieved by pressurized sample infusion.

Typical charge-tagged PSI ESI-MS procedure

Charged aldehyde: A Schlenk flask under nitrogen containing a solution of the charged aldehyde (90 mM, 0.225 mmol) and 1-octyne (135 mM, 0.338 mmol) in acetone (2.5 ml) was pressurized to 2 psi using 99.995% purity argon gas.). The flask was connected to the mass spectrometer via a short length of PEEK tubing and mass spectra collection was initiated. A solution of $[Rh(PNPipr)(FPh)]^+$ $[BArF_4]^-$ in acetone (0.5 ml, 22.5 mmol/L, 0.0113 mmol) was injected into the pressurized Schlenk flask through a septum, this commenced the reaction.

Charged Alkyne: A Schlenk flask under nitrogen containing a solution of the 2-(methylthio)benzaldehyde (90 mM, 0.225 mmol) and charged octyne (135 mM, 0.338 mmol) in acetone (2.5 ml) was pressurized to 2 psi using 99.995% purity argon gas.). The flask was connected to the mass spectrometer via a short length of PEEK tubing and mass spectra collection was initiated. A solution of $[Rh(PNPipr)(FPh)]^+$ $[BArF_4]^-$ in acetone (0.5 ml, 22.5 mmol/L, 0.0113 mmol) was injected into the pressurized Schlenk flask through a septum, this commenced the reaction.

Typical IR-MS Reaction procedure

A Schlenk flask under nitrogen containing DCE was was pressurized to 2 psi using 99.995% purity argon gas. The flask was connected to the inlet of the circulation pump by PEEK tubing, the outlet of the circulation pump was connected to the entrance of the IR-flow cell, and the outlet of the flow cell was connected via PTFE tubing to a waste flask. The pump was turned on and solvent ran through the pump and flow cell into the waste flask. After about 2 ml of solvent had passed through the system, the exit tubing from the flow cell was inserted into the Schlenk flask. A background IR spectrum of solvent circulating through the flow cell was collected. The solvent was purged from the flask by removing the exit tubing and placing it into a waste flask. After all the solvent had been removed and the system purged with argon, the exit tubing was re-inserted into the Schlenk flask. A solution of 2-(methyl)thiobenzaldehyde (90 mmol/L, 0.225 mmol) and 1-octyne (135 mmol/L, 0.338 mmol) in DCE (2.5ml) was added to the empty Schlenk flask. The flask was connected to the mass spectrometer via a short length of PEEK tubing and mass spectra collection was initiated. Collection on the IR spectrometer was initiated. A solution of $[Rh(PNPipr)(FPh)]^+ [BArF_4]^-$ in DCE (0.5 ml, 22.5 mmol/L, 0.0113 mmol) was injected into the pressurized Schlenk flask through a septum, this commenced the reaction.

Bibliography

(1) Thomson, J. J. *Philosophical Magazine and Journal of Science Series 5* **1897**, *44* (269), 293–316.

(2) Thomson, J. J. *Rays of positive electricity and their application to chemical analyses*; London, New York [etc.] Longmans, Green and Co., 1913.

(3) Thomson, J. J. *Philosophical Magazine and Journal of Science Series 6* **1912**, *24* (140), 209–253.

(4) Aston, F. W. *Philosophical Magazine Series 6* **1919**, *38* (228), 707–714.

(5) Aston, F. W. *Nature.* **1919**, *104*, 334.

(6) Aston, F. W. *Nature.* **1919**, *104*, 393.

(7) Cavendish Laboratory. Aston's Third Mass Spectrograph http://www-outreach.phy.cam.ac.uk/camphy/massspectrograph/massspectrograph8_1.htm (accessed Mar 3, 2015).

(8) Gross, J. H. *Mass Spectrometry: A Textbook*, 2nd ed.; Springer Science & Business Media: Heidelberg University, 2011.

(9) Dempster, A. J. *Philosophical Magazine Series 6* **1916**, *31* (185), 438–443.

(10) Cech, N. B.; Enke, C. G. *Mass Spectrom. Rev.* **2001**, *20* (6), 362–387.

(11) Mora, J. F. de la; Van Berkel, G. J.; Enke, C. G.; Cole, R. B.; Martinez-Sanchez, M.; Fenn, J. B. *J. Mass Spectrom.* **2000**, *35* (8), 939–952.

(12) Iribarne, J. V.; Thomson, B. A. *The Journal of Chemical Physics* **1976**, *64* (6), 2287–2294.

(13) Henderson, W.; McIndoe, J. S. *Mass Spectrometry of Inorganic and Organometallic Compounds: Tools - Techniques - Tips*; John Wiley and Sons: New York, 2005.

(14) Dawson, P. H. *Quadrupole Mass Spectrometry and Its Applications*; American Inst. of Physics, 1997.

(15) Hoffmann, E. de; Stroobant, V. *Mass Spectrometry: Principles and Applications*; John Wiley & Sons, 2007.

(16) Jirásko, R.; Holčapek, M. *Mass Spectrom Rev* **2011**, *30* (6), 1013–1036.

(17) Eelman, M. D.; Blacquiere, J. M.; Moriarty, M. M.; Fogg, D. E. *Angewandte Chemie International Edition* **2008**, *47* (2), 303–306.

(18) Lubben, A. T.; McIndoe, J. S.; Weller, A. S. *Organometallics* **2008**, *27* (13), 3303–3306.

(19) Patiny, L.; Borel, A. *J. Chem. Inf. Model.* **2013**, *53* (5), 1223–1228.

(20) Pavia, D. L. *Introduction to spectroscopy: a guide for students of organic chemistry*, 3rd ed.; Harcourt College Publishers: Fort Worth, 2001.

(21) Smith, B. C. *Fundamentals of Fourier Transform Infrared Spectroscopy, Second Edition*; CRC Press, 2011.

(22) Jordan, R. B. *Reaction Mechanisms of Inorganic and Organometallic Systems*, 3 edition.; Oxford University Press: Oxford ; New York, 2007.

(23) Nelson, J. H. *Nuclear Magnetic Resonance Spectroscopy*, 1 edition.; Prentice Hall: Upper Saddle River, NJ, 2002.

(24) Perkampus, H.-H. *UV-VIS spectroscopy and its applications*; Springer laboratory; Springer-Verlag: Berlin ; New York, 1992.

(25) Alpert, N. L.; Keiser, W. E.; Szymanski, H. A. *IR; theory and practice of infrared spectroscopy*, 2nd ed.; Plenum Press: New York, 1970.

(26) Silverstein, R. M.; Webster, F. X.; Kiemle, D. *Spectrometric Identification of Organic Compounds*, 7 edition.; Wiley: Hoboken, NJ, 2005.

(27) In *Reactive Intermediates*; Santos, L. S., Ed.; Wiley-VCH Verlag GmbH & Co. KGaA, 2009; pp 307–317.

(28) Pernik, I.; Hooper, J. F.; Chaplin, A. B.; Weller, A. S.; Willis, M. C. *ACS Catal.* **2012**, *2* (12), 2779–2786.

(29) Chaplin, A. B.; Hooper, J. F.; Weller, A. S.; Willis, M. C. *J. Am. Chem. Soc.* **2012**, *134* (10), 4885–4897.

(30) Vikse, K. L.; Woods, M. P.; McIndoe, J. S. *Organometallics* **2010**, *29* (23), 6615–6618.

(31) Vikse, K. L.; Ahmadi, Z.; Luo, J.; van der Wal, N.; Daze, K.; Taylor, N.; McIndoe, J. S. *International Journal of Mass Spectrometry* **2012**, *323–324*, 8–13.

(32) Sutera, S. P.; Skalak, R. *Annual Review of Fluid Mechanics* **1993**, *25* (1), 1–20.

(33) Pike, S. D.; Pernik, I.; Theron, R.; McIndoe, J. S.; Weller, A. S. *Journal of Organometallic Chemistry* **2015**, *784*, 75–83.

(34) Dyson, P. J.; Johnson, B. F. G.; McIndoe, J. S.; Langridge-Smith, P. R. R. *Rapid Commun. Mass Spectrom.* **2000**, *14* (5), 311–313.

(35) Dyson, P. J.; Hearley, A. K.; Johnson, B. F. G.; McIndoe, J. S.; Langridge-Smith, P. R. R.; Whyte, C. *Rapid Commun. Mass Spectrom.* **2001**, *15* (12), 895–897.

(36) Butcher, C. P. G.; Johnson, B. F. G.; McIndoe, J. S.; Yang, X.; Wang, X.-B.; Wang, L.-S. *The Journal of Chemical Physics* **2002**, *116* (15), 6560–6566.

(37) Pape, J.; McQuinn, K.; Hof, F.; McIndoe, J. S. *New J. Chem.* **2011**, *35* (8), 1582–1587.

(38) Kobylianskii, I. J.; Widner, F. J.; Kräutler, B.; Chen, P. *J. Am. Chem. Soc.* **2013**, *135* (37), 13648–13651.

(39) McQuinn, K.; Hof, F.; McIndoe, J. S. *International Journal of Mass Spectrometry* **2009**, *279* (1), 32–36.

(40) Ryzhov, V.; Yang, C.-N.; Klippenstein, S. J.; Dunbar, R. C. *International Journal of Mass Spectrometry* **1999**, *185–187*, 913–923.

(41) Meyer, F.; Khan, F. A.; Armentrout, P. B. *J. Am. Chem. Soc.* **1995**, *117* (38), 9740–9748.

(42) Bauschlicher Jr., C. W.; Partridge, H. *Chemical Physics Letters* **1991**, *181* (2–3), 129–133.

(43) Pike, S. D.; Pernik, I.; Theron, R.; McIndoe, J. S.; Weller, A. S. *Journal of Organometallic Chemistry*.

(44) Johnson, H. C.; Torry-Harris, R.; Ortega, L.; Theron, R.; McIndoe, J. S.; Weller, A. S. *Catal. Sci. Technol.* **2014**, *4* (10), 3486–3494.

(45) Hartwig, J. F. *Organotransition Metal Chemistry: From Bonding to Catalysis*; University Science Books, 2010.

(46) Männig, D.; Nöth, H. *Angew. Chem. Int. Ed. Engl.* **1985**, *24* (10), 878–879.

(47) Davan, T.; Corcoran, E. W.; Sneddon, L. G. *Organometallics* **1983**, *2* (11), 1693–1694.

(48) Crudden, C. M.; Edwards, D. *Eur. J. Org. Chem.* **2003**, *2003* (24), 4695–4712.

(49) Burgess, K.; Van der Donk, W. A.; Westcott, S. A.; Marder, T. B.; Baker, R. T.; Calabrese, J. C. *J. Am. Chem. Soc.* **1992**, *114* (24), 9350–9359.
(50) Evans, D. A.; Fu, G. C.; Anderson, B. A. *J. Am. Chem. Soc.* **1992**, *114* (17), 6679–6685.
(51) Staubitz, A.; Robertson, A. P. M.; Sloan, M. E.; Manners, I. *Chem. Rev.* **2010**, *110* (7), 4023–4078.
(52) Scheideman, M.; Wang, G.; Vedejs, E. *J. Am. Chem. Soc.* **2008**, *130* (27), 8669–8676.
(53) Sewell, L. J.; Lloyd-Jones, G. C.; Weller, A. S. *J. Am. Chem. Soc.* **2012**, *134* (7), 3598–3610.
(54) Sewell, L. J.; Huertos, M. A.; Dickinson, M. E.; Weller, A. S.; Lloyd-Jones, G. C. *Inorg. Chem.* **2013**, *52* (8), 4509–4516.
(55) Leitao, E. M.; Jurca, T.; Manners, I. *Nat Chem* **2013**, *5* (10), 817–829.
(56) Luo, J.; Theron, R.; Sewell, L. J.; Hooper, T. N.; Weller, A. S.; Oliver, A. G.; McIndoe, J. S. *Organometallics* **2015**, In review.
(57) Hoops, S.; Sahle, S.; Gauges, R.; Lee, C.; Pahle, J.; Simus, N.; Singhal, M.; Xu, L.; Mendes, P.; Kummer, U. *Bioinformatics* **2006**, *22* (24), 3067–3074.
(58) James, B. R. *Homogeneous Hydrogenation*; Wiley, 1973.
(59) Young, J. F.; Osborn, J. A.; Jardine, F. H.; Wilkinson, G. *Chem. Commun. (London)* **1965**, No. 7, 131–132.
(60) Osborn, J. A.; Jardine, F. H.; Young, J. F.; Wilkinson, G. *J. Chem. Soc. A* **1966**, No. 0, 1711–1732.
(61) Halpern, J.; Okamoto, T.; Zakhariev, A. *Journal of Molecular Catalysis* **1977**, *2* (1), 65–68.
(62) Cabrera, M. I.; Zgolicz, P. D.; Grau, R. J. *Applied Catalysis A: General* **2008**, *334* (1–2), 291–303.
(63) Nelson, D. J.; Li, R.; Brammer, C. *J. Org. Chem.* **2005**, *70* (3), 761–767.
(64) Bowker, M.; Gland, J. L.; Joyner, R. W.; Li, Y.; Slin'ko, M. M.; Whyman, R. *Catal Lett* **1994**, *25* (3-4), 293–308.
(65) Koga, N.; Daniel, C.; Han, J.; Fu, X. Y.; Morokuma, K. *J. Am. Chem. Soc.* **1987**, *109* (11), 3455–3456.
(66) Wink, D.; Ford, P. C. *J. Am. Chem. Soc.* **1985**, *107* (6), 1794–1796.
(67) Wink, D. A.; Ford, P. C. *J. Am. Chem. Soc.* **1987**, *109* (2), 436–442.
(68) Duckett, S. B.; Newell, C. L.; Eisenberg, R. *J. Am. Chem. Soc.* **1993**, *115* (3), 1156–1157.
(69) Duckett, S. B.; Newell, C. L.; Eisenberg, R. *J. Am. Chem. Soc.* **1994**, *116* (23), 10548–10556.
(70) Chisholm, D. M.; Oliver, A. G.; McIndoe, J. S. *Dalton Trans.* **2010**, *39* (2), 364–373.
(71) Luo, J.; Oliver, A. G.; McIndoe, J. S. *Dalton Trans.* **2013**, *42* (31), 11312–11318.
(72) Schrock, R. R.; Osborn, J. A. *J. Am. Chem. Soc.* **1976**, *98* (8), 2134–2143.
(73) James, B. R.; Mahajan, D. *Can. J. Chem.* **1979**, *57* (2), 180–187.
(74) Knowles, W. S. *Adv. Synth. Catal.* **2003**, *345* (1-2), 3–13.
(75) James, B. R.; Wang, D. K. W. *Can. J. Chem.* **1980**, *58* (3), 245–250.
(76) Cipot, J.; McDonald, R.; Ferguson, M. J.; Schatte, G.; Stradiotto, M. *Organometallics* **2007**, *26* (3), 594–608.

(77) Bell, S.; Wüstenberg, B.; Kaiser, S.; Menges, F.; Netscher, T.; Pfaltz, A. *Science* **2006**, *311* (5761), 642–644.

(78) Kohrt, C.; Wienhöfer, G.; Pribbenow, C.; Beller, M.; Heller, D. *ChemCatChem* **2013**, *5* (10), 2818–2821.

(79) Sakai, K.; Ide, J.; Oda, O.; Nakamura, N. *Tetrahedron Letters* **1972**, *13* (13), 1287–1290.

(80) Milstein, D. *J. Chem. Soc., Chem. Commun.* **1982**, No. 23, 1357–1358.

(81) Vora, K. P.; Lochow, C. F. *Journal of Organometallic Chemistry* **1980**, *192* (2), 257–264.

(82) Suggs, J. W. *J. Am. Chem. Soc.* **1978**, *100* (2), 640–641.

(83) Jo, E.-A.; Jun, C.-H. *Tetrahedron Letters* **2009**, *50* (26), 3338–3340.

(84) Bosnich, B. *Acc. Chem. Res.* **1998**, *31* (10), 667–674.

(85) Eilbracht, P.; Gersmeier, A.; Lennartz, D.; Huber, T. *Synthesis* **1995**, *3*, 330–334.

(86) Vora, K. P.; Lochow, C. F.; Miller, R. G. *Journal of Organometallic Chemistry* **1980**, *192* (2), 257–264.

(87) Vora, K. P. *Synthetic Communications* **1983**, *13* (2), 99–102.

(88) Kokubo, K.; Matsumasa, K.; Miura, M.; Nomura, M. *J. Org. Chem.* **1997**, *62* (14), 4564–4565.

(89) Kokubo, K.; Matsumasa, K.; Nishinaka, Y.; Miura, M.; Nomura, M. *Bulletin of the Chemical Society of Japan* **1999**, *72* (2), 303–311.

(90) Tanaka, M.; Imai, M.; Yamamoto, Y.; Tanaka, K.; Shimowatari, M.; Nagumo, S.; Kawahara, N.; Suemune, H. *Org. Lett.* **2003**, *5* (8), 1365–1367.

(91) Imai, M.; Tanaka, M.; Tanaka, K.; Yamamoto, Y.; Imai-Ogata, N.; Shimowatari, M.; Nagumo, S.; Kawahara, N.; Suemune, H. *J. Org. Chem.* **2004**, *69* (4), 1144–1150.

(92) Willis, M. C.; McNally, S. J.; Beswick, P. J. *Angewandte Chemie International Edition* **2004**, *43* (3), 340–343.

(93) Willis, M. C.; Randell-Sly, H. E.; Woodward, R. L.; Currie, G. S. *Org. Lett.* **2005**, *7* (11), 2249–2251.

(94) Moxham, G. L.; Randell-Sly, H. E.; Brayshaw, S. K.; Woodward, R. L.; Weller, A. S.; Willis, M. C. *Angewandte Chemie International Edition* **2006**, *45* (45), 7618–7622.

(95) Moxham, G. L.; Randell-Sly, H.; Brayshaw, S. K.; Weller, A. S.; Willis, M. C. *Chem. Eur. J.* **2008**, *14* (27), 8383–8397.

(96) Tanaka, K.; Shibata, Y.; Suda, T.; Hagiwara, Y.; Hirano, M. *Org. Lett.* **2007**, *9* (7), 1215–1218.

(97) Osborne, J. D.; Randell-Sly, H. E.; Currie, G. S.; Cowley, A. R.; Willis, M. C. *J. Am. Chem. Soc.* **2008**, *130* (51), 17232–17233.

(98) Omura, S.; Fukuyama, T.; Horiguchi, J.; Murakami, Y.; Ryu, I. *J. Am. Chem. Soc.* **2008**, *130* (43), 14094–14095.

(99) Lenges, C. P.; White, P. S.; Brookhart, M. *J. Am. Chem. Soc.* **1998**, *120* (28), 6965–6979.

(100) Tsuda, T.; Kiyoi, T.; Saegusa, T. *J. Org. Chem.* **1990**, *55* (8), 2554–2558.

(101) Pape, J.; Vikse, K. L.; Janusson, E.; Taylor, N.; McIndoe, J. S. *International Journal of Mass Spectrometry* **2014**, *373*, 66–71.

(102) Jordan, R. F.; Dasher, W. E.; Echols, S. F. *J. Am. Chem. Soc.* **1986**, *108* (7), 1718–1719.

(103) Thomas, B. J.; Theopold, K. H. *J. Am. Chem. Soc.* **1988**, *110* (17), 5902–5903.

(104) Crabtree, R. H.; Hlatky, G. G.; Holt, E. M. *J. Am. Chem. Soc.* **1983**, *105* (25), 7302–7306.

(105) Brookhart, M.; Grant, B.; Volpe, A. F. *Organometallics* **1992**, *11* (11), 3920–3922.

(106) Hein, J. E.; Cao, B. H.; van der Meijden, M. W.; Leeman, M.; Kellogg, R. M. *Org. Process Res. Dev.* **2013**, *17* (6), 946–950.

(107) Fairlie, D. P.; Bosnich, B. *Organometallics* **1988**, *7* (4), 946–954.

(108) Roy, A. H.; Lenges, C. P.; Brookhart, M. *J. Am. Chem. Soc.* **2007**, *129* (7), 2082–2093.

(109) Walter, K. Stabilization of trichloroethylene and tetrachloroethylene. US2492048 A, December 20, 1949.

(110) Kadish, K. M.; Anderson, J. E. *Pure Appl. Chem.* **1987**, *59* (5), 703–714.

(111) Ito, J.; Kitase, M.; Nishiyama, H. *Organometallics* **2007**, *26* (25), 6412–6417.

(112) Yamaguchi, M.; Omata, K.; Hirama, M. *Tetrahedron Letters* **1994**, *35* (31), 5689–5692.

(113) Ren, P.; Pike, S. D.; Pernik, I.; Weller, A. S.; Willis, M. C. *Organometallics* **2015**, *34* (4), 711–723.

(114) Hooper, J. F.; Chaplin, A. B.; González-Rodríguez, C.; Thompson, A. L.; Weller, A. S.; Willis, M. C. *J. Am. Chem. Soc.* **2012**, *134* (6), 2906–2909.

(115) Arambasic, M.; Hooper, J. F.; Willis, M. C. *Org. Lett.* **2013**, *15* (20), 5162–5165.

(116) Guzel, B.; Omary, M. A.; Fackler Jr., J. P.; Akgerman, A. *Inorganica Chimica Acta* **2001**, *325* (1–2), 45–50.

(117) Roberts, C. F.; Hartley, R. C. *J. Org. Chem.* **2004**, *69* (18), 6145–6148.

Appendix

A NMR Sectra

^{13}C NMR Spectrum: $[NBu_3]^+ [PF_6]^-$ (5.23)

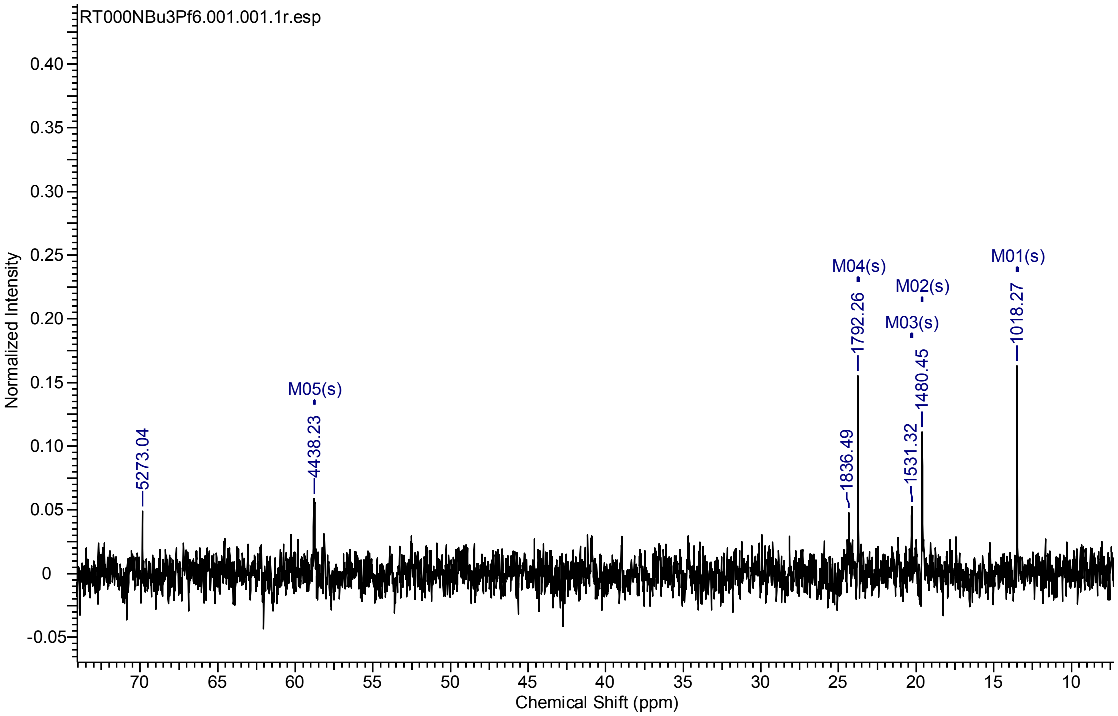

^{1}H NMR Spectrum: $[NBu_3]^+$ $[PF_6]^-$ (5.23)

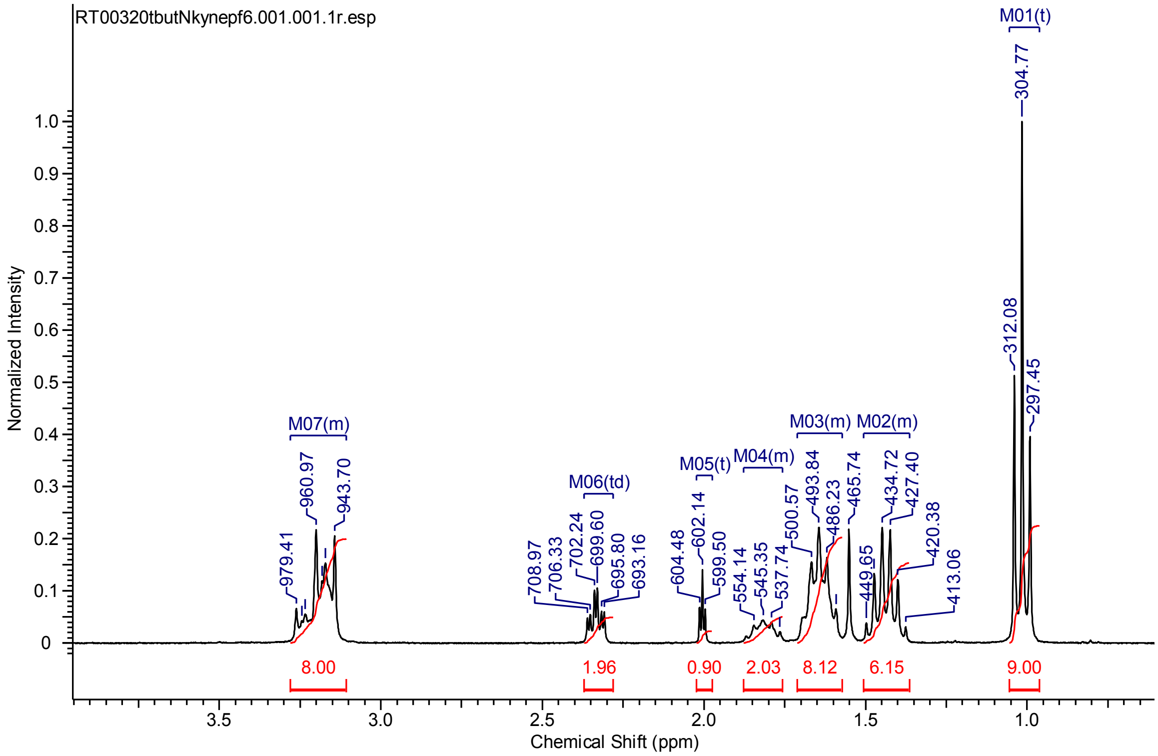

B Crystallography data

Crystal structure of hex-5-yn-1-yltributylammonium hexafluorophosphate **(5.23)**

(Crystallography by Dr. Allen Oliver, University of Notre Dame)

DISCUSSION

The compound crystallizes as colourless block-like crystals. There are four molecules of the ammonium cation and associated PF_6 anion in the unit cell of the primitive, acentric, orthorhombic space group $Pna2_1$. Though the compound is achiral, the space group is chiral. The correct enantiomorph of the space group was determined by comparison of intensities of Friedel pairs of reflections, yielding a Flack *x* parameter of 0.08(3) [3] and a Hooft *y* parameter of 0.07(3) [4]. A value of zero (0) indicate the correct enantiomorph, and a value one (1) the inverted absolute configuration.

The structure of the compound is as expected. The ammonium cation is tri-butyl hexyne amine. Bond distances and angles within the molecules are as expected.

CRYSTAL SUMMARY

Crystal data for $C_{18}H_{36}F_6NP$; M_r = 411.45; Orthorhombic; space group $Pna2_1$; a = 17.287(7) Å; b = 13.633(5) Å; c = 9.430(4) Å; $\alpha = 90°$; $\beta = 90°$; $\gamma = 90°$; V = 2222.4(15) Å^3; Z = 4; T = 120(2) K; λ(Mo-Kα) = 0.71073 Å; μ(Mo-Kα) = 0.174 mm^{-1}; d_{calc} = 1.230g.cm^{-3}; 36783 reflections collected; 4919 unique (R_{int} = 0.0406); giving R_1 = 0.0287, wR_2 = 0.0641 for 4493 data with [I>2σ(I)] and R_1 = 0.0340, wR_2 = 0.0672 for all 4919 data. Residual electron density (e^-.Å^{-3}) max/min: 0.154/-0.188.

An arbitrary sphere of data were collected on a colourless block-like crystal, having approximate dimensions of 0.323 × 0.157 × 0.119 mm, on a Bruker APEX-II diffractometer using a combination of ω- and φ-scans of 0.5° [1]. Data were corrected for absorption and polarization effects and analyzed for space group determination. The structure was solved by intrinsic phasing methods and expanded routinely [2]. The model was refined by full-matrix least-squares analysis of F^2 against all reflections. All non-hydrogen atoms were refined with anisotropic thermal displacement parameters. Unless otherwise noted, hydrogen atoms were included in calculated positions. Thermal parameters for the hydrogens were tied to the isotropic thermal parameter of the atom to which they are bonded (1.5 × for methyl, 1.2 × for all others).

REFERENCES

[1] Bruker AXS. (2008). *APEX-2*. Bruker-Nonius AXS, Madison, Wisconsin, USA.

[2] G. M. Sheldrick, *Acta Cryst.*, **2008**, *A64*, 112.

[3] S. Parsons & H.D. Flack, *Acta Cryst.* **2004**, *A60*, s61.

[4] R. W. W. Hooft, L. H. Straver & A. L. Spek, *J. Appl. Cryst.*, **2008**, *41*, 96.

Table 1. Crystal data and structure refinement for uvic1401.

Identification code	uvic1401
Empirical formula	$C_{18}H_{36}F_6NP$
Formula weight	411.45
Temperature	120(2) K
Wavelength	0.71073 Å
Crystal system	Orthorhombic
Space group	$Pna2_1$
Unit cell dimensions	a = 17.287(7) Å α = 90°
	b = 13.633(5) Å β = 90°
	c = 9.430(4) Åγ = 90°
Volume	2222.4(15) $Å^3$
Z	4
Density (calculated)	1.230 $g.cm^{-3}$
Absorption coefficient (μ)	0.174 mm^{-1}
F(000)	880
Crystal color, habit	colourless, block
Crystal size	0.323 × 0.157 × 0.119 mm^3
θ range for data collection	1.902 to 27.183°
Index ranges	$-22 \leq h \leq 22$, $-17 \leq k \leq 17$, $-12 \leq l \leq 12$
Reflections collected	36783
Independent reflections	4919 [R_{int} = 0.0406]
Completeness to θ = 25.242°	100.0 %
Absorption correction	Numerical
Max. and min. transmission	0.9814 and 0.9432
Refinement method	Full-matrix least-squares on F^2
Data / restraints / parameters	4919 / 1 / 238
Goodness-of-fit on F^2	1.029
Final R indices [$I>2\sigma(I)$]	R_1 = 0.0287, wR_2 = 0.0641
R indices (all data)	R_1 = 0.0340, wR_2 = 0.0672
Absolute structure parameter	0.08(3)
Extinction coefficient	n/a
Largest diff. peak and hole	0.154 and -0.188 $e^{-}.Å^{-3}$

Table 2. Atomic coordinates and equivalent isotropic displacement parameters (Å^2) for uvic1401. U(eq) is defined as one third of the trace of the orthogonalized U_{ij} tensor.

	x	y	z	U(eq)
N(1)	0.70085(10)	0.46328(12)	0.52922(17)	0.020(1)
C(1)	0.74467(13)	0.41312(15)	0.6485(2)	0.025(1)
C(2)	0.77487(15)	0.48122(16)	0.7643(2)	0.033(1)
C(3)	0.81910(13)	0.42307(17)	0.8779(2)	0.031(1)
C(4)	0.76692(13)	0.35504(16)	0.9636(2)	0.028(1)
C(5)	0.80724(13)	0.30964(16)	1.0843(2)	0.028(1)
C(6)	0.83986(15)	0.27507(17)	1.1822(2)	0.034(1)
C(7)	0.74894(12)	0.54521(14)	0.4618(2)	0.023(1)
C(8)	0.82918(13)	0.51593(16)	0.4100(3)	0.030(1)
C(9)	0.86510(14)	0.60173(18)	0.3290(3)	0.043(1)
C(10)	0.94710(15)	0.5804(2)	0.2782(4)	0.057(1)
C(11)	0.68286(12)	0.38740(14)	0.4148(2)	0.022(1)
C(12)	0.62586(12)	0.30719(15)	0.4543(2)	0.025(1)
C(13)	0.61582(14)	0.23998(16)	0.3264(3)	0.032(1)
C(14)	0.55711(16)	0.15850(19)	0.3517(3)	0.049(1)
C(15)	0.62679(11)	0.50801(14)	0.5889(2)	0.022(1)
C(16)	0.57275(12)	0.55372(16)	0.4809(2)	0.026(1)
C(17)	0.50531(11)	0.60347(15)	0.5556(2)	0.024(1)
C(18)	0.45012(15)	0.6503(2)	0.4515(3)	0.045(1)
P(1)	0.36381(3)	0.34586(4)	0.57200(6)	0.023(1)
F(1)	0.28002(8)	0.33318(11)	0.50248(16)	0.044(1)
F(2)	0.34100(8)	0.45424(9)	0.62415(14)	0.035(1)
F(3)	0.38597(9)	0.23719(10)	0.52019(15)	0.039(1)
F(4)	0.44750(8)	0.35838(10)	0.64048(14)	0.037(1)
F(5)	0.33162(8)	0.30153(10)	0.71840(13)	0.033(1)
F(6)	0.39554(8)	0.38991(10)	0.42492(13)	0.038(1)
H(1A)	0.7891	0.3773	0.6071	0.029
H(1B)	0.7101	0.3639	0.6928	0.029
H(2A)	0.7309	0.5161	0.8088	0.039
H(2B)	0.8096	0.5308	0.7217	0.039
H(3A)	0.8599	0.3836	0.8314	0.037
H(3B)	0.8448	0.4697	0.9432	0.037
H(4A)	0.7221	0.3929	0.9993	0.034
H(4B)	0.7469	0.3028	0.9006	0.034
H(6)	0.8661	0.2473	1.2611	0.052
H(7A)	0.7196	0.5721	0.3804	0.027
H(7B)	0.7548	0.5986	0.5321	0.027
H(8A)	0.8253	0.4580	0.3472	0.036
H(8B)	0.8623	0.4984	0.4918	0.036
H(9A)	0.8322	0.6172	0.2459	0.052
H(9B)	0.8660	0.6602	0.3912	0.052

H(10A)	0.9671	0.6375	0.2267	0.086
H(10B)	0.9466	0.5233	0.2151	0.086
H(10C)	0.9803	0.5668	0.3601	0.086
H(11A)	0.6624	0.4224	0.3308	0.026
H(11B)	0.7320	0.3559	0.3862	0.026
H(12A)	0.5755	0.3364	0.4810	0.030
H(12B)	0.6456	0.2693	0.5362	0.030
H(13A)	0.5990	0.2797	0.2441	0.038
H(13B)	0.6664	0.2102	0.3026	0.038
H(14A)	0.5518	0.1190	0.2655	0.073
H(14B)	0.5069	0.1874	0.3762	0.073
H(14C)	0.5748	0.1167	0.4298	0.073
H(15A)	0.5982	0.4562	0.6404	0.026
H(15B)	0.6412	0.5589	0.6589	0.026
H(16A)	0.5530	0.5023	0.4162	0.031
H(16B)	0.6013	0.6025	0.4235	0.031
H(17A)	0.4771	0.5544	0.6130	0.029
H(17B)	0.5255	0.6543	0.6208	0.029
H(18A)	0.4092	0.6847	0.5034	0.068
H(18B)	0.4270	0.5995	0.3915	0.068
H(18C)	0.4783	0.6972	0.3920	0.068

Table 3. Anisotropic displacement parameters (Å^2) for uvic1401.
The anisotropic displacement factor exponent takes the form:
$-2\pi^2[h^2a^{*2}U_{11} + ... + 2hka^*b^*U_{12}]$

	U_{11}	U_{22}	U_{33}	U_{23}	U_{13}	U_{12}
N(1)	0.0251(9)	0.0164(8)	0.0197(8)	-0.0002(6)	-0.0018(7)	0.0030(7)
C(1)	0.0306(11)	0.0194(10)	0.0238(10)	0.0028(8)	-0.0070(9)	0.0039(9)
C(2)	0.0449(14)	0.0227(11)	0.0301(11)	0.0014(9)	-0.0129(11)	-0.0012(10)
C(3)	0.0321(12)	0.0310(11)	0.0286(11)	0.0028(9)	-0.0102(10)	-0.0030(10)
C(4)	0.0273(11)	0.0319(11)	0.0252(10)	-0.0007(9)	-0.0017(9)	0.0038(9)
C(5)	0.0356(12)	0.0267(10)	0.0227(10)	-0.0029(10)	0.0020(10)	0.0039(9)
C(6)	0.0467(14)	0.0330(13)	0.0234(11)	0.0000(10)	0.0005(10)	0.0113(11)
C(7)	0.0251(10)	0.0160(9)	0.0271(10)	0.0017(8)	0.0002(9)	0.0009(8)
C(8)	0.0256(11)	0.0216(10)	0.0440(13)	0.0030(10)	0.0026(10)	0.0035(9)
C(9)	0.0292(13)	0.0297(13)	0.0712(19)	0.0087(13)	0.0105(13)	0.0011(10)
C(10)	0.0339(15)	0.0450(16)	0.092(2)	0.0126(17)	0.0201(15)	0.0024(12)
C(11)	0.0257(11)	0.0188(9)	0.0202(9)	-0.0033(8)	-0.0004(8)	0.0037(8)
C(12)	0.0253(11)	0.0208(10)	0.0284(11)	-0.0010(8)	0.0001(9)	0.0003(8)
C(13)	0.0305(12)	0.0288(11)	0.0369(13)	-0.0065(10)	-0.0077(10)	0.0001(9)
C(14)	0.0365(14)	0.0357(14)	0.074(2)	-0.0193(14)	-0.0037(14)	-0.0054(11)
C(15)	0.0263(10)	0.0208(9)	0.0185(10)	-0.0003(8)	0.0032(8)	0.0045(8)
C(16)	0.0246(11)	0.0300(11)	0.0230(10)	0.0031(9)	0.0024(8)	0.0064(9)
C(17)	0.0214(10)	0.0263(10)	0.0253(10)	-0.0023(9)	0.0019(9)	0.0003(8)
C(18)	0.0339(14)	0.0640(18)	0.0377(14)	0.0070(13)	0.0060(12)	0.0240(12)
P(1)	0.0272(3)	0.0232(2)	0.0182(2)	-0.0020(2)	0.0001(2)	-0.0056(2)
F(1)	0.0337(8)	0.0514(9)	0.0460(8)	-0.0019(7)	-0.0128(7)	-0.0122(7)
F(2)	0.0438(8)	0.0233(7)	0.0389(7)	-0.0025(6)	0.0041(6)	-0.0012(6)
F(3)	0.0545(9)	0.0287(7)	0.0330(7)	-0.0083(6)	0.0103(7)	-0.0025(6)
F(4)	0.0301(7)	0.0473(9)	0.0337(7)	-0.0010(6)	-0.0059(6)	-0.0047(6)
F(5)	0.0467(8)	0.0293(7)	0.0240(6)	-0.0007(5)	0.0101(6)	-0.0080(6)
F(6)	0.0542(9)	0.0407(8)	0.0202(6)	0.0033(6)	0.0043(6)	-0.0143(7)

Table 4. Bond lengths [Å] for uvic1401.

atom-atom	distance	atom-atom	distance	
N(1)-C(1)	1.519(3)	N(1)-C(15)	1.526(3)	N(1)-C
1.524(3)	C(8)-C(9)	1.529(3)	C(9)-C(10)	1.524(
1.5993(15)	P(1)-F(3)	1.6063(15)	P(1)-F(2)	1.6064
H(3B)	0.9900	C(4)-H(4A)	0.9900	C(4)-H
0.9900	C(10)-H(10A)	0.9800	C(10)-H(10B)	0.9800
0.9900	C(14)-H(14A)	0.9800	C(14)-H(14B)	0.9800
0.9900	C(18)-H(18A)	0.9800	C(18)-H(18B)	0.9800

Symmetry transformations used to generate equivalent atoms:

Table 5. Bond angles [°] for uvic1401.

atom-atom-atom	angle	atom-atom-atom	angle	
C(1)-N(1)-C(15)	108.97(16)	C(1)-N(1)-C(11)	108.66(15)	C(15)-
C(3)-C(2)	112.87(19)	C(5)-C(4)-C(3)	112.66(18)	C(6)-C
C(12)	113.0(2)	C(16)-C(15)-N(1)	115.67(16)	C(15)-
P(1)-F(2)	90.14(8)	F(3)-P(1)-F(2)	179.55(8)	F(4)-P
F(6)	90.04(8)	F(2)-P(1)-F(6)	90.25(8)	F(5)-P
109.5	C(1)-C(2)-H(2B)	109.5	C(3)-C(2)-H(2B)	
	109.5	H(2A)-C(2)-H(2B)	108.1	C(4)-C
109.1	C(3)-C(4)-H(4B)	109.1	H(4A)-C(4)-H(4B)	
	107.8	C(5)-C(6)-H(6)	180.0	C(8)-C
109.8	C(9)-C(8)-H(8B)	109.8	H(8A)-C(8)-H(8B)	
	108.3	C(10)-C(9)-H(9A)	109.0	C(8)-C
H(10C)	109.5	H(10A)-C(10)-H(10C)	109.5	H(10B
H(12A)	110.1	C(11)-C(12)-H(12B)	110.1	C(13)-
C(14)-H(14A)	109.5	C(13)-C(14)-H(14B)	109.5	H(14A
C(15)-H(15B)	108.4	H(15A)-C(15)-H(15B)	107.4	C(15)-
H(17B)	109.3	C(16)-C(17)-H(17B)	109.3	H(17A

Symmetry transformations used to generate equivalent atoms:

Table 6. Torsion angles [°] for uvic1401.

atom-atom-atom-atom	angle	atom-atom-atom-atom	angle
C(15)-N(1)-C(1)-C(2)	-65.2(2)	C(11)-N(1)-C(1)-C(2)	173.57(18)
		C(7)-N(1)-C(1)-C(2)	54.5(2)
		N(1)-C(1)-C(2)-C(3)	-179.18(18)
		C(1)-C(2)-C(3)-C(4)	-67.3(3)
		C(2)-C(3)-C(4)-C(5)	-172.27(19)
		C(1)-N(1)-C(7)-C(8)	53.9(2)
		C(15)-N(1)-C(7)-C(8)	173.84(18)
		C(11)-N(1)-C(7)-C(8)	-65.5(2)
		N(1)-C(7)-C(8)-C(9)	172.7(2)
		C(7)-C(8)-C(9)-C(10)	177.6(2)
		C(1)-N(1)-C(11)-C(12)	67.4(2)
		C(15)-N(1)-C(11)-C(12)	-52.5(2)
		C(7)-N(1)-C(11)-C(12)	-171.47(17)
		N(1)-C(11)-C(12)-C(13)	179.80(17)
		C(11)-C(12)-C(13)-C(14)	-177.72(19)
		C(1)-N(1)-C(15)-C(16)	-175.05(17)
		C(11)-N(1)-C(15)-C(16)	-55.3(2)
		C(7)-N(1)-C(15)-C(16)	63.5(2)
		N(1)-C(15)-C(16)-C(17)	-174.82(16)
		C(15)-C(16)-C(17)-C(18)	179.81(19)

Symmetry transformations used to generate equivalent atoms: